I N A U G U R A L - D I S S E R T A T I O N
zur
Erlangung der Doktorwürde
der
Naturwissenschaftlich-Mathematischen
Gesamtfakultät
der
Ruprecht–Karls–Universität
Heidelberg

vorgelegt von
Dipl.–Phys. **Alex Peter Großmann**
aus Rastatt

Tag der mündlichen Prüfung: 01.Juli 1998

Thema

Magnetic Field Determination in a Superferric Storage Ring for a Precise Measurement of the Muon Magnetic Anomaly

Gutachter : **Priv. Doz. Dr. Klaus Jungmann**
Prof. Dr. Karlheinz Meier

Zusammenfassung

Am Brookhaven National Laboratory in Upton, New York, wurde 1997 ein neues Experiment zur Messung der magnetischen Anomalie des Myons in einer internationalen Kollaboration in Betrieb genommen mit dem Ziel, diese auf $0.35\,ppm$ zu vermessen. Damit kann der Anteil der schwachen Wechselwirkung mit 25% Genauigkeit bestimmt und eine Suche nach neuer Physik jenseits des Standardmodells durchgeführt werden. Zur Messung werden polarisierte Myonen in einen Speicherring mit $14\,m$ Durchmesser injiziert und die Differenz zwischen Spinpräzessions-und Zyklotronfrequenz bestimmt, welche direkt proportional zur magnetischen Anomalie des Myons und zur durchschnittlichen Stärke des Magnetfeldes ist. Die asymmetrische räumliche Verteilung der Zerfallspositronen bezüglich der Myonspinrichtung aufgrund der nicht erhaltenen Parität bei der schwachen Wechselwirkung bildet die Grundlage der Detektion der Spinpräzession.
Im Rahmen dieser Doktorarbeit wurde ein Magnetfeldmeßsystem auf Basis gepulster Kernspinresonanz (NMR) aufgebaut und die Magnetfelddaten der ersten Messung ausgewertet. Das Meßsystem selbst ist mit einer Genauigkeit von besser als $0.1\,ppm$ eine Größenordnung präziser als die besten kommerziell erhältlichen Meßgeräte. Dabei wird ein NMR-Trolley eingesetzt, welches das Magnetfeld direkt im Speichervolumen im Vakuum vermessen kann. Zusammen mit 366 fest montierten Meßsonden erlaubt es die kontinuierliche Überwachung des Magnetfeldes. Während der ersten Testmeßphase konnte das durchschnittliche Feld auf $1\,ppm$, begrenzt vor allem durch Feldinhomogenitäten, bestimmt werden. Für die Anomalie ergab sich $a_\mu = 1.165925 \cdot 10^{-3} \pm 13\,ppm$ in Übereinstimmung mit der Theorie und früheren CERN Experimenten.

Abstract

At the Brookhaven National Laboratory in Upton, New York, a new experiment to measure the anomalous magnetic moment of the muon in international collaboration was commissioned in 1997, the ultimate goal of which is an accuracy of $0.35\,ppm$. This allows to determine the contribution of the weak interaction with 25% accuracy and to search for new physics beyond the standard model. To measure the muon magnetic anomaly polarized muons are injected into a storage ring and the difference between the spin precession frequency and the cyclotron frequency is determined, which is directly proportional to the magnetic anomaly of the muon and to the average strength of the magnetic field. The spatial asymmetry of the decay positrons with respect to the muon spin due to the non-conservation of parity in the weak interaction allows the detection of the spin-precession.
In the framework of this doctoral thesis a magnetic field measurement system based on pulsed nuclear magnetic resonance (NMR) was built and the magnetic field data for the first run was evaluated. The system itself has an accuracy of $0.1\,ppm$, one order of magnitude better than the best commercially available devices. A NMR-Trolley is used which can directly measure the magnetic field in vacuum inside the storage volume. Together with 366 fixed probes this allows continuous monitoring of the magnetic field. During the first engineering run the average field was determined with an accuracy of $1\,ppm$ limited mainly by field inhomogeneities. The result for the measurement of the anomaly is $a_\mu = 1.165925 \cdot 10^{-3} \pm 13\,ppm$ in agreement with theory and former experiments at CERN.

Contents

List of Figures

List of Tables

1 Precision Experiments for Testing Standard Theory

Precision experiments can put stringent tests on the theoretical description of processes in physics and explore the limits of today's theoretical models used in physics. The standard model of the unified electroweak interaction has been confirmed with impressive precision, for example in experiments using the LEP storage ring at CERN [1]. On the other hand it is also possible to conduct tests of the standard model in a lower energy range. Precision measurements of atomic parity violation, for example, demonstrate the validity of the unified electroweak theory over 10 orders of magnitude in momentum transfer. Other examples at lower energies are the search for particle decays not included in standard theory, such as $\mu \rightarrow e\gamma$, $\mu Z \rightarrow Ze$, $\mu^+e^- \rightarrow \mu^-e^+$, $\tau \rightarrow e\gamma$ and many others, none of which have been unambiguously observed up to date. Some extensions of the standard model however predict such processes.
Precision measurements with single particles and simple (one and two electron) atomic systems have a long history for determining accurate values of fundamental constants and of revealing new physics at that time. Examples are the discovery of nuclear isotopes by finding deuterium through a splitting of the Balmer-α-line of natural hydrogen one of which was the new isotope deuterium . A deviation of the hyperfine structure in atomic Hydrogen from Fermi theory observed by Nafe, Nelson and Rabi [2] in 1947 could be explained by Breit [4] assuming that the magnetic g-factor of the electron differs from the integer value 2 as predicted by Dirac theory [5]. The observation could be confirmed in an atomic spin precession experiment by Kusch and Foley [6] in the same year.
The discovery of the electron's magnetic anomaly a_e together with the observation of the $2^2S_{1/2} - 2^2P_{1/2}$ Lamb-shift by Lamb and Retherford [7] in 1947 has initiated the development of the modern field theory of quantum electrodynamics (QED) [8]. Today the electron's and positron's magnetic anomaly ranks among the best known universal constants in physics since it has been measured very precisely on single electrons in a Penning trap by Dehmelt and coworkers [9, 10]. Its present good agreement with values calculated in the framework of QED demonstrates to which accuracy electromagnetic processes can be predicted. In reverse the theory can be used to extract from the measurement the most accurate value of the important fundamental constant α at zero momentum transfer, in very good agreement with values of α determined in atomic, solid state and neutron physics (see chapter 2.1).
When the muon was observed for the first time by P. Kunze in 1933 [11] it was a totally unexpected particle. When it was seen in other experiments by Anderson and Neddermeyer [12] and by Street and Stevenson [13], both in 1937, its identity was first mistaken as the particle predicted by Yukawa [14] to mediate the strong interaction, now known as the pion. After Powells [15, 16] observation of the real pion in 1947 its identity as a lepton became apparent and it is now well established that the muon acts like a heavy electron. It was the first representative of the second

generation of fundamental fermions, which later was completed by the observation of the muon neutrino as a distinctive particle, different from the electron neutrino, and the strange and charm quarks later. This phenomenon, the electron-muon universality was observed very critically ever since, and with the discovery of the third particle generation was expanded to the $e-\mu-\tau$ universality. From scattering at highest possible energies it can be concluded that leptons l (e, μ, τ) are 'point-like' particles down to dimensions of $10^{-18}\,m$.

2 Theory of the Magnetic Anomaly of the Muon

The magnetic moment μ of a particle is proportional to its intrinsic angular momentum (spin) $\hbar\vec{s}$, its charge and inversely proportional to its mass

$$\vec{\mu} = g\mu_B\vec{s} \quad , \quad \mu_B = \frac{e\hbar}{2mc}, \tag{1}$$

where μ_B is the Bohr magneton of a particle with electric charge e. $\hbar$ is the Planck constant and c is the speed of light in vacuum. In the framework of relativistic quantum mechanics, particularly in Dirac theory [5], the proportionality constant g equals 2 for point-like fermions.
For non-point-like particles, e.g. the proton, the g factor differs significantly from 2. Even the neutron has a magnetic moment although it does not have an electric charge. The large magnetic anomaly of these objects which are composed of quarks and gluons is due to their inner structure and the dynamics of their constituents.
For point-like leptons l, where l represents e, μ and τ, there is also a small deviation due to interaction between the particle and virtual fields, the magnetic anomaly defined as

$$a_l := \frac{g_l - 2}{2}. \tag{2}$$

The biggest contributions to the magnetic anomaly come from corrections due to quantum electro-dynamical (QED) effects. The first measurements of a_μ confirmed that the muon interacts with fields and other particles [17] like the electron. The only difference seemed to be the bigger mass ($m_\mu \approx 207 m_e$). Since leptons of lower mass exist the muon further decays due to weak interaction. The relatively long lifetime of $2.2\mu s$ renders the possibility to perform precision measurements. Therefore the properties of the muon are known to very high precision. The g factor of the muon already is the best known parameter of any decaying particle [18]. The magnetic anomalies of the muon and the electron are different because of the higher mass of the muon. The higher mass enhances the effects of processes with high momentum transfers by a factor of $(m_\mu/m_e)^2 \approx 4\times10^4$. Therefore $g_\mu - 2$ is a much better probe for corrections due to the influence of heavy particles on the vacuum polarization compared to $g_e - 2$ even though it is possible to measure $g_e - 2$ more precise [9, 10]. The experimental values for electron

$$a_{e^-} = 1159652188.4(4.3) \times 10^{-12}\ (3.7ppb) \tag{3}$$

and positron

$$a_{e^+} = 1159652187.9(4.3) \times 10^{-12}\ (3.7ppb) \tag{4}$$

agree well with theory [22]

$$a_e = 1159652156.4(1.2)(27.5) \times 10^{-12}\ (24ppb), \tag{5}$$

where the first error comes from calculation and the second error comes from uncertainty in the fine structure constant α [19]. The contribution of heavier particles, including muons in vacuum polarization loops is 4.46×10^{-12} [20]. For the electron even at that level of accuracy only quantum electro-dynamical contributions are of importance whereas for the muon other contributions have to be taken into account. The contributions to the anomaly a_μ consist of :

- The by far dominating electromagnetic interaction contribution. This effect is known to better than 0.02 *ppm* and contributes to 99.994% of the total anomaly.

- Corrections due to the strong interaction. The size of the hadronic corrections is about 60 *ppm* and is known to better than 1 *ppm* at present employing measured data for $e^+\ e^-$ scattering into hadrons. Additional data from on-going $e^+e^- \to hadron$ experiments together with the analysis of hadronic τ decays from ALEPH and CLEO data are expected to decrease this uncertainty.

- Corrections due to the weak interaction. The weak interaction contributes 1.30 ± 0.03 *ppm*.

- Possible effects arising from new physics not contained in the standard model could in some cases contribute as much as the present experimental uncertainty of 7.2 *ppm*.

2.1 The QED Contribution to the Magnetic Anomaly of the Muon

The QED contribution can be written in the general form

$$a_\mu(QED) = A_1 + A_2\left(\frac{m_\mu}{m_e}\right) + A_2\left(\frac{m_\mu}{m_\tau}\right) + A_3\left(\frac{m_\mu}{m_e}, \frac{m_\mu}{m_\tau}\right) \tag{6}$$

where m_e, m_μ and m_τ are the masses of the electron e, muon μ and tauon τ respectively. Renormalizability of QED guarantees that the functions A1, A2 and A3 can be expanded in power series of α divided by π with finite calculable coefficients:

$$A_i = A_i^{(2)}\left(\frac{\alpha}{\pi}\right) + A_i^{(4)}\left(\frac{\alpha}{\pi}\right)^2 + A_i^{(6)}\left(\frac{\alpha}{\pi}\right)^3 + A_i^{(8)}\left(\frac{\alpha}{\pi}\right)^3 + ..., \quad i = 1, 2, 3. \tag{7}$$

The first terms A_1 are exactly the same for both the muon and the electron. $A_1^{(2)}$ for example describes the effect of the emission of a virtual photon and its value is 1/2. This term was determined by Schwinger [8] 1948 in the early days of QED and contributes more than 99.5 % to the total value

$$a_l \approx A_1^{(2)}\left(\frac{\alpha}{\pi}\right) = \left(\frac{\alpha}{2\pi}\right). \tag{8}$$

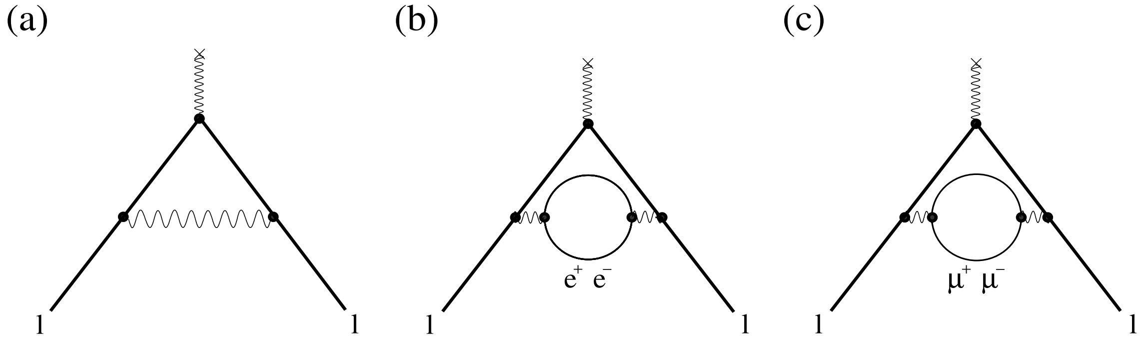

Figure 2.1: *(a) The lowest order contribution which accounts for more than* 99.5% *of* a_μ *or* a_e*. (b) One of the* 4*th order contributions to* a_μ *(vacuum polarization with* e^+e^- *pairs). (c) The contribution of this graph involving vacuum polarization with* $\mu^+\mu^-$ *pairs is very small for electrons due to their lower mass (*$\Delta a_e \approx 4 \times 10^{-12}$*)*

It is the same for all charged leptons l. Starting with the 4th order ($\left(\frac{\alpha}{\pi}\right)^2$) there are differences for muon and electron arising from the terms A_2 and A_3.
The expansion converges faster for electrons. In order to determine $a_\mu(QED)$ to better than 10^{-7}, it is necessary to calculate all contributions up to 8th order. The total QED effect then is [21, 22]

$$a_\mu(QED) = +11658470.57(0.18)(0.05) \times 10^{-10}\,(\pm 0.016)\,ppm \,\text{(Kinoshita 1996,1998)} \tag{9}$$

The first uncertainty arises from the accuracy of numerical calculations, the second from the knowledge of the fine structure constant α. The uncertainty in the QED contribution as it is available today is negligible compared with the proposed experimental accuracy.
The accuracy of the calculations for the electron is limited by the uncertainty in the fine structure constant α. The measurement of a_e together with the calculation however can be used to obtain the most precise value α [22, 9]:

$$\alpha^{-1} = 137.03599993(14)(50)\,(1\,ppb)(3.7\,ppb), \tag{10}$$

where the first error comes from the calculation and the second one from the experimental uncertainty. This is more than one order of magnitude better than the values obtained from measurements based on the quantum Hall effect [19], the AC Josephson effect [23], the de Broglie wave length of a neutron beam [24] and the muonium hyperfine structure [25].

2.2 QCD Corrections

Vacuum polarization loops containing hadrons yield another contribution to a_μ at a measurable level ($\approx 60ppm$) [26]. At present it is impossible to calculate these contributions either analytically or numerically with any accuracy comparable with the one necessary for the $g_\mu - 2$ experiment due to the current lack of understanding of Quantum Chromo Dynamics (QCD). Instead one has to use the measured ratio of cross-sections [27, 28]

$$R_\sigma(s) := \frac{\sigma(s)(e^+e^- \to \gamma^* \to hadrons)}{\sigma(s)(e^+e^- \to \gamma^* \to \mu^+\mu^-)} \tag{11}$$

and a dispersion relation. The hadronic part of the magnetic anomaly yields then

$$\Delta a_\mu(\text{had. vac. pol.}) \mid \mathcal{O}(\alpha^2) = \left(\frac{\alpha m_\mu}{3\pi}\right)^2 \int_{4m_\pi^2}^{\infty} ds \frac{R(s)K(s)}{s^2}, \tag{12}$$

where

$$K(s) = \frac{3s}{m_\mu^2}\left[x^2\left(1-\frac{x^2}{2}\right) + (1+x)^2\left(1+\frac{1}{x^2}\right)\left[ln(1+x) - x + \frac{x^2}{2}\right] + \frac{1+x}{1-x}x^2 lnx\right] \tag{13}$$

and

$$x = \frac{1-\beta}{1+\beta}, \qquad \beta = \sqrt{1-\frac{4m_\mu^2}{s}}. \tag{14}$$

The integral is dominated by the kinematic region from 0.1 GeV to several GeV (see table 2.2). There have been several evaluations of the hadronic contribution to a_μ which are in good agreement. At the moment several experiments try to measure the cross-sections of $\sigma(e^+e^- \to \gamma^* \to hadrons)$ in this kinematic region to a higher accuracy.

The CMD and OLYA experiments at the Budker Institute of Nuclear Physics (BINP, Novosibirsk, Russia) obtained data for charged and neutral particles in the final state in the region from $0.36\,GeV < \sqrt{s} < 1.4\,GeV$. A new detector CMD2 and the upgrade of the VEPP-2M accelerator will further decrease the systematical and statistical error in this region. At Frascati (Italy) a new ϕ factory is under construction which would make it possible to improve the data in the region $\sqrt{s} < 1.0\,GeV$. In addition it is planned to measure $R(s)$ at the Bejing accelerator BEPC at energies between $2.0\,GeV$ and $3.1\,GeV$. The different energy regions and final states affect the result to a different order of magnitude (see figure 2.2).

A second way to determine the hadronic contribution is through hadronic τ decays [29, 30, 31]. The relevant diagram is shown in figure 2.4. The weak W current can be related to the electromagnetic current also shown in figure 2.4. The ALEPH [32, 33, 34] and the CLEO [35, 36] collaboration have collected data on hadronic τ decays. Aleph collected the data from 1991-1994 at $\sqrt{s} = m_{Z^0}$ and CLEO measures at the $\Upsilon 4s$ resonance. Adding these data and the world data sample of $e^+e^- \to hadrons$, R. Alemany, M. Davier and A. Höcker [30] obtain

$$\Delta a_\mu(\text{had.}\mathcal{O}(\alpha^2)) = +701.1(9.4) \times 10^{-10}\ (60.13 \pm 0.81)ppm\ \text{(Alemany, 1998)}. \tag{15}$$

Very recently M. Davier and A. Höcker [31] improved their earlier result using e^+e^- data,τ decay data and a theoretical model of $R(s)$ which yields

$$\Delta a_\mu(\text{had.}\mathcal{O}(\alpha^2)) = +695.1(7.5) \times 10^{-10}\ (59.61 \pm 0.64)ppm\ \text{(Davier,1998)}. \tag{16}$$

After the analysis of all CLEO data will be finished, the uncertainty of Δa_μ(had.) will be further reduced.

For higher order corrections there are 2 calculations by Kinoshita [21] and Krause

$\Delta a_\mu^{had.\mathcal{O}(\alpha^2)} \times 10^{10}$	error in ppm	author	year,ref
663 (85)	7.3ppm	Barger et al.	1975 [37]
699 (88)	7.6ppm	Calmet et al.	1976 [38]
702 (80)	6.9ppm	Narison et al.	1978 [39]
684 (11)	0.9ppm	Barkov et al.	1985 [40]
707 (6)(16)	1.5ppm	Kinoshita et al.	1985 [21, 41]
707 (10)(5)	1.0ppm	Casas et al.	1985 [42]
705 (6)(5)	0.9ppm	Martinovic, Dubnicka	1990 [43]
724 (7)(26)	2.3ppm	Jegerlehner	1991 [44]
699 (4)(2)	0.4ppm	Dubnickova et al.	1992 [45]
702 (6)(14)	1.3ppm	Eidelman, Jegerlehner	1995,1996 [46, 47]
711 (10)	0.9ppm	Adel, Yndurain	1995 [48]
703 (8)(13)	1.3ppm	Worstell, Brown	1995 [49]
695 (15)	1.3ppm	R. Alemany et al.	1996 [29]
701.1 (9.4)	0.81ppm	R. Alemany et al.	1998 [30]
695.1 (7.5)	0.64ppm	M. Davier	1998 [31]

Table 2.1: *First order contributions to* $\Delta a_\mu^{had.\mathcal{O}(\alpha^2)}$. *The higher order contributions are small :* $\Delta a_\mu^{had.}(higher\ order) = -9.0(0.5)\times 10^{-10}(0.77\pm 0.04 ppm)$ *[41] and* $\Delta a_\mu^{had.}(higher\ order) = -10.1(0.6)\times 10^{-10}(0.86\pm 0.05\ ppm)$ *[50]*

[50] yielding

$$\Delta a_\mu(\text{had.}\mathcal{O}(>1)) = -9.0(0.5)\times 10^{-10}\,(-0.77\pm 0.04)\,ppm\,(\text{Kinoshita, 1985}) \quad (17)$$

$$\Delta a_\mu(\text{had.}\mathcal{O}(>1)) = -10.1(0.6)\times 10^{-10}\,(-0.86\pm 0.05)\,ppm\,(\text{Krause, 1996}) \quad (18)$$

A particular difficulty arises in connection with graph (c) in figure 2.2. This hadronic light-by-light scattering graph can unfortunately not be determined employing measured cross-sections. This effect was calculated using a vector dominance model and amounts to [51, 52]

$$\Delta a_\mu(\text{had. light-by-light}) = -5.2(1.8)\times 10^{-10}\,(-0.45\pm 0.15)\,ppm\,(\text{Hayakawa, 1996}) \quad (19)$$

$$\Delta a_\mu(\text{had. light-by-light}) = -9.2(3.2)\times 10^{-10}\,(-0.79\pm 0.27)\,ppm\,(\text{Bijens, 1996}) \quad (20)$$

The comparison between those two results revealed that the η' scalar and axial vector exchange contributions were not included in the analysis from Hayakawa, Kinoshita and Sanda [51]. A reevaluation by Hawakaya and Kinoshita which is including the η' contribution gave [53]:

$$\Delta a_\mu(\text{had. light-by-light}) = -7.9(1.5)\times 10^{-10}\,(-0.68\pm 0.13)\,ppm\,(\text{Hayakawa, 1998}) \quad (21)$$

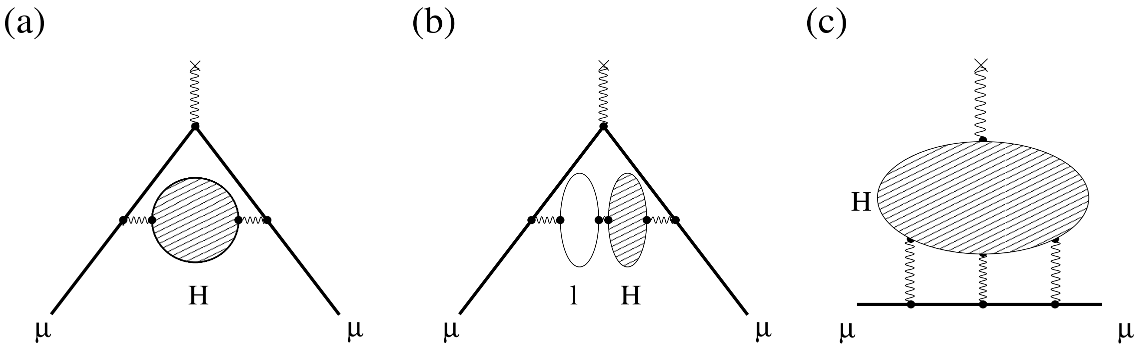

Figure 2.2: *(a) The hadronic vacuum polarisation loop (H) correction to first order. (b) Example of the higher orders where l indicates a leptonic loop. (c) Hadronic light on light scattering. This graph can not be evaluated using experimental cross-sections.*

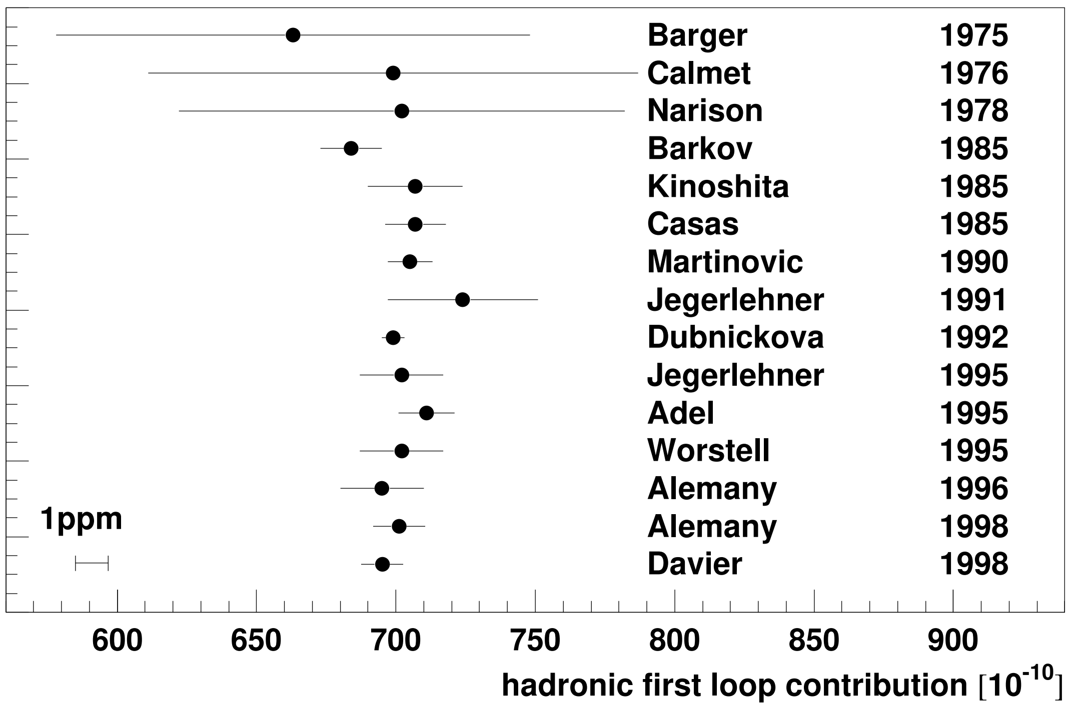

Figure 2.3: *The hadronic first loop correction adds the biggest uncertainty to the theoretical value of a_μ. Further experiments in Dubna, Frascati and Bejing are expected to significantly reduce the uncertainty.*

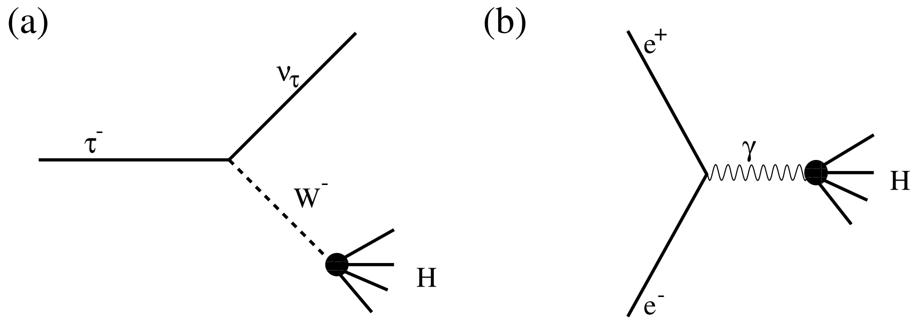

Figure 2.4: *(a) Hadronic τ decay through vector or axial-vector weak current. This decay can be related to the e^+e^- reaction shown in (b).*

final state	energy range (GeV)	contri.	(stat)	(syst)	(rel. err.)	(abs. err.)
ρ	$(0.28, 0.81)$	422.66	5.61	10.62	2.8%	1.7%
ω	$(0.42, 0.81)$	37.76	0.45	1.02	3.0%	0.2%
ϕ	$(1.00, 1.04)$	38.55	0.54	0.89	2.7%	0.2%
J/ψ		8.60	0.41	0.40	6.7%	0.1%
Υ		0.10	0.00	0.01	6.7%	0.0%
hadrons	$(0.81, 1.40)$	112.85	1.33	5.49	5.0%	0.8%
hadrons	$(1.40, 3.10)$	56.43	0.45	7.22	12.8%	1.0%
hadrons	$(3.10, 3.60)$	4.47	0.23	0.86	19.9%	0.1%
hadrons	$(3.60, 9.46)$	14.06	0.07	0.90	6.5%	0.1%
hadrons	$(9.46, 40.0)$	2.70	0.03	0.13	4.9%	0.0%
hadrons	$(40.0, \infty)$	0.16	0.00	0.00	0.2%	0.0%
total		702.35	5.85	14.09	2.2%	2.2%

Table 2.2: *The contributions to the hadronic part of a_μ from resonances and regions between the resonances. The table demonstrates the necessity to obtain additional data in the energy range from $0.28GeV < \sqrt{s} < 3.1GeV$. This energy range is covered by DAΦNE, VEPP-2M and BEPC. The values are taken from Jegerlehner et al. [46].*

in good agreement with Bijens, Pallante and Prades [52]. Presently the total uncertainty off $\Delta a_\mu^{had.}$ is of order $1\,ppm$. For a more accurate value, additional measurements will be necessary to improve the first order calculations. At the level of $0.5\,ppm$ it will be further necessary to reevaluate the hadronic light-by-light contribution.

2.3 Weak Interaction Corrections

The weak interaction contribution based on standard electroweak theory is a weak radiative correction to an electromagnetic interaction and arises in lowest order from the single loop diagrams shown in Figure 2.5. The results for the first order corrections can be calculated analytically [54, 55, 56, 57]

$$\Delta a_\mu(W) = \left(\frac{G_F m_\mu^2}{8\pi^2\sqrt{2}}\right)\left(\frac{10}{3}\right) = +38.9 \times 10^{-10}, \tag{22}$$

$$\Delta a_\mu(Z^0) = \left(\frac{G_F m_\mu^2}{8\pi^2\sqrt{2}}\right)\left(\frac{10}{3}\right)\left[(3 - 4\cos^2\theta_W)^2\right] = -19.4 \times 10^{-10}, \tag{23}$$

$$\Delta a_\mu(Higgs) = \left(\frac{G_F m_\mu^2}{4\pi^2\sqrt{2}}\right)\left(\frac{m_\mu}{m_H}\right)^2 \ln\left[\left(\frac{m_H}{m_\mu}\right)^2\right] \leq 0.1 \times 10^{-10} \text{ if } m_H \gg m_\mu, \tag{24}$$

where G_F is the Fermi coupling constant, θ_w is the Weinberg angle and m_H is the mass of the Higgs-boson. The dependence of the total weak term on the Higgs-boson mass is very weak. The total first order weak contribution is

$$\Delta a_\mu weak\mathcal{O}(1) = 19.5 \times 10^{-10}\ (1.67)ppm. \tag{25}$$

Second order electroweak diagrams are of the order $\alpha \cdot G_F$ and have been calculated

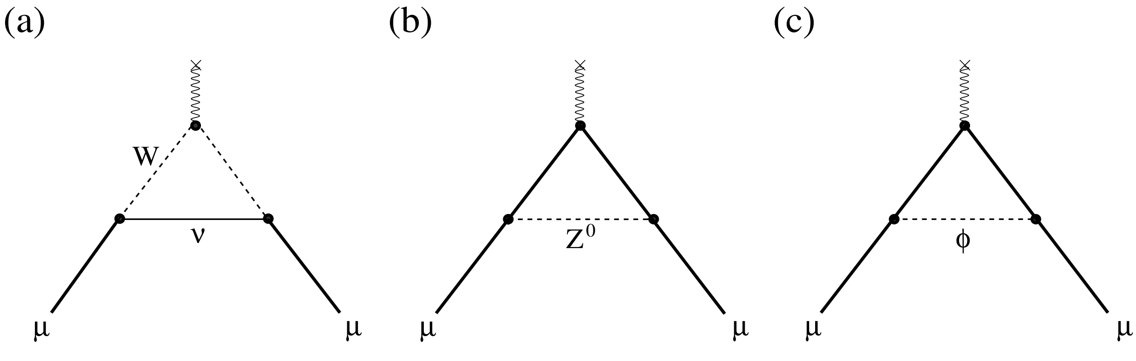

Figure 2.5: *(a) The generation of a virtual W boson which then directly interacts with the magnetic field . (b) The generation of a virtual Z^0-boson and the same graph with the Higgs-boson (c).*

by Kuhto et al. [58]. They have recently been checked by Czarnecki, Krause and

Marciano [59, 60] and independently by Degrassi and Giudice [61]. The sum of all weak contributions is

$$\Delta a_\mu(weak) = (15.1 \pm 0.4) \times 10^{-10}\ (1.30 \pm 0.04)ppm\ \text{(Czarnecki 1995,1996)}, \quad (26)$$

$$\Delta a_\mu(weak) = (15.3 \pm 0.3) \times 10^{-10}\ (1.30 \pm 0.03)ppm\ \text{(Kutho 1992, Degrassi 1998)}. \quad (27)$$

Terms of the order $\alpha^2 \cdot G_F$ have been evaluated and are negligible at present.

2.4 Evidence for New Physics Beyond the Standard Model

Any significant deviation of the measured from the $(g-2)_\mu$ value predicted by the standard model would be a signal for new physics. For example additional new particles would contribute to the $(g-2)_\mu$ value in vacuum polarization loops and would therefore change the value predicted. Of course, the experiment is only able to measure the sign and the size of the difference to the predicted value.
Compared to other experiments $(g-2)_\mu$ is most sensitive to μ and W substructure [62] whereas it is not competitive concerning the Higgs mass.
Within supersymmetric models the $(g-2)_\mu$ value would be sensitive particularly to the vacuum expectation value $\tan\beta$ of the two Higgs fields. The sensitivity is [63]

$$\Delta a_\mu(SUSY) = 140 \times 10^{-11} \left(\frac{100\,GeV/c^2}{\tilde{m}}\right)^2 \cdot \tan\beta, \quad (28)$$

where $\tilde{m}$ is the mass of the lightest supersymmetric particle. At its design accuracy the experiment could rule out large values of $\tan\beta$ respectively give a hint to look for such in dedicated searches.
In table 2.3 the major possible contributions arising from non standard model physics are summarized as described in a review by Kinoshita and Marciano [21].

Sensitivity of a_μ to speculative theories		
	AGS$(g_\mu - 2)$ Limits	Comments / Other experiments
Compositeness:		
Lepton substructure:		
Muon (m_μ^2/Λ^2)	$\Lambda > 5TeV$	LHC similar
μ Form factors $(1 - k^2/\Lambda^2)$	$(W^\pm)\Lambda > 450GeV$ $(Z^0)\Lambda > 64GeV$ $(\gamma)\Lambda > 180GeV$	$\Lambda_{LEPI} > 300GeV$
Excited muon	$m_\mu^* > 400GeV$	LEP II similar
Boson Substructure:		
$W^\pm$	$\Lambda > 400GeV$	LEP II $\sim 100 - 200GeV$
Excited bosons	$m_{Z^*} > 70 - 140GeV$ $m_{W^{\pm *}} > 70 - 140GeV$	LEP II similar LEP II similar
Anomalous magnetic moment of W	$(g_W - 2)/2 \leq 0.02$	$(g_W - 2)/2 \leq 0.05$ LEP II $(g_W - 2)/2 \leq 0.2$ LHC
Extensions of standard model:		
New gauge bosons:		
$Z'(E6, LR)$ $W_R^\pm$ Super-heavy Higgs Light Higgs	$m_{Z'} > 30 - 130GeV$ $m_{W'} > 250GeV$ $m_H > 500GeV$ $m_H > 300MeV$	FNAL $p\bar{p}$ FNAL $p\bar{p}$ $O(g)$ coupling $O(10^{-3}g)$ coupling
Supersymmetry	$> 130GeV$	FNAL $p\bar{p}$
Muon electric dipole moment	$D_\mu \leq 4 \times 10^{-20} ecm$	

Table 2.3: *The sensitivity of a_μ at a level of $0.35\,ppm$ accuracy for effects which occur in several speculative theories is in many cases comparable or better than in the best ongoing or proposed measurements in high energy collision experiments.*

3 The Experiments Measuring the Magnetic Anomaly of the Muon

The motivation for the new $g_\mu - 2$ experiment at BNL (Experiment 821) is measuring the contribution of the weak interaction to the muon magnetic anomaly within the standard model as well as searching for new physics beyond the standard model. The proposed measurement accuracy of $0.35\,ppm$ would allow to verify the weak contribution ($1.3\,ppm$) at the 25 % level and to set stringent limits to many speculative theoretical extensions of the the standard model. Before the experiment was proposed there have been three experiments at CERN to measure the $g_\mu - 2$ value.

3.1 Muon Decay

The first g_μ experiments measured the g factor for muons which decayed at rest by observing the Larmor precession in an external magnetic field perpendicular to the muon spin axis. They used the decay chain :

$$\pi^+ \to \mu^+ + \nu_\mu \quad , \quad \mu^+ \to e^+ + \nu_e + \bar{\nu_\mu}.$$

Both decays are due to the weak interaction and violate parity-conservation [64, 65]. The non-conservation of parity in the first decay leads to the fact that the spin of the decay muon points against its propagation direction. In the second decay the decay-positrons preferably are emitted in the direction of the muon spin. This effect was also used in a series of three CERN experiments and is employed in the new $g_\mu - 2$ experiment at the Brookhaven National Laboratory (BNL). The maximum kinetic energy of the decay positrons or electrons is $E_{max} = 52.3\,MeV$. The probability with which the positron is emitted in a certain direction within a certain energy range can be calculated by integrating over the neutrinos' momenta. The double differential distribution $W(\theta, \epsilon)$ of the decay positrons with respect to the spin of the muon is given by

$$\begin{aligned} \mathrm{d}^2 W &= W(\theta,\epsilon)\,\mathrm{d}\epsilon\,\mathrm{d}\cos\theta \\ &= \frac{G^2 m_\mu^5}{192\pi^3} \cdot (3-2\epsilon) \cdot \epsilon^2 \left[1 + \frac{(2\epsilon - 1)}{3 - 2\epsilon} \cos\,\theta\right] \mathrm{d}\epsilon\,\mathrm{d}\cos\theta, \end{aligned} \tag{29}$$

where $\epsilon = E/E_{max}$ and θ is the angle between the muon spin and the momentum of the emerging positron. The asymmetry in the angular distribution is a consequence of parity violation in the weak interaction. The energy spectrum of the positrons or electrons follows from eq. (29) by only integrating over $cos\,\theta$

$$\mathrm{d}W(\epsilon) = W(\epsilon)\mathrm{d}\epsilon = \left[2(3-2\epsilon)\epsilon^2/\tau_\mu\right] \mathrm{d}\epsilon \quad \text{, with} \quad \tau_\mu = \frac{G^2 m_\mu^5}{192\pi^3}\,. \tag{30}$$

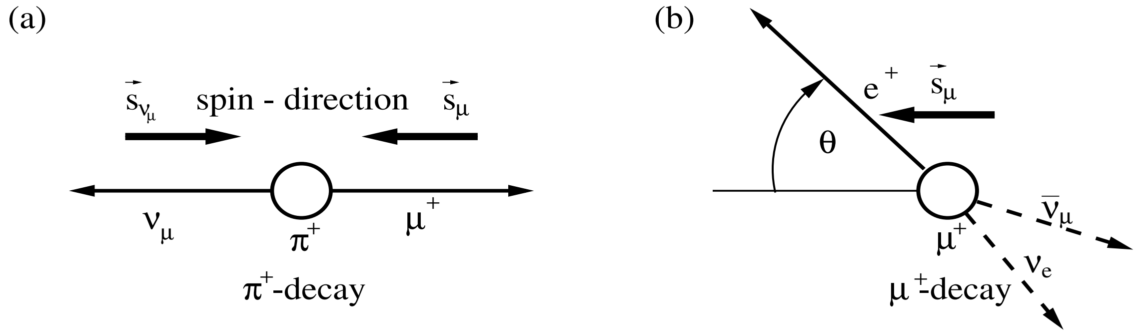

Figure 3.1: *a) pion decay in the pion rest frame, the spin directions $\vec{s}$ are indicated. b) muon decay in its rest frame.*

The asymmetry factor in front of the cosine function in eq. (30) depends on the positron energy and for an ensemble of muons with polarization P the asymmetry is

$$a(\epsilon) = \frac{2\epsilon - 1}{3 - 2\epsilon} \cdot P \quad . \tag{31}$$

Only looking for decay positrons in the same plane as the muon spin gives

$$\frac{dN_{e^+}}{d\theta} \sim (1 + a\cos\theta) \tag{32}$$

and for the decay electrons in the μ^- decay

$$\frac{dN_{e^-}}{d\theta} \sim (1 - a\cos\theta). \tag{33}$$

-integrated over all energies $a = 1/3$. For the highest energies $a = 1$ (see figure 3.2).

3.2 Early Measurements of the Muon g-Factor

The measurement of the spacial distribution of the decay positrons at zero magnetic field reflects the non-conservation of parity. This was experimentally observed by two groups [64, 65] immediately after the discovery of the non-conservation of parity by Wu et al. [66] in nuclear β-decay. If the muon is in a magnetic field perpendicular to the spin direction the expectation value of the spin rotates with the spin precession frequency around the direction of the magnetic field lines:

$$\omega_s = g_\mu \frac{e}{2m_\mu c} \cdot B. \tag{34}$$

The angular distribution in equation (32) and (33) together with the spin precession in equation (34) give an oscillation in the number of decay particles detected in a device of small solid angle positioned to observe them in a direction perpendicular

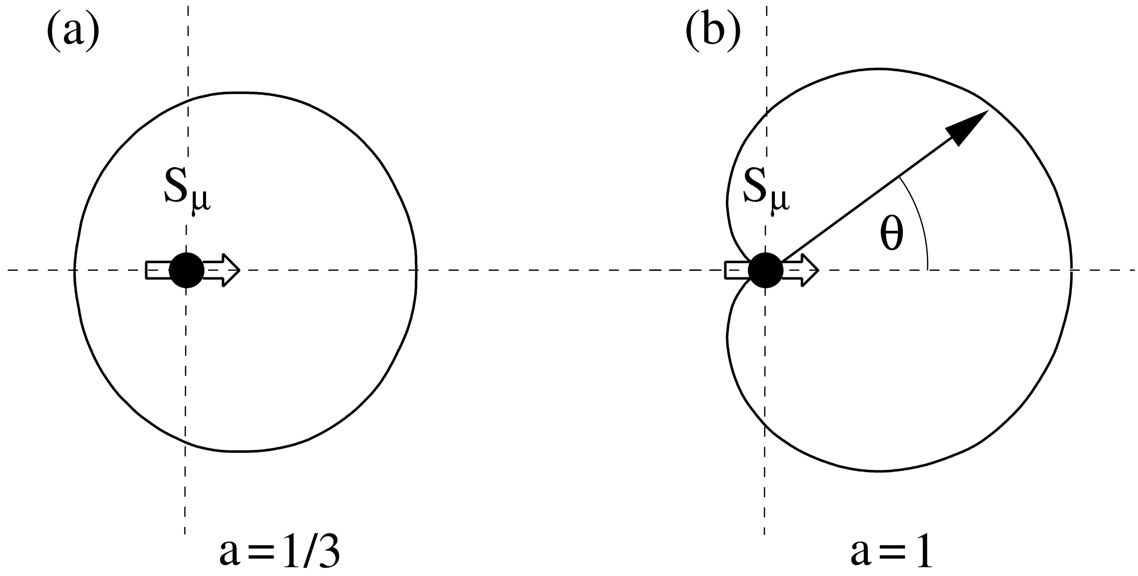

Figure 3.2: *Muon decay. The rate of the decay positrons is given in a polar diagram with an angle θ with respect to the muon spin. (a) Averaged over all positron energies the asymmetry parameter a is $1/3$. For negative muons a is $-1/3$ and the electron is emitted predominantly against the direction of the muon spin. (b) For the highest energy positrons a equals 1.*

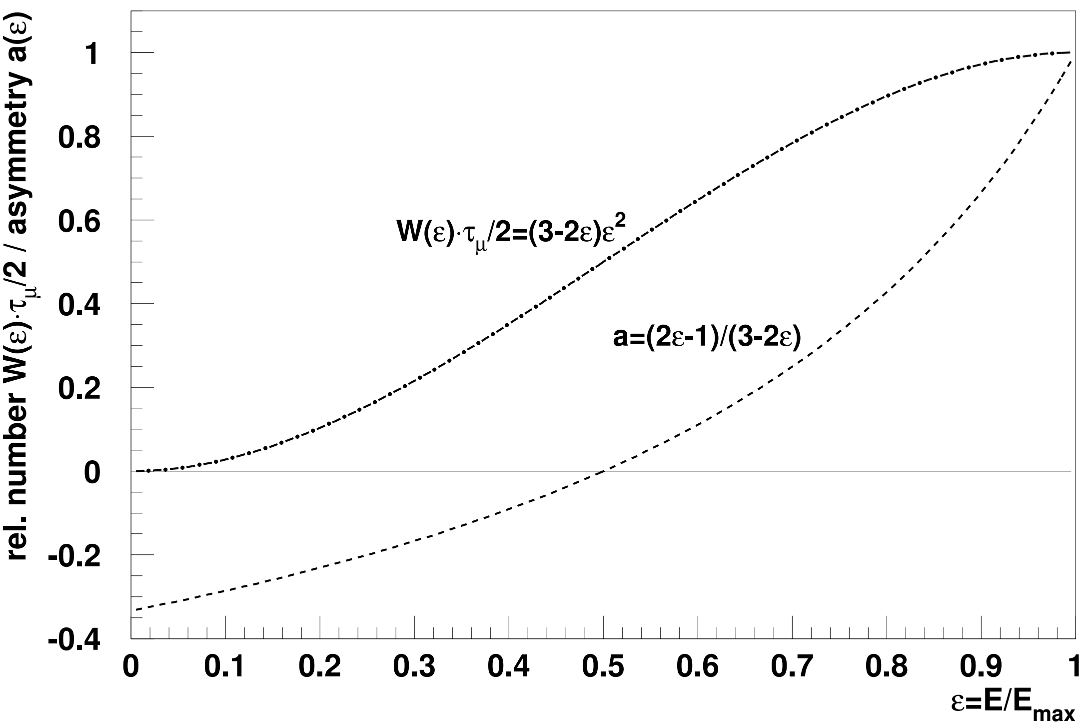

Figure 3.3: *The relative number $W(\epsilon)$ and the asymmetry a of the spatial distribution versus the energy of the decay positrons. For low energy positrons the asymmetry is negative.*

to the magnetic field B. The measurements of Garwin et al. [64] resulted in $g_\mu = 2.0 \pm 0.1$ and showed that the muon is a spin 1/2 particle like the electron. By 1963 the anomaly $a_\mu = (g_\mu - 2)/2$ was known to 15% [67]. The measurement was limited by the knowledge of the muon-mass [68, 69, 70]. For a more precise test of the electron muon universality a new type of measurement was necessary.

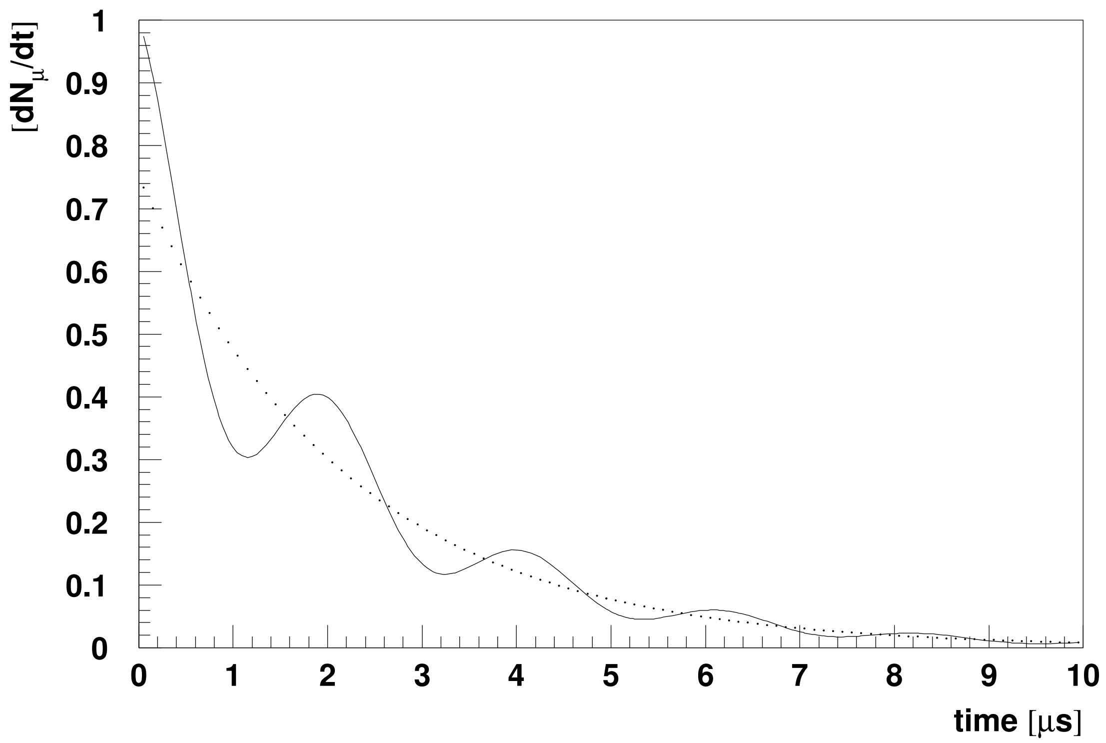

Figure 3.4: *The spin precession of muons in a magnetic field perpendicular to the muon spin axis. An asymmetry $a = 1/3$ corresponding to averaging over all possible energies and* 100% *muon polarization are used. Only decay positrons emitted mostly perpendicular to the magnetic field into a small solid angle are shown. The exponential muon decay is indicated by the dotted line.*

3.3 The CERN g-2(Muon) Experiments

In a low energy regime the cyclotron-frequency of a charged particle is given by $\omega_c = eB/m_\mu c$ and difference frequency

$$\omega_a = \omega_s - \omega_c = a_\mu \left(\frac{e}{m_\mu c}\right) B \quad , \quad a_\mu = \frac{m_\mu c}{eB}\omega_a \tag{35}$$

is directly proportional to a_μ which happens to hold at all energies (see below). Since a_μ is of the order $\alpha/2\pi$, an experiment in which the muons decay in motion in a magnetic field is three orders of magnitude less sensitive to uncertainties in m_μ. The exact knowledge of the magnetic field is crucial because a_μ is inversely proportional to B. In all three CERN $g_\mu - 2$ experiments and also in the new experiment at BNL the nuclear magnetic resonance (NMR) signal of protons was used to measure the magnetic field in the bending magnets

$$B = \frac{\hbar \omega_L}{2\mu_p}, \tag{36}$$

where ω_L is the measured Larmor frequency of the protons in the magnetic field and μ_p is the magnetic moment of the proton. The advantages of this method are the accuracy of NMR measurements as well as the fact that the essential part of the measurement boils down to a comparison between two frequencies: The NMR-frequency of protons in a magnetic field against the $g_\mu - 2$ frequency in the same magnetic field. There are however several difficulties: to store particles in a magnetic field it is necessary to focus the particle beam which is normally done by magnetic quadrupoles. Introducing higher multi-poles to the magnetic field limits the ability to measure $< B >$ since the position of the particles cannot be determined with sufficient precision.

The first experiment [17] used a longitudinally polarized muon-beam with a momentum of 150 MeV/c produced by forward decay in flight of pions from the CERN Synchro-cyclotron. The muons were moderated in a beryllium degrader and were stored in a dipole magnet for about 1000 turns of radius 19 cm. A gradient in the magnetic field caused a slow drift over 600 cm from the injection point to the ejection point. The gradient was small in the middle of the magnet whereas it had to be big at the beryllium-degrader to prevent the muons hitting the degrader again after one turn and at the ejection point to get the muons out of the magnet. After the ejection the muons were stopped in a field free region and the final spin direction was measured by recording the direction of the decay positrons in an elaborate detector system. Although this method was a big improvement compared to the former measurements it faced several problems:

1. The maximal number of turns the muons did in the dipole-magnet was small (≈ 1000) and therefore the total change of the spin direction of the muons was limited. The muon spin turned about 0.4 degree per turn which means that the total rotation angle was about 400 degrees.

2. It was necessary to introduce field gradients to keep the beam in focus which made it difficult to calculate the average B-field the muons saw. There were also big field gradients at the ejection point when the particles left the magnetic field.

3. Finally the count rate was very low since the muons stayed for about 6 μs inside the dipole-magnet and most of them decayed before reaching the detectors.

The final result was

$$a_\mu(\text{CERN I}) = (1162 \pm 5) \times 10^{-6}, \tag{37}$$

which agreed well with the theoretical value of 1165×10^{-6} and improved the accuracy by more than a factor of 10. At that time a_e was measured by Wilkinson and Crane

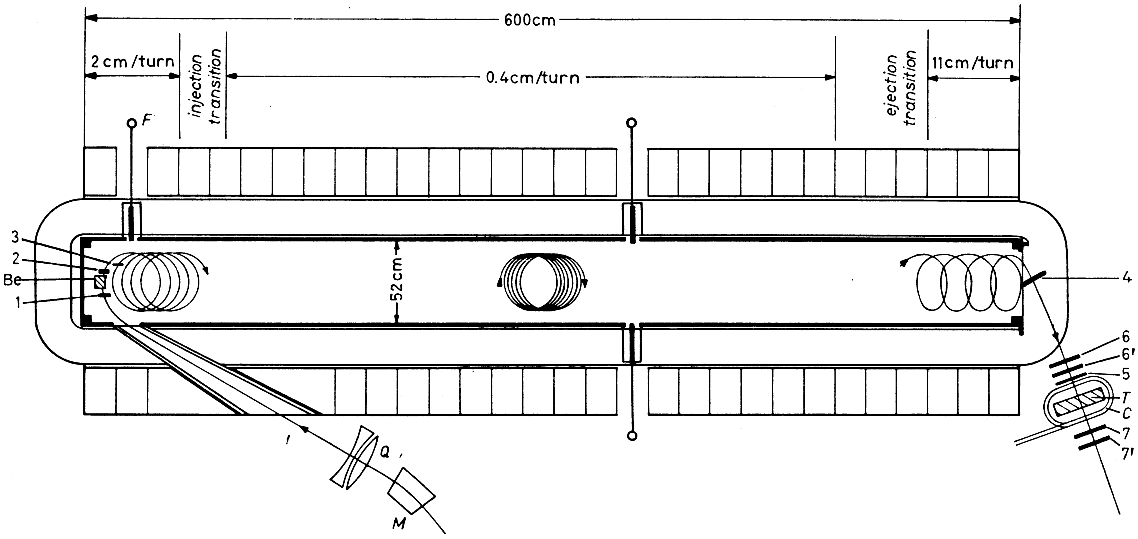

Figure 3.5: *The first $g_\mu - 2$ experiment at CERN [17].*

[71, 72] and the result $a_e^{exp} = (1159.622 \pm 0.027) \times 10^{-6}$ agreed very well with theory $a_e^{theo} = 1159.615$. Both values were identical within a standard deviation of the $g_\mu - 2$ experiment thus strongly supporting the $\mu - e$ universality which stimulated strong interest in a further enhancement of accuracy to see the predicted difference between a_μ and a_e.

In the second CERN experiment the spin precession of muons at $E = 1.27\ GeV/c^2$ (corresponding to $\gamma = (1-\beta^2)^{-1/2} \approx 12,\ \beta = v_\mu/c$) was measured in a storage ring. Equation (35) still holds in the case of relativistic particles. The cyclotron frequency for relativistic particles is

$$\omega_c(rel.) = \frac{eB}{m_\mu c} \cdot \frac{1}{\gamma}. \tag{38}$$

To calculate ω_s the Thomas precession frequency ω_T which arises from the accelerated motion of the particle has to be subtracted from the Lorentz invariant Larmor frequency ω_L

$$\omega_s = \omega_L - \omega_T = 1/2\ g_\mu\ \frac{eB}{m_\mu c} - \frac{(\gamma - 1)}{\gamma} \cdot \frac{eB}{m_\mu c}. \tag{39}$$

This yields to

$$\omega_a = \omega_s - \omega_c = 1/2\ (g_\mu - 2)\ \frac{eB}{m_\mu c} = a_\mu \frac{eB}{m_\mu c}. \tag{40}$$

Therefore this design has several advantages:

The γ times longer muon lifetime as well as the storage ring design were essential for the improvement of the accuracy. In a storage ring with detectors for the decay electrons located inside the ring it is possible to measure a large fraction of all decay $e^\pm$. Almost all decay $e^\pm$ have a lower momentum than the muons, therefore almost all of them are swept to smaller radii where the detectors are located. In the rest frame of the positive (negative) muon the positrons (electrons) are preferably emitted in (against) the direction of the muon spin and their polarization is dependent on their energy. The highest energy positrons (electrons) are all emitted directly in (against) the direction of the muon spin. In the laboratory frame this means that the positrons (electrons) with higher energies were emitted in (against) the spin direction of the positive (negative) charged muon. Therefore it is necessary to measure the energy of the decay electrons and then restrict the observation to the higher energy particles. If the number of detected decay particles is plotted versus time the plot shows the exponential muon decay modulated with the frequency ω_a.

The

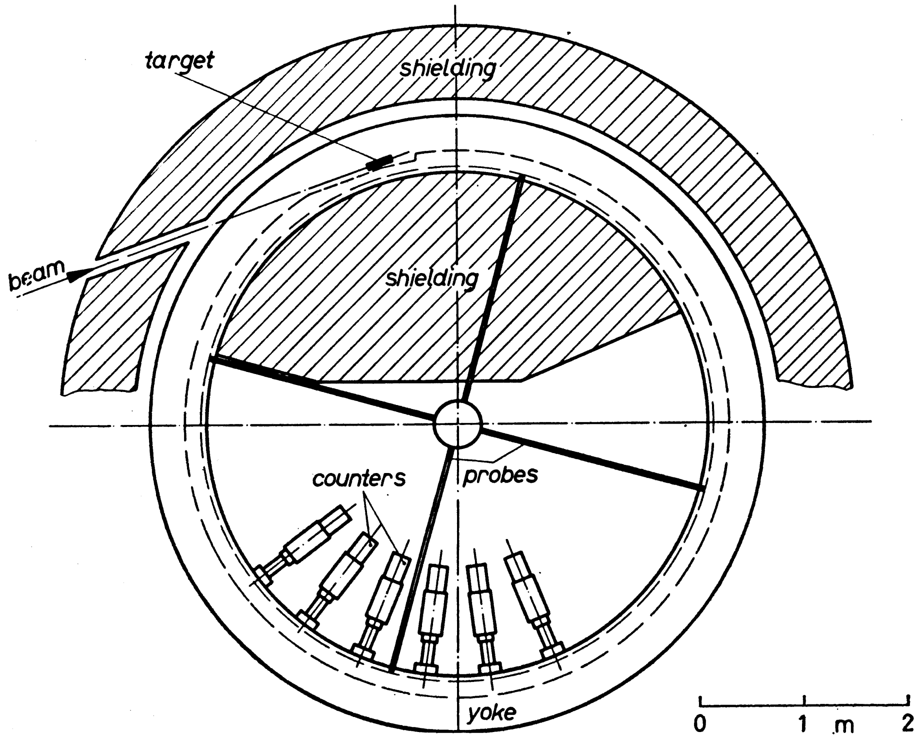

Figure 3.6: *The second $g_\mu - 2$ experiment at CERN. This was the first storage ring experiment. Protons were directly shot at the pion production target inside the ring and muons got produced by pions decaying in flight [73].*

The introduction of higher multi-poles to the magnetic field made it difficult to calculate the average magnetic field for the particles. The position of the stored muons was known to $\pm 3mm$. This made it impossible to determine the average magnetic field seen by the particles to better than $160\,ppm$. Another problem was the production of the muons. A pulsed proton beam was directly shot onto a target inside the ring to produce pions. Some of the pions made about 1/2 turn in the ring and some of those decayed in a way that the decay muons got stored in the ring. The efficiency of this process is very low ($\approx 6 \times 10^{-9}$ per pion leaving the target and $\approx 2.4 \times 10^{-9}$ per incoming proton.) and the background produced by the protons and pions was immense compared to the decay signal of the muons. Therefore it was impossible to evaluate the muon decays within the first $20.5\,\mu s$ after the proton

injection. Another problem associated with this kind of injection was also the low polarization of the resulting muons of only 26 %.
The final result was [73, 74, 75]

$$a_\mu(\text{CERN II}) = (1166.16 \pm 0.31) \times 10^{-8}. \tag{41}$$

When this value was published there was a disagreement between theory and experiment of 1.8 standard deviations. Further calculations showed that there was a sixth order QED correction which was much bigger than originally expected. The leptonic light-by-light scattering graphs equivalent to the hadronic ones shown in figure 2.2 contribute to a_μ much more than previous calculations revealed [76]. After this correction was found the disagreement was less than one standard deviation: $(240 \pm 270 ppm)$. This result was more than a factor of 15 better than the result of the CERN I experiment.
The third CERN experiment [18] had major improvements in two respects: Firstly

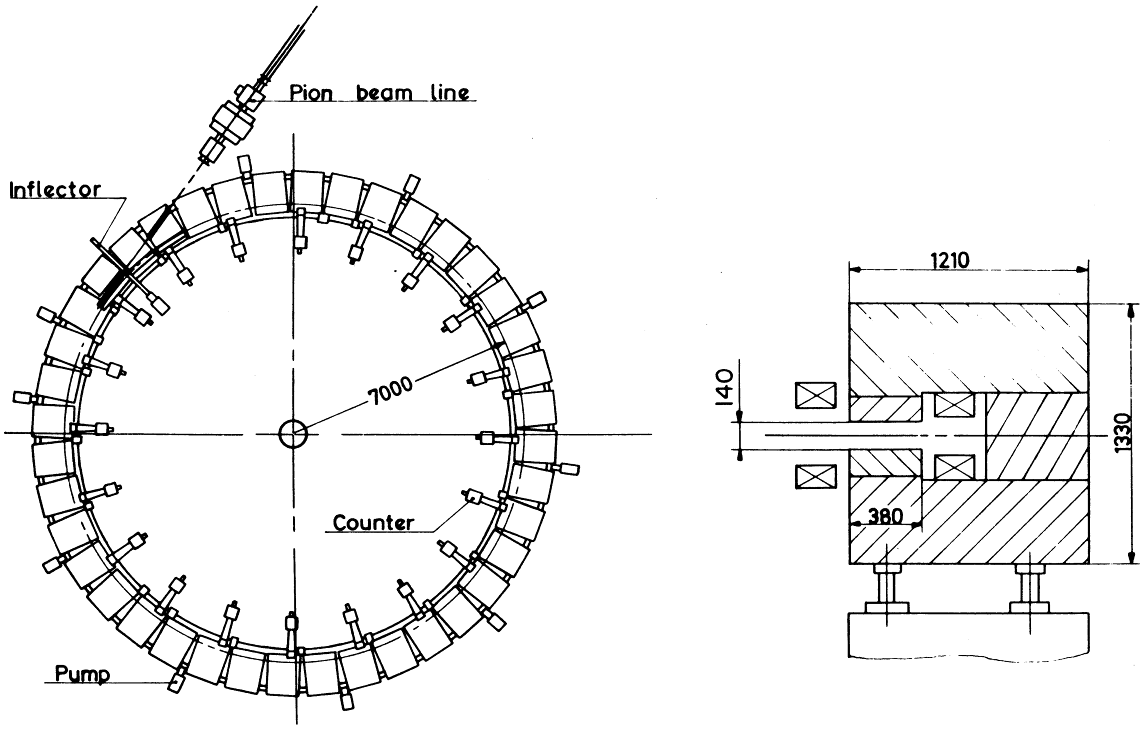

Figure 3.7: *The third $g_\mu - 2$ experiment at CERN. The big improvement of this experiment was the usage of electrostatic fields to focus the muons. At $\gamma = 29.3$ the effect of electrostatic fields on the muon precession frequency cancels out; therefore the experiment was built to run at $3.1\,GeV/c$ [18].*

the particle beam was focused with electrostatic instead of magnetic quadrupoles and secondly the proton target was now located outside the storage ring to reduce the amount of background at early times.
The motion of the muon spin in the combined magnetic field $\vec{B}$ (perpendicular to

$\vec{\beta}$) and electric field $\vec{E}$ now had to be considered. The angular frequency ω_a of the spin relative to the momentum vector for muons of velocity $\vec{\beta}c$ is shifted from the value $(e/mc)aB$ in eq. (35) and is given by

$$\vec{\omega}_a = \frac{e}{mc}\left\{a_\mu \vec{B} - \left[a_\mu - \frac{1}{\gamma^2 - 1}\right]\vec{\beta} \times \vec{E}\right\}, \tag{42}$$

where $\vec{B}$ and $\vec{E}$ are the magnetic and the electrostatic field respectively and $\vec{\beta} = \vec{v}/c$. However the additional term with the electric field cancels out for

$$\gamma = \left(1 + \frac{1}{a_\mu}\right)^{1/2} \approx 29.304 \text{ (magic gamma)} \tag{43}$$

which corresponds to $p_\mu = 3.0944\, GeV/c$. This fact was used in third CERN experiment and is also used in the new $g_\mu - 2$ experiment at BNL. The fact that the muons are highly relativistic adds another advantage: Since the relative precession frequency ω_a is independent of γ more periods of the $g_\mu - 2$ oscillation can be observed due to the dilated muon lifetime.
The CERN III experiment used a pulsed inflector magnet to inject pions into the ring. The pions decayed in flight and a fraction of the decay muons got stored in the storage ring. This injection method gave a polarization of 95%. To measure the magnetic field a detailed field-map using NMR-magnetometers was taken at the beginning and at the end of each measurement cycle with the vacuum-chambers removed. The magnet had to be turned off and on again to remove or reinstall the vacuum-chambers. There were 37 NMR-probes which could be moved inside the vacuum-chambers during the runtime. About 400 data points were taken and these values were compared with the field-maps taken before the vacuum-chambers were mounted. This allowed to track the field with sufficient accuracy. The experiment measured both positive and negative muons and got $a_{\mu^-} = 1165937(12) \times 10^{-9}$, $a_{\mu^+} = 1165911(11) \times 10^{-9}$ and the combined result

$$a_\mu(\text{CERN III}) = 1165924(8.5) \times 10^{-9}. \tag{44}$$

This improved the accuracy by another factor of 35 compared to the last measurement. The total number of measured muons set a limit to this experiment, without a significant increase in the number of stored muons it was not possible to further improve this result.

3.4 The New BNL g-2(Muon) Experiment

The new $g_\mu - 2$ experiment at the Brookhaven National Laboratory has as its ultimate goal a reduction of the uncertainty in a_μ by factor of 20 and uses the powerful storage ring method developed at CERN. To achieve this goal there were several improvements necessary. The muon rate needs to be higher by at least a factor of 100 compared to the last CERN experiment and also the magnetic field has to be more uniform and stable. This requires the field to be measured more frequently. In addition, the timing of the detector stations and the readout electronics had to be improved for better energy and time resolution at higher rates.
The Alternating Gradient Synchrotron (AGS) at BNL delivered up to 60×10^{12} protons at 25 GeV/c per cycle in 1997, which is about a factor of 200 more compared to the CERN Proton Synchrotron (CPS) at CERN in 1978.
There are two ways to store muons in the storage ring. In both cases the primary

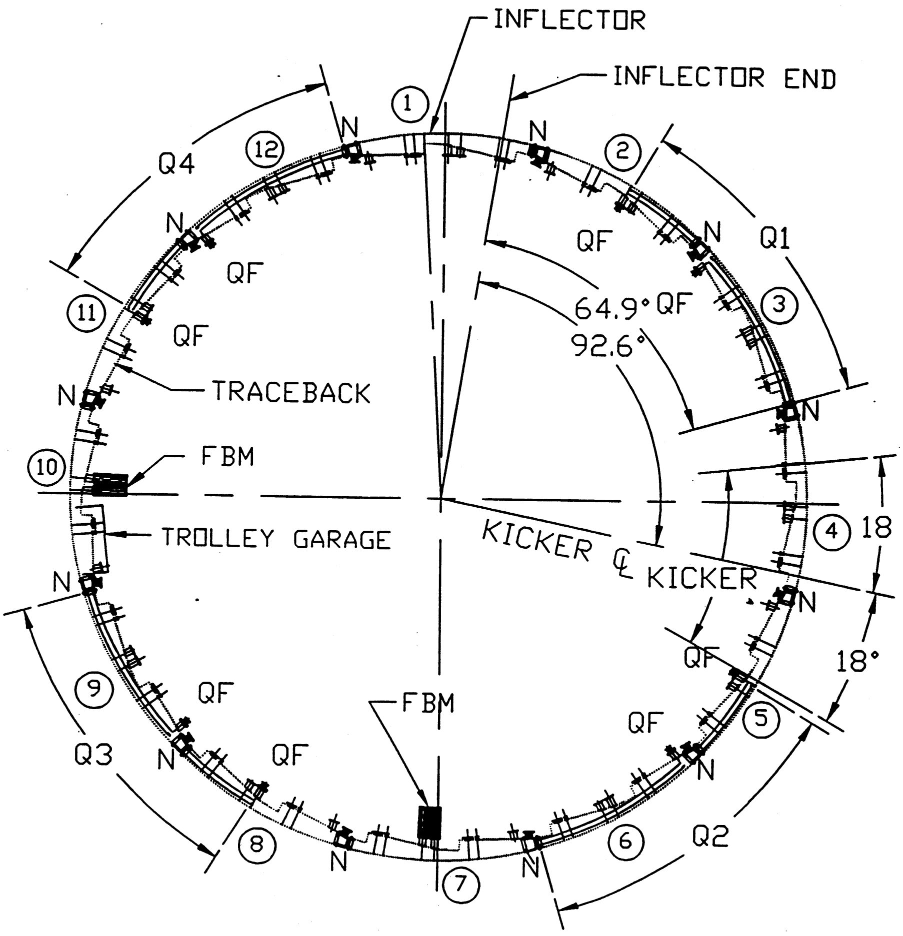

Figure 3.8: *The basic geometry of the new $g_\mu - 2$ experiment storage ring at BNL. The vacuum tank with a scalloped shape is indicated. The relative position of the various key elements are given. The magnetic field is perpendicular to the ring plane.*

proton beam passes through a water cooled pion production target made of nickel with a thickness of about $30\,cm$. With a dipole magnet $3\,GeV/c$ pions are separated from protons and other particles and are transported through a $122\,m$ long transfer beam-line. During this time a substantial fraction of the pions can decay to muons (38 % whereas 50 % of the original pions will survive [77]), thus providing either pions or muons to inject into the storage ring. For injection a superconducting static inflector magnet is used which compensates the field near to the storage region and allows to bring the particles tangentially through the yoke from the outside into the toroidal storage volume.

- If pions are injected, some of them will decay during the first turn and some of the decay muons will be stored. The efficiency of this mechanism is rather low, calculations give about 2×10^{-5} [78] per injected pion in the right momentum range. This is about 50 % less than the efficiency of the CERN III experiment due to the static inflector and the longer beam-line.

- Direct muon injection into a homogeneous magnetic field would not work since the particles would leave the storage volume again after at most one turn. Therefore a pulsed muon 'kicker' has been built to sweep the muons to the right storage position. Direct muon injection is expected to increase the rate of stored muons by a factor of 10 and also greatly reduces the background in the particle detectors which during pion injection dominantly arises from decaying pions, neutrons and gammas.

The magnet has a super-ferric design, which means that the field is provided by superconducting coils but shaped by steel. Four coils of $\approx 14\,m$ diameter are used and the iron is mounted to give one single block with full azimuthal symmetry. This design offers higher field stability compared to the non-superconducting magnet assembly at CERN which consisted of 40 individual dipole magnets while it still allows many ways to adjust the field homogeneity. The shimming is done by adding and removing iron at various locations and also by electrically excited correction coils. Field-maps of the magnetic field can be taken daily without breaking the vacuum and field changes between two field-maps are monitored by 366 fixed NMR-probes which are embedded in the top and bottom plates of the vacuum-chambers.
The detection of the decay electrons (positrons) is done by calorimeters which are made of $1\,mm$ scintillating fibers embedded in a lead block [79, 80]. There are 24 calorimeters inside the storage ring magnet, one every 15 degrees. The active volume of each is $22.5\,cm$ wide, $14\,cm$ high and $15\,cm$ deep, the scintillating fibers make up 35 % of the volume and the radiation length is about $1\,cm$. The active volume consists of four separately-constructed modules which are glued together and read out separately. The depth of approximately 15 radiation lengths is enough for a reasonable containment of the showers. The energy resolution is $\sigma = 10 - 13\,\%/\sqrt{E/GeV}$. Solid acrylic light couplers with a surface area of $7.5 \times 8.0\,cm^2$ have been designed to gather the light from the ends of the calorimeter and bring it to a two-inch round acrylic light-pipe. The light coupler has been measured to have a very uniform acceptance with deviations of only 1 % [81]. The four light-pipes undergo a 90 degree

bend and extend to the photomultipliers located $1\,m$ below the midplane on the bottom of the detector station. The magnetic field is already below $100\,G$ where the photomultipliers are located and since the photomultipliers are far away from the precision magnetic field in the storage region it can be further reduced by screening them with additional iron thus improving gain and timing stability. Another advantage of the bent light-guide is the reduced background due to scattered particles hitting the vacuum-chamber walls or the magnet. This is particularly important for pion injection where the pions produce a large background. A $2\,GeV$ electron will produce about 500 photoelectrons in the photocathode of the photomultiplier tube. Based on various tests the Hamamatsu R1828-01 photomultiplier tube has been chosen for the calorimeters. It is a 12 stage tube with $53\,mm$ diameter and a rising time spread of only $28\,ps$ for 500 photoelectrons. The bases for the photomultipliers were developed at Boston University and they have two interesting features:

- They are transitorized to keep the voltage stable even at high photocurrents. This is necessary because after injection the signal is much bigger than at the end of the measurement. If the voltage was not stable there would be timing and gain instabilities.

- They can be gated; this means that the voltage between 2 stages can be turned off and on again very quickly. This is necessary to limit the current during the pion-flash directly after injection. Unfortunately it is not possible to gate the first stage since it takes too long to charge and discharge the photocathode which has a rather high capacity and resistance. Instead the voltage between the 4th and 7th stage is turned off. This reduces the effect of the flash but still the photocathode is discharged due to the large number of photons reaching the photomultiplier-tube during injection. Gated photomultiplier-tubes were first developed for the the CERN II ($g_\mu - 2$) experiment in 1964 [82].

Additionally in front of the calorimeters there are front scintillating detectors (FSD). They consist of 5 radially oriented scintillating fingers on top of each other, each made of 3/8 inch scintillator and measuring $2.8\,cm \times 23.0\,cm$. Together they cover the entire front face of the calorimeter. Light-guides of 1 inch diameter and about $1.5\,m$ length connect the scintillators to the phototubes located at the bottom of the detector stations. At the end of the light-guide there are about 200 photons per $2\,GeV$ electron detected in the photomultiplier. The Hamamatsu R1355 10 stage $28.5\,mm$ diameter photomultiplier-tube is used. The rise time spread for 200 photons is $46\,ps$. The FSDs are used for pileup detection and to get position information about the decay electrons (positrons). This information can be used for searching a finite electric dipole moment of the muon through a time dependent vertical asymmetry.

On four stations there are also position sensitive detectors (PSD) which are able to determine the position where the decay electrons (positrons) enter the calorimeter in two dimensions. They are scintillator hodoscopes composed of a x-plane and a y-plane with $7\,mm$ spacing each. The detection of the photons is done with segmented photomultipliers which combine good quantum efficiency with small crosstalk between the channels and stable timing.

In 1997 only calorimeter data was used to determine the frequency ω_a. The other detectors were operational but are not very well suited for pion injection runs with large background. The output of the calorimeters is divided and read out by custom made 8 bit VME wave form digitizer boards (WFD) [83] and LeCroy CAMAC FERA ADCs. The WFDs are used as multi-hit ADCs and sample the sum signal of the four photomultipliers at each detector station at a rate of 400 MHz. Once every storage ring fill a laser calibration pulse is fired and distributed to all photomultipliers at each detector station. This signal is measured by both the wave form digitizers and the FERA ADCs and used to monitor the response of the photomultipliers. The FERA ADCs provide a high resolution measurement of the pulse height whereas the wave form digitizer data is used to determine possible timing shifts.
Additionally a completely independent calibration system using LEDs located at the light guide of each photomultiplier is available to cross-check the results.
The wave form digitizers are optimized to have very little timing shifts. To keep the systematic error in ω_a below $0.1\,ppm$, as proposed, systematic timing shifts have to be less than $20\,ps$ over a $200\,\mu s$ period. An external clock is used to provide the timing for all wave form digitizers. It is locked to the same LORAN C frequency standard as the NMR reference frequency. LORAN C is a navigation network which in particular broadcasts time reference signals derived from a network of atomic clocks. The receiver stability is better than 10^{-11} short term and 10^{-12} long term.

4 The Magnetic Field Measurement System

In order to obtain a_μ from eq. (35) it is necessary to know the average magnetic field with an accuracy exceeding the one of ω_a. The magnetic field measurement system in the BNL $g_\mu - 2$ experiment E821 is newly designed to provide a knowledge of the field at every point in the storage region to better than $0.05\,ppm$ and the field integral $\int \rho_\mu(\vec{r})B(\vec{r})\, d^3r$ to better than $0.1\,ppm$, where $\rho_\mu(\vec{r})$ and $B(\vec{r})$ are the muon density and the magnitude of the magnetic field at location $\vec{r}$ respectively. This exceeds the accuracy of commercial devices by more than one order of magnitude. The best commercial device available today originates from the CERN III $g_\mu - 2$ experiment's field measurement system.

In the framework of this thesis the complex measurement system has been built and implemented. The field measurements were used in shimming the magnet and for evaluating the $g_\mu - 2$ measurements made so far.

The new system consists of two parts. There is a NMR-magnetometer based on pulsed nuclear magnetic resonance with 17 probes built into a vacuum-tight vessel that can be moved through the entire muon storage region along the ring. This NMR-Trolley is used to obtain the magnetic field within the μ storage region to get a complete field-map every 24 to 72 hours. Between these measurements the drift of the magnetic field is monitored by 366 fixed NMR-probes which are distributed to locations outside the vacuum vessel above or below it. Due to the fact that the probes are inaccessible when the vacuum-chambers are mounted, the system was equipped with a 3 fold overdetermination, as the probes itself are rather inexpensive.

In future there are further forseen three additional probes which can plunge into the vacuum vessel. Two of them can measure the magnetic field at different radial positions and one can move both in the radial and in the vertical direction. They will be used to calibrate the NMR-Trolley in absolute terms to better than 10^{-7}, and to cross-check the calibration after every field map.

4.1 Nuclear Magnetic Resonance

The magnetic anomaly a_μ as described in equation (35) by the measured values of ω_a and B can be expressed equivalently by

$$a_\mu = \frac{R}{\lambda - R}, \tag{45}$$

where

$$R = \frac{\omega_a}{\omega_p} \tag{46}$$

and

$$\lambda = \frac{\omega_s}{\omega_p} = \frac{\mu_\mu}{\mu_p}, \tag{47}$$

where μ_p is the magnetic moment of the proton and μ_μ is the magnetic moment of the muon. The strength of the magnetic field is proportional to the Larmor frequency of free protons ω_p as determined in the NMR measurements. Since it is possible to measure frequencies with very high precision, a measurement of this frequency provides a very accurate method to determine the strength of magnetic fields.
Nuclear magnetic resonance (NMR) measurements can be conducted with all nuclei with nuclear spin $\vec{I} \neq 0$. These nuclei also have a magnetic moment:

$$\vec{\mu} = \gamma_I \hbar \vec{I} = \gamma_I \vec{L}, \qquad \gamma_I = \frac{|\vec{\mu}|}{\hbar |\vec{I}|} \qquad \text{gyromagnetic ratio.} \tag{48}$$

The Hamiltonian $\mathbf{H}$ for a nucleus with magnetic moment $\vec{\mu} = -\gamma_I \hbar \vec{I}$ in a magnetic field $\vec{B_0} = (0, 0, B_0)$ is:

$$\mathbf{H} = -\gamma_I \hbar \vec{\mathbf{I}} \cdot \vec{B_0} = -\gamma_I \hbar \mathbf{I_z} B_0. \tag{49}$$

The eigenfunctions of $\mathbf{H}$ are the eigenfunctions of the angular momentum operator $\mathbf{I_z}$ with the eigenvalues $m = I, I-1, ... - I+1, -I$. The energy eigenvalues are $E_m = -\gamma_I \hbar B_0 m$. The energy difference between two neighboring energy eigenstates therefore is :

$$\Delta E = \hbar \omega_L, \qquad \omega_L = \gamma_I B_0 := \text{Larmor frequency} \tag{50}$$

In the case of the proton there are just 2 energy eigenvalues $E_{\pm 1/2} = \mp 1/2 \gamma_I \hbar B_0$. The energy difference ΔE is very small compared to thermal energies ($\Delta E \approx 10^{-5} \cdot kT$ for $B = 1.5T$). Therefore both energy levels are normally almost equally populated at room temperature.
In a macroscopic sample of N nuclei the sum of the magnetic momenta in thermal equilibrium is [84, 85]

$$\vec{M_0} = \sum_{i=1}^{N} \vec{\mu}_i = \frac{N \hbar^2 \gamma_I^2 I(I+1)}{3kt} \cdot \vec{B_0} = \chi_{0n} \vec{B_0} \tag{51}$$

where χ_0 is the static nuclear susceptibility. The proportionality of χ_0 to $1/T$ is the well-known Curie law. Since the nuclear susceptibility is proportional to the square of the elementary nuclear moment $\hbar^2 \gamma_I^2 I(I+1)$, it is very small compared to the electronic paramagnetic susceptibility ($\chi_{0n} \approx 10^{-7} \chi_{0e}$). The time evolution of the expectation value $< \vec{M} >$ can be calculated using classical equations of motion since the value is a macroscopic quantity. In thermal equilibrium the magnetization $\vec{M}$ points in the direction of the external magnetic field to minimize the total amount of energy. To excite the NMR-probe it is necessary to turn the direction of $\vec{M}$ away from the direction of the magnetic field. Then $\vec{M}$ starts to rotate around the direction of the magnetic field and electromagnetic radiation is emitted.
For exciting the NMR-signal a circular polarized high frequency field perpendicular to the static magnetic field gets superimposed $\vec{B_1} = (B_1 \cos(\omega t), -B_1 \sin(\omega t), 0)$. This high frequency field imposes a torque

$$\vec{D} = \vec{M} \times \vec{B}, \qquad \vec{B} = (B_1 \cos(\omega t), -B_1 \sin(\omega t), B_0) \tag{52}$$

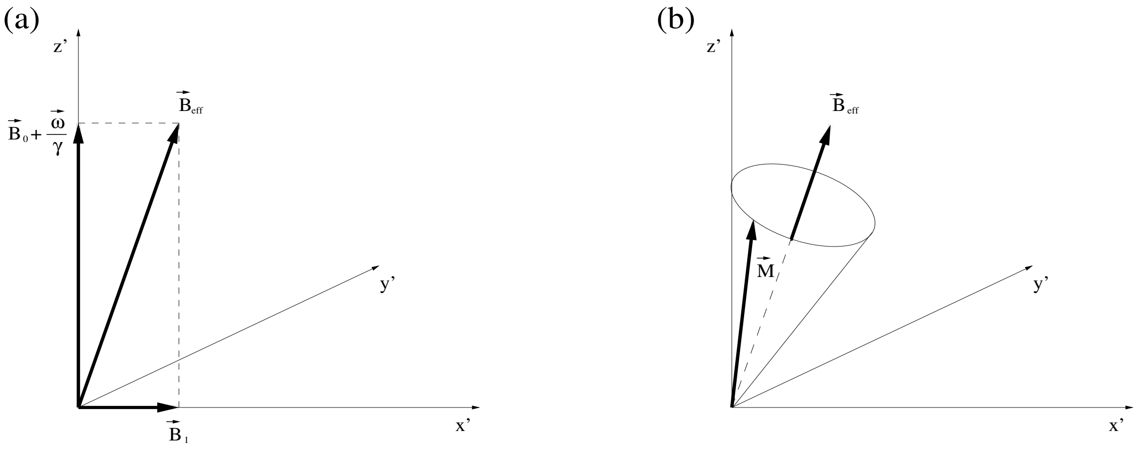

Figure 4.1: *(a) In the rotating coordinate system the effective magnetic field points in the direction of $\vec{B}_{eff}$ if additional to the static magnetic field a circular polarized magnetic field in perpendicular direction is applied. (b) If the frequency of the circular magnetic field is the Larmor-frequency the z' component of $\vec{B}_{eff}$ vanishes and the magnetization turns around the x' axis. The magnetization can be turned by 90 degrees if the HF-signal is only applied for a short time.*

which causes a temporal change of the magnetization $\vec{M}$

$$\frac{d}{dt}\vec{M} = \gamma_I \cdot \vec{D}. \tag{53}$$

Transformation in a coordinate system which is rotating with frequency $\vec{\omega} = (0, 0, -\omega)$ gives

$$\left(\frac{\partial \vec{M}}{\partial t}\right)_{rot} = \gamma_I \vec{M} \times \left(\vec{B}_r + \frac{\vec{\omega}}{\gamma_I}\right) = \gamma_I \vec{M} \times \vec{B}_{eff}. \tag{54}$$

where $\vec{B}_r = (B_1, 0, B_0)$ and $\vec{B}_{eff} = (B_1, 0, B_0 - \frac{\omega}{\gamma_I})$. In the rotating coordinate system with the coordinates x', y' and z' the magnetization precesses about an effective magnetic field $\vec{B}_{eff}$ (See fig 4.1). In the resonance case for $\omega = \omega_l = \gamma_I B_0$ the z' component of $\vec{B}_{eff}$ vanishes and $\vec{M}$ rotates about the x'-axis with frequency $\omega_1 = \gamma_I B_1$.
If the high frequency magnetic field is just applied for some time, it turns the magnetization $\vec{M}$ by an angle α about the x'-axis:

$$\alpha = \gamma_I B_1 t_p, \qquad t_p = \text{pulse length} \tag{55}$$

t_p can be chosen to turn $\vec{M}$ by 90 degrees. Then $\vec{M}$ points in the direction of the y' axis. In the non-rotating coordinate system $\vec{M}$ then precesses with the frequency $\omega_l = \gamma_I B_0$ around the magnetic field axis ($\vec{B} = (0, 0, B)$).
The pulse amplifiers used in the $g_\mu - 2$ experiment have a power of about $20\,W$. The pulse-length is about $5\,\mu s$ to obtain a 90 degree rotation.
Relaxation effects cause the magnetization to go back to the thermal equilibrium

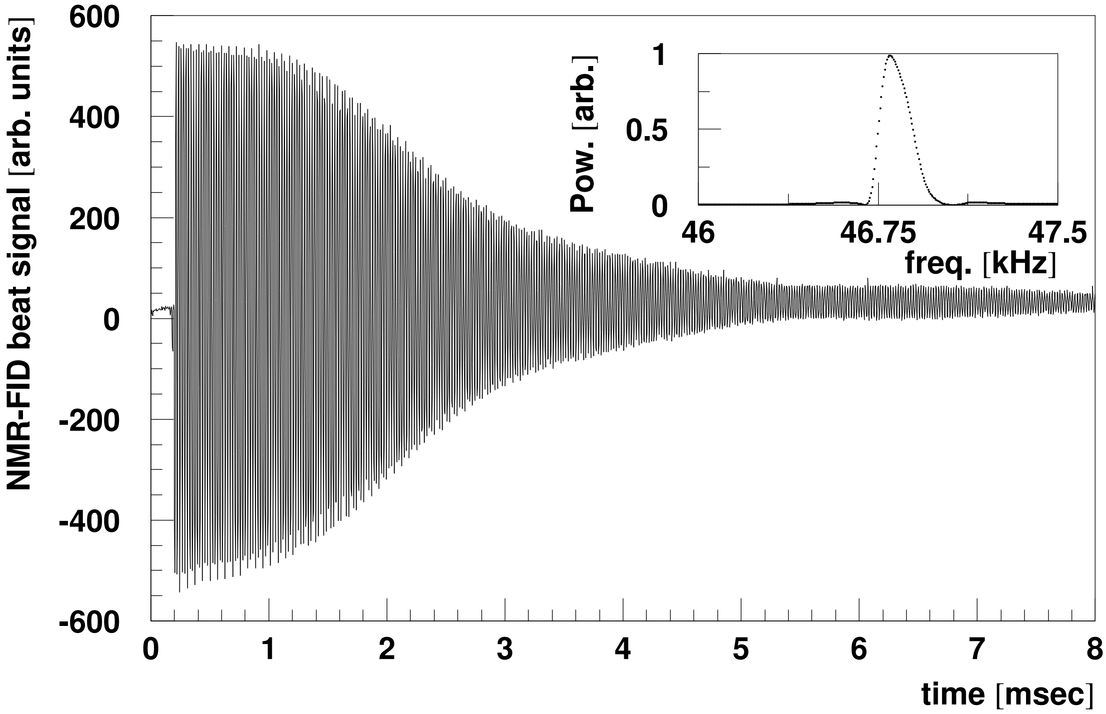

Figure 4.2: *The free induction decay (FID) signal measured with one of the fixed probes. The Fourier power spectrum is indicated in the upper right corner. Since the magnetic field is not homogeneous, the line shape is not symmetric [86].*

value. The time constant of these effects in a very homogenous magnetic field is of the order 3 seconds for a pure water sample. The natural line width is about $2\pi \times 0.1\,Hz(2.5\,ppb)$ [87]. The effect can not be explained by the process of spontaneous emission, the transition probability is only of the order of $10^{-24}s^{-1}$. The lifetime is instead limited by local magnetic field fluctuations due to interaction with other magnetic moments in thermal motion in the same frequency range as the Larmor frequency. The signal is called free induction decay signal (FID).

Since a measurement of about 1 ms is sufficient to reach the proposed accuracy of 0.05 ppm per single shot, it is desirable to reduce the length of the NMR-signal further to be able to work with a higher repetition rate. In the experiment the signal length is reduced by diluting $CuSO_4$ in the water sample. A Cu^{2+} concentration of about 1.5×10^{19} cm^{-3} leads to relaxation times of about 30 ms. Since the frequency of the signal is in the MHz range it is common to look at the beat signal between a reference frequency and the NMR-frequency ($\omega_{beat} = \omega_{NMR} - \omega_{ref}$) and to refer to this signal as FID signal. Figure 4.2 and 4.3 show such a beat signal taken with a probe mounted on top of the vacuum chambers inside the BNL Exp. 821 ($g_\mu - 2$) magnet. The magnetic field is inhomogeneous in this region. The variation of the magnetic field value causes the envelope of the NMR signal to deviate from a pure

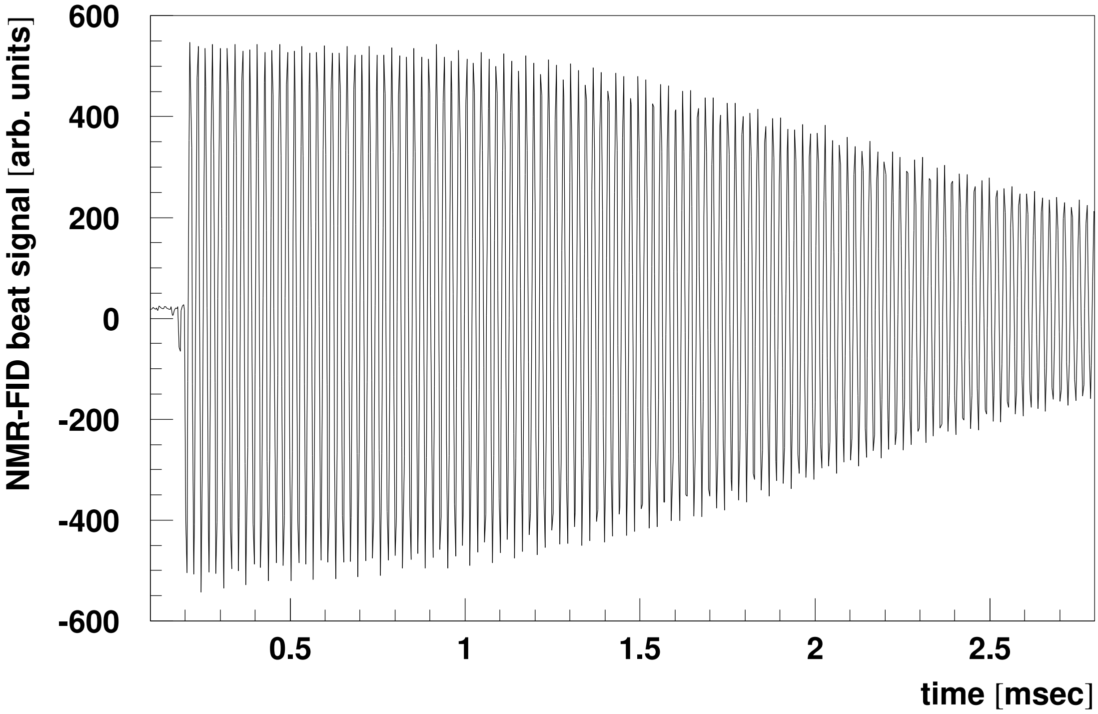

Figure 4.3: *The first 2.7 milliseconds of the same FID signal. This part is used to determine the NMR-frequency. The total length of the signal depends on the homogeneity of the magnetic field at the probe location. The measurement is terminated when the amplitude of the signal is less than* 1/3 *of the amplitude at the beginning of the measurement.*

exponential function. The nuclei at different positions of the probe get out of phase (and in phase again) due to their different Larmor frequency.

4.2 Magnetic Field Measurement and Control Electronics

The magnetic field readout and control system consists of 3 parts:

1. The custom made power supply B-MN 5V/6500A manufactured by Bruker Analytische Meßtechnik GmbH and the current transducer Ultrastab 861^R made by Danfysk.
2. The NMR-measurement system for the fixed NMR-probes and the NMR-Trolley
3. The custom made 88 channel power supply system to power active correction coils.

The $5\,V$ $6500\,A$ Power supply made by Bruker is a custom modified version of a commercial power supply. It offers current stability together with a sophisticated readout and control system. The current can be set by a 14-bit ADC and there is an analog input to make fine-adjustments. The measured temperature drift is less than 5 $ppm/°C$. This value is confirmed by measuring the magnetic field with the NMR-system and using the additional external current transducer made by Danfysk. Since it is possible to stabilize the temperature of the cooling water to 0.1 $°C$ the current is already very stable without additional feedback loop. In 1998 it is planned to introduce feedback from the NMR-system to further improve the stability of the magnetic field. Since this feedback is obtained by measuring the magnetic field in the magnet it also takes the thermal movements of the magnet into account and keeps the dominating dipolar component of the magnetic field constant.

4.2.1 NMR-Probes and Pulse Excitation

The NMR system uses a pulsed NMR technique. The nuclear spins of the water sample in the probe (see figure 4.4) are excited by a pulse of $5\,W$ and $10\,\mu s$ ($10\,W$ and $7\,\mu s$ for the fixed probes) length applied to the resonance circuit formed by the 2 coils with inductances L_s and L_p and a capacitance C_s made by the Al-housing and a metal electrode. The NMR-signal is picked up by the same resonance circuit. A duplexer (see figure 4.5) is used to decouple the typically μV signal from the pulse amplifier. The basic properties of these subsystems were investigated carefully by Prigl et al. [88, 89]. The electronics for the fixed probes NMR-system is located in the

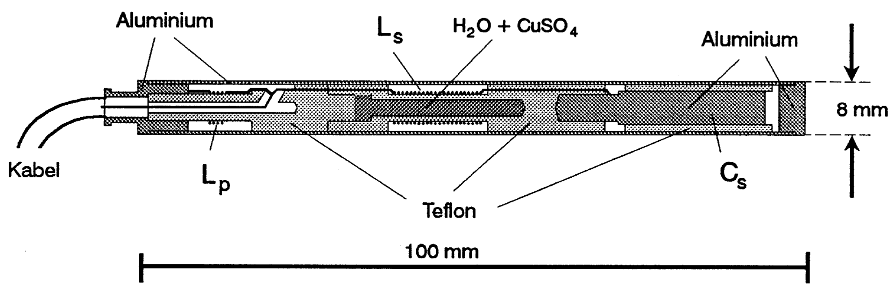

Figure 4.4: *NMR-Probe. The resonance circuit is formed by the 2 coils with inductances L_s and L_p and a capacitance C_s made by the Al-housing and a metal electrode.*

control room far away from the magnet, only the multiplexer units are located near to the magnetic field. Therefore (magnetic) commercial circuits like the UTO 101 amplifier and ASK 1 mixers could be used to amplify and mix the signal whereas the Trolley electronics consists of carefully selected non-magnetic discrete parts. Also the power consumption of the preamplifiers used in the fixed-probe NMR-system would have been prohibitive. The circuit diagrams of the trolley are shown in Appendix A.

The NMR-frequency is measured by a counter counting the zero crossings of the low frequency ($10 - 100\,kHz$) FID-signal and simultaneously counting cycles of a

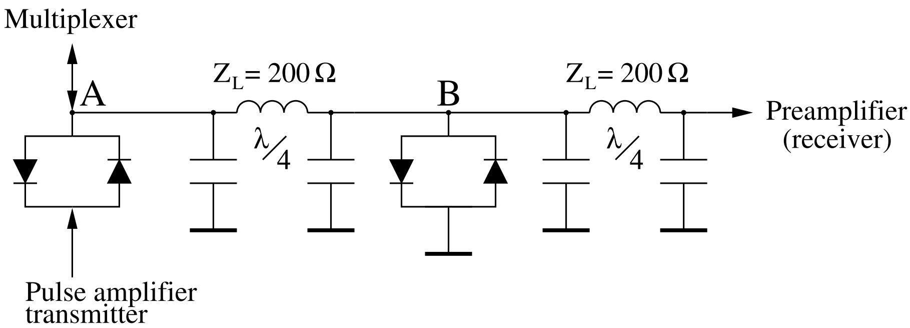

Figure 4.5: *The duplexer. During the pulse the pairs of crossed diodes represent a short circuit. The $\lambda/4$ line between A and B transforms the short circuit at B to a high impedance at A. For the weak NMR signal the duplexer acts as a pure $\lambda/2$ line between probe and preamplifier [88, 89].*

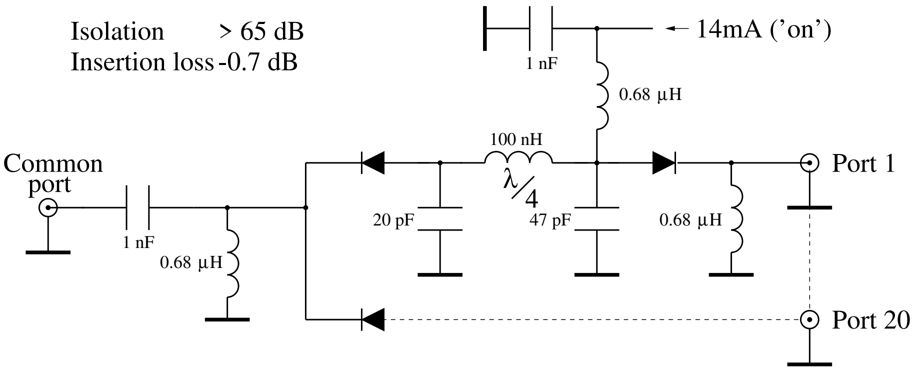

Figure 4.6: *The multiplexer. Basically the same circuit is used for the the fixed probe NMR-system (1:20) and the NMR-Trolley (1:17). A switch is closed by running a current of $7\,mA$ through each of the two PIN-diodes. The two diodes are separated by a $\lambda/4$ line to improve the isolation of an open switch. [88, 89].*

precision clock. The clock of the fixed probe NMR system is running at $20\,MHz$ and in the Trolley it is running at the reference frequency of $61.74\,MHz$. The frequency is then obtained by

$$f_{NMR} = f_{ref} + \frac{N_z}{N_c} \times f_c, \tag{56}$$

where the signal got mixed with f_{ref} to obtain the FID-signal, N_z is the number of FID-signal zero crossings and N_c is the number of clock cycles. The frequency f_c is the clock frequency; for the Trolley this is the same frequency as the reference frequency f_{ref}.

For the fixed probes it is additionally possible to digitize the signal and to do a Fourier analysis. Both methods agree within $0.01\,ppm$ [90].

The resolution of a single shot NMR-trolley-measurement of about $1.5\,ms$ length is about $0.03\,ppm$ RMS whereas the fixed probe NMR-electronics reaches $< 0.02\,ppm$ RMS. This is primarily caused by the additional noise of the nearby digital electronics, the miniaturization which causes crosstalk and the necessity of a low power

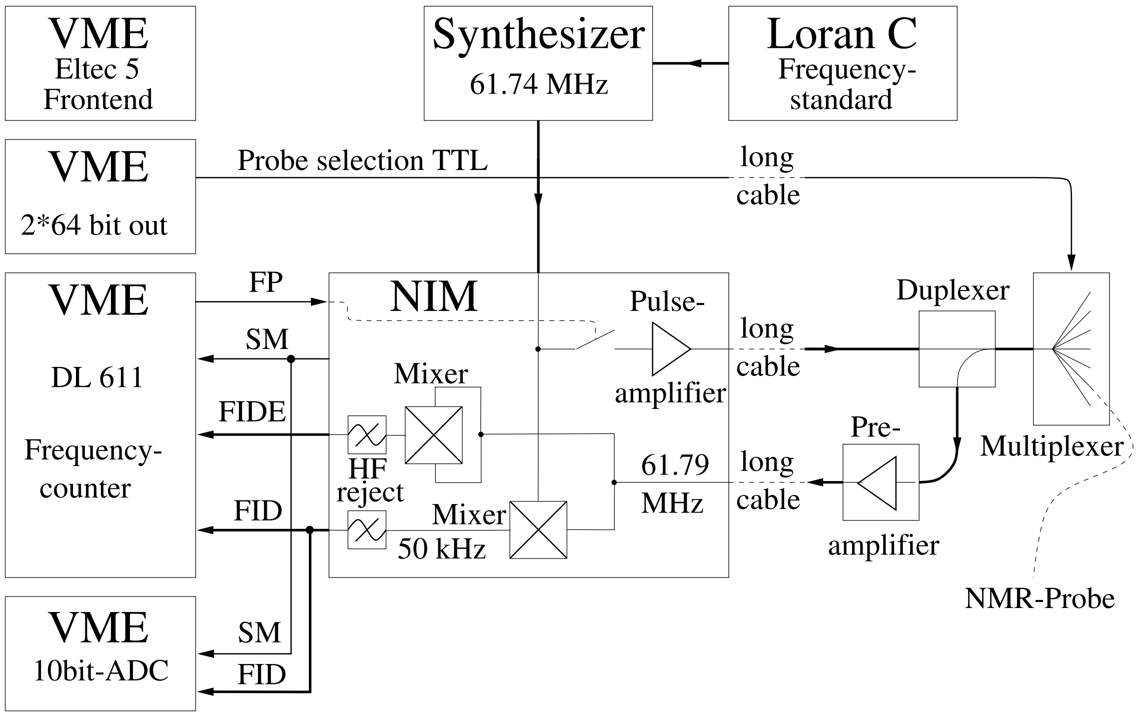

Figure 4.7: *The electronics of the NMR-magnetometer. The DL611 VME module has four independent channels. The whole VME system consists of* 5 *DL611 counter modules,* 2 64 *bit TTL output modules to select the channels (*5 *bit per multiplexer) and one multiplexed ADC (*20 *channels). There are* 20 *NIM modules and also* 20 *multiplexers for up to* 400 *probes [88, 89].*

design. The Trolley can dissipate heat only via radiation which is not very effective. Therefore the average power consumption has to be less than $1.5\,W$.

Due to the low power design the preamplifiers in the Trolley need about 200 to $250\,\mu s$ recovery time after the strong 5 W pulse which is needed to agitate the NMR-probe whereas the fixed probe electronics using special high power low noise amplifiers (UTO 101) as pre-amplifier can recover within 5 to $10\,\mu s$.

In 1997 the shimming of the magnet was not finished and therefore the Trolley NMR-signal at some locations was very short due to the field inhomogeneities. The measurement length was set to a fixed value of $\approx 250\,\mu s$ thus reducing the single shot precision to about $0.2\,ppm$. This does not show up in the final error budget since the measurements show a Gaussian distribution and each field-map consists of more than 5000 points thus reducing the uncertainty to $0.2\,ppm/\sqrt{5000}$.

It was also necessary for the Trolley system to reduce the delay time between the pulse and the measurement to $200\,\mu s$. The preamplifiers are not completely recovered after that time and the baseline of the NMR-signal does not reach the zero level after that time, it still shows an exponential decay from recharging the capacitors. This decaying signal is small compared to the NMR-signal but calculations and measurements show that it shifts the measured NMR-frequency by $\approx 0.1\,ppm$. Not

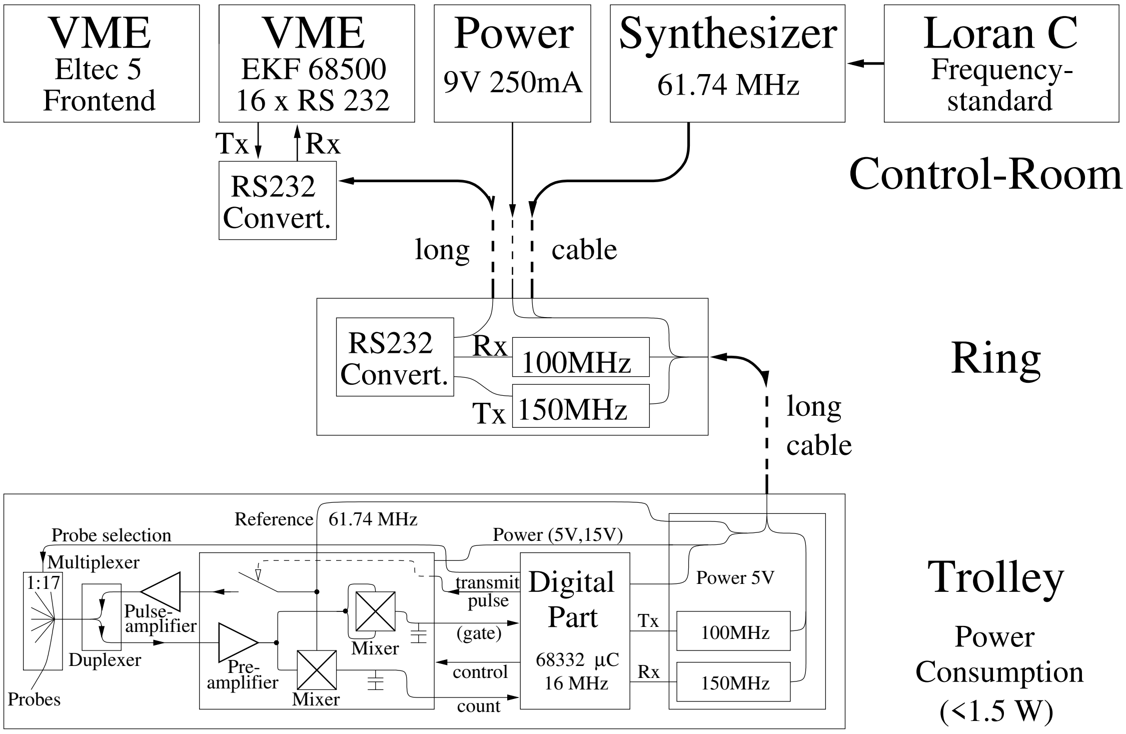

Figure 4.8: *The electronics of the NMR-Trolley.*

switching off the preamplifiers during the pulse makes the situation worse, the effect does not only come from switching on the preamplifier. However, since the same settings are used for the Trolley calibration measurements, this effect gets included in the calibration and is therefore negligible. The complete firing sequence shown in figure 4.10 and the threshold for the zero counter is programmable. This made it possible to test the NMR-Trolley under various conditions with only $0.05\,s$ between the different measurements. It is important that the threshold for the zero counter is near to zero. If there is an offset voltage, the measured frequency is shifted due to the fact that the signal is getting smaller with time and for example crosses the threshold at a phase of 20 degree at the beginning and at 40 degree at the end of the measurement.
The threshold values for the fixed probe NMR-system were determined by comparing the signal offset and the threshold value as read on a reference point. For the Trolley this is only possible as long as the electronics is not mounted inside the vacuum-tight housing. To make sure that the threshold does not drift two methods were applied:

- If the threshold is not zero the maximal signal length is shorter since after some time the signal will not be high enough to cross the threshold. Searching the threshold with the longest possible measurement length gives the optimum threshold.

- If the threshold is zero the measured frequency is independent of the length of

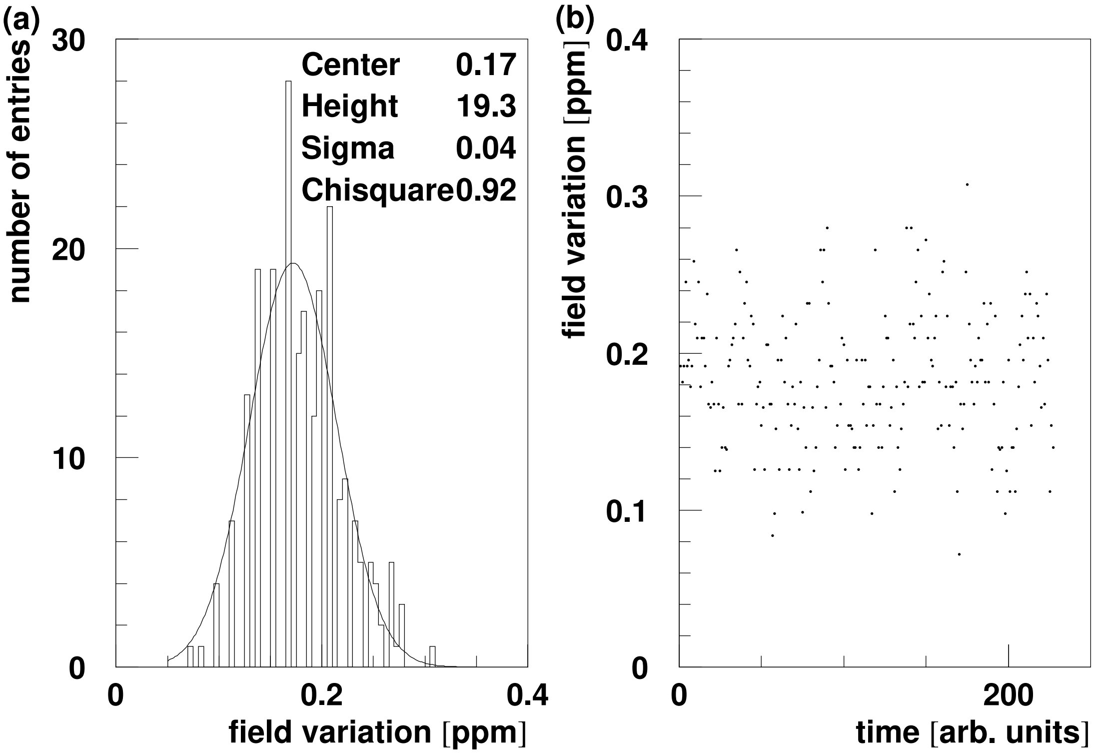

Figure 4.9: *The measurement accuracy of the NMR-Trolley. The measurement's length is only* 0.6 *ms. For longer measurements the accuracy is better. (a) This distribution is Gaussian and arises from electronic noise. (b) The same data plotted versus time.*

the measurement. By varying both threshold and duration the optimum value can be found.

Both methods gave the same result and no drift was observed.

4.2.2 Power Supplies for the Correction Coils

The third part of the magnetic field measurement and control system are the power supplies for the correction coils used to improve the homogeneity of the magnetic field. There are two types of correction coils :

- The dipole correction coils (DCCs). They are located between the iron yoke and the poles of the magnet. There are two coils every 10 degrees in azimuthal direction, one above the upper pole and one below the lower pole. They are used to make the field more homogeneous in azimuthal direction. At the nominal current of $\pm 1\,A$ they produce a local field change of $\approx 100\,ppm$ of the dipolar component of the magnetic field.

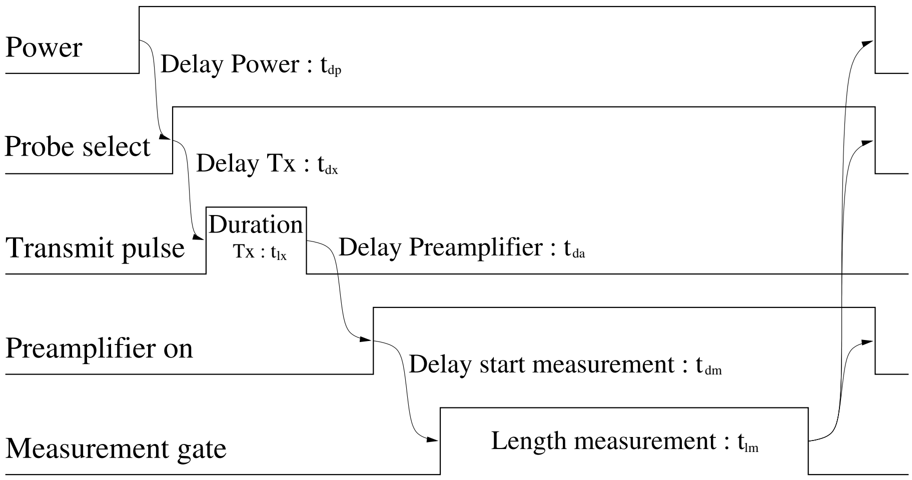

Figure 4.10: *For the field-map NMR-measurements first the analog part of the electronics is powered, after* $1.5\,ms$ *the probe is selected and after another* $1.5\,ms$ *the pulse is generated with a length of about* $10\,\mu s$*.* $40\,\mu s$ *later the preamplifier is turned on and then after* $150\,\mu s$ *the measurement with a length of* $250\,\mu s$ *starts. The symbols relevant for the firing sequence are indicated.*

- The surface correction coils (SCCs). They are one turn loops located above and below the vacuum chambers at 120 different radial locations. They are used to minimize the 360 degree averages of the higher multi-pole components as well as the skew dipole.

4 dipole correction coils are connected in series in a way that a complete 20 degree section, top and bottom, is covered by a single power supply channel, and 4 neighboring surface correction coils are connected in series which makes a sum of 78 channels.
The power supplies are built as water cooled VME-modules. The two VME-crates have a special backplane providing $\pm 20\,V$ $60\,A$ each. They are controlled by an Eltec Eurocom E5 VME computer and connected via Ethernet to the magnetic field workstation. The modules have a current stability of better than $\pm\,0.5mA$ and have read-back for current and voltage.

4.3 The NMR-Trolley

The NMR-Trolley system was designed to measure the magnetic field inside the storage region in vacuum below $10^{-7}\,mbar$ within 2 hours and without venting the vacuum chambers. To reach the proposed accuracy it is necessary to do frequent field measurements not only to provide very accurate field-maps but also to cross-check regularly the fixed probes which monitor the magnetic field during muon data taking.

The system consists of three parts, the Trolley itself, the garage mechanism to park the Trolley during muon data taking and the Trolley-drive which pulls the Trolley through the ring. The Trolley itself has the highest requirements concerning any

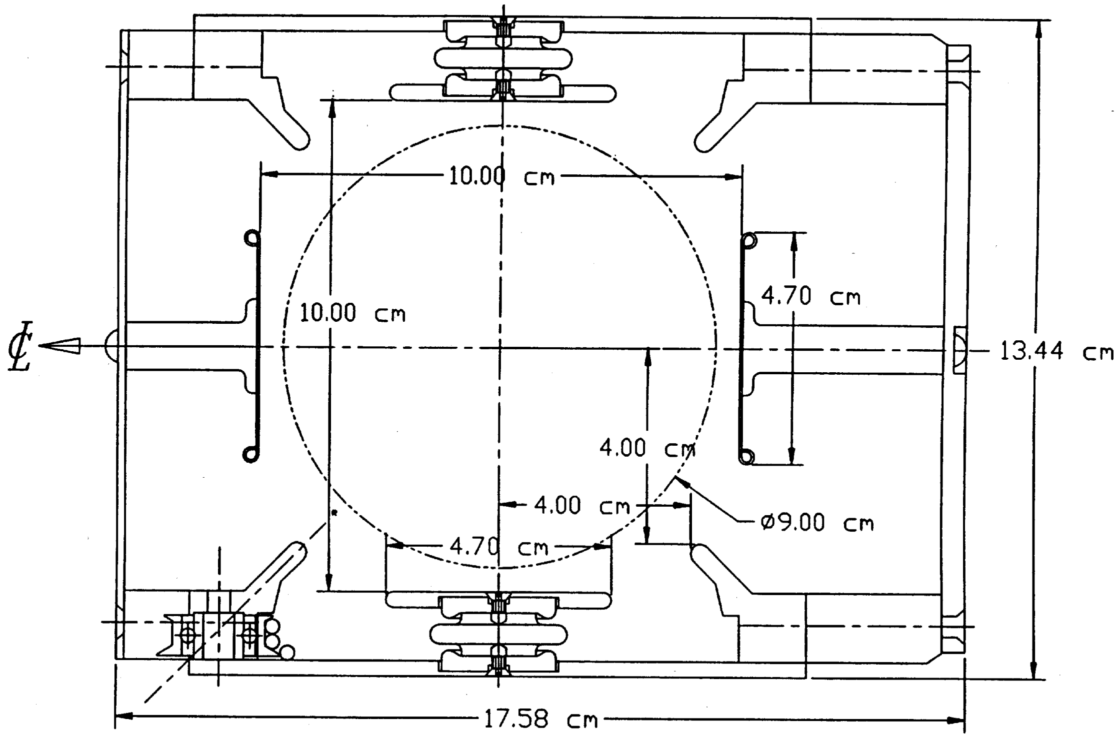

Figure 4.11: *The Trolley rides on rails inside the vacuum chamber. The rails also serve to shape the field produced by the aluminum electrostatic quadrupole plates. The vertical plates are only* 0.5 *mm thick to minimize the energy loss of the decay electrons. The dashed circle indicates the beam aperture.*

significant residual magnetism of its components since it is directly located in the magnetic field. Only certain materials like aluminum and copper and non-conductors fulfill these requirements which become higher with decreasing distance from the actual probes.

Brass for example varies between different samples of the material and generally its paramagnetism is about an order of magnitude too strong to be used in the Trolley. Therefore the vacuum-tight housing of the Trolley and the housings for the electronics are made of aluminum.

The NMR-probes in the Trolley are the same as the ones used as fixed probes on top and below the vacuum chambers. For the cable connections inside selected connectors made by Huber and Suhner are used. The Trolley is filled with air to improve the heat transfer from the electronics to the Trolley housing via air circu-

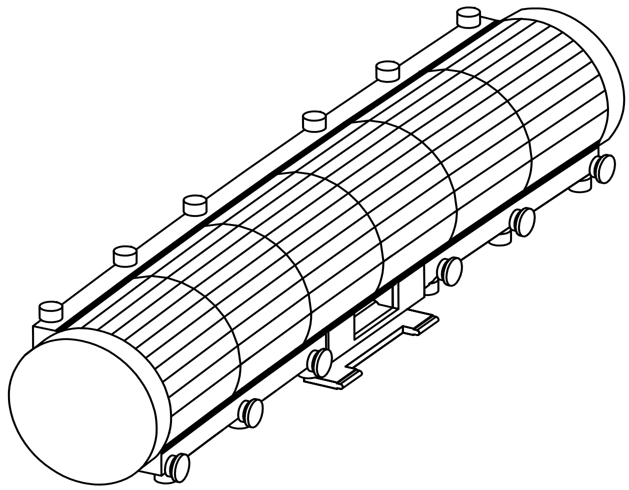

Figure 4.12: *The NMR-Trolley : Inside the vacuum-tight housing is a pulsed NMR-magnetometer. All electrical connections carrying power, reference frequency and communication were made with only two coax cables which are also used to pull the device mechanically through the storage region. An advanced version is available which only needs one coax cable. This will be necessary when the muon-kicker is in operation. The other coax cable will be replaced by a non-conducting nylon(?) line.*

lation. Most commercially available vacuum feedthroughs are magnetic which made it necessary to develop special feedthroughs to fulfill the requirements concerning vacuum-tightness and low paramagnetism. A pressure gauge inside the electronic housing allows to measure the air pressure inside with an accuracy of $\pm 4\,mbar$. The pressure remained the same within this error margin during the three month of operation under vacuum. There are two temperature gauges inside the Trolley, one inside the electronic housing and one located near to the probes. It takes about one hour to take a complete field-map. During that time the temperature inside rises approximately $1.5\,^{\circ}C$ near to the probes and $4\,^{\circ}C$ in the electronic housing.
The Trolley body is curved with the same radius as the storage ring. This was achieved by bending an aluminum pipe with a thick wall and then machining it on a CNC milling machine. The Trolley wheels are made of PEEK material and have ball bearings with balls made of glass.

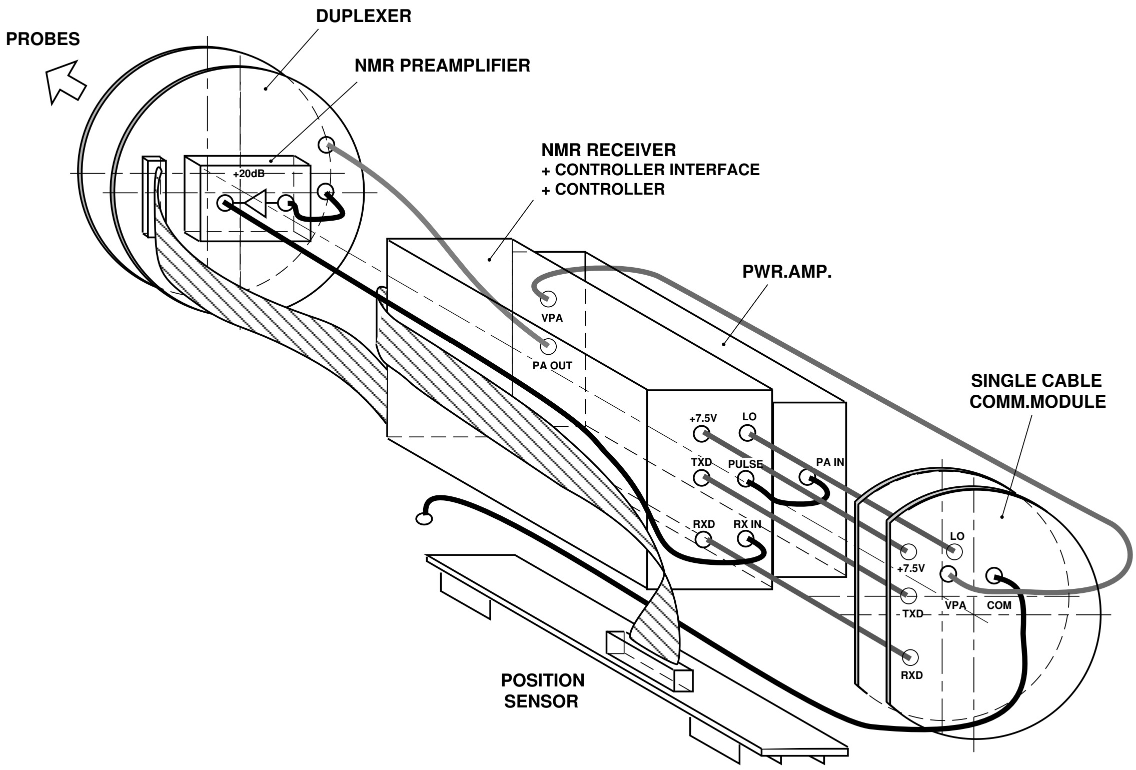

Figure 4.13: *The electronic modules inside the NMR-Trolley and their connections(1998). The NMR-probes are located at the other end of the NMR-Trolley as far as possible away from the electronics to further reduce the influence of the electronic parts on the magnetic field seen by the probes. All electronic parts have to be non-magnetic to insure that the magnetic field is not perturbed by the NMR-Trolley itself.*

The cables from the NMR-Trolley to the Trolley-drive are lying inside the vacuum-chambers, therefore non-magnetic cables with a low outgassing rate had to be chosen (Suhner 2232-08).
The Trolley drive is also made of non-magnetic parts only and is operated under vacuum. To prevent possible contamination of the $10^{-8}\,mbar$ storage vacuum, the cables run through $1\,m$ long pipes with $5\,mm$ inner diameter to separate the vacua. The pressure inside the Trolley drive is in the 10^{-7} to $10^{-6}\,mbar$ range. The two $45\,m$ cables connected to the NMR-Trolley are wound up on two aluminum drums. All electrical connections are made without using electrical rotation feedthroughs, there is a direct coaxial cable connection from the NMR-Trolley to the synthesizer which is located in the control room and provides the reference frequency of $61.74 MHz$ with 10^{-10} accuracy. The motors used to drive the drums are of piezoelectric type and do not need magnetic fields for operation. Instead they use a traveling mechanical

wave on a piezo ring to turn a coaxial disk by friction. The cable tension on both cables is controlled by strain gauges to limit the tension on the cable and keep it stable.
The Trolley garage is located about 120 degrees away from the Trolley drive. It is also driven by a piezoelectric motor and moves a complete 50 cm section of the rails radially in and out. The Trolley drive has a special mode for garage operation. In that mode it just keeps the tension on both cables constant. Moving the rail frame away from the storage volume makes a difference in the magnetic field seen by the Trolley compared to the one seen by the stored muons. However this effect was measured and is less than 0.5 ppm locally. This makes an effect of about 5ppb on the average magnetic field seen by the muons and can be neglected.

4.4 The Calibration of the Trolley NMR-System

The Trolley itself has an effect on the B-field it is measuring. Even though it was built of non-ferromagnetic parts exclusively, it disturbs the B-field. For example the paramagnetism of the vacuum-tight aluminum vessel has a measurable effect on the B-field seen by the NMR-probes at the 2 ppm level. The specifications established in the design report [91] demand that those effects are less than 15 ppm to make sure that the calibration is still reliable. The reason why those effects have to be small is that the calibration gets more and more dependent on the relative angle between the Trolley and the B-field when the deviations are big.
Measurements with NMR-probes without the Trolley housing were done by Prigl [89] and the deviation was less than 0.1 ppm for measurements with different angles in a range of ± 8 degrees between the probe and the magnetic field. The effects of the trolley housing should be comparable. The bigger amount of material is compensated by the bigger distance to the active probe volume. The angle between the Trolley and the magnetic field is constant within ± 1 degrees during a field measurement and during the calibration. The effects of the Trolley on the magnetic field can also be seen by the fixed NMR-probes which are mounted on top and below the vacuum-chambers of the storage ring. The calibration of the Trolley was done inside the $g_\mu - 2$ magnet at an azimuthal position with a vacuum port and where the magnetic field was as homogeneous as possible. Since the shimming was not finished there was still a gradient of about 0.2 ppm/mm in azimuthal direction.
A standard probe, described in [90] was brought to the central position in the x-y plane of the storage region and the magnetic field was measured. The spherical water sample is located in the middle of this probe to reduce the influence of the end-caps of the surrounding cylindrical aluminum housing. This has the disadvantage that it is impossible to reach all x-y positions of the probes inside the Trolley because the probe hits the wall of the vacuum-chamber. Therefore a probe of different shape had to be calibrated against the standard probe. This probe will be referred to as plunging probe.
A problem arose from the drift of the magnetic field during this measurement. To

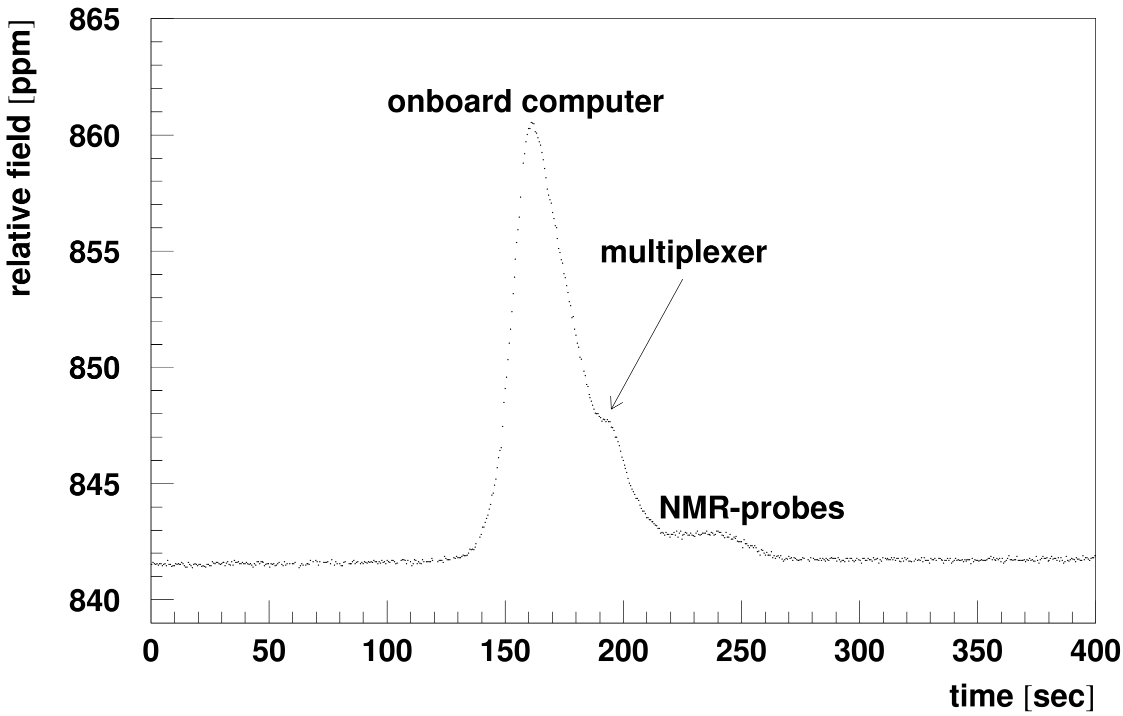

Figure 4.14: *The NMR-Trolley itself has an effect on the magnetic field. The magnetic field seen by a fixed probe when the Trolley passes. The effect is small ($< 2\,ppm$) at the position of the probes and can be corrected for in a calibration procedure.*

keep track of the field-change another probe in the same magnet but about $1\,m$ in azimuthal direction away from the calibration position was used to monitor field-changes. The distance of about $1\,m$ was necessary to insure that the movement of the calibration probe, the plunging probe and the NMR-Trolley did not affect the magnetic field seen by this probe. On a timescale of minutes the accuracy of this method to track the magnetic field with a nearby probe inside the $g_\mu - 2$ magnet was proven to be better than $0.05\,ppm$.

The calibration of the plunging probe was done by exchanging the two probes in a way that the active volume of both probes was at the same position thus measuring the same magnetic field.

This procedure was repeated three times by different persons and a difference of $+0.46\,ppm$ was obtained. The positioning was good to $1\,mm$ and the biggest field gradient was $0.2\,ppm/mm$ yielding an uncertainty of $\pm 0.2\,ppm$. The standard probe itself was found in [90] to deviate $-0.044\,ppm$ from a pure water sample without surrounding material. This adds up to an overall correction of $+0.4 \pm 0.2\,ppm$ for the plunging probe compared with a pure water sample.

The Trolley was driven to the same location and the magnetic field was measured with each of the 17 probes inside the Trolley. Then it was removed and the same positions were measured with the plunging probe. This procedure was repeated twice by different persons. The results for the different probes are shown in figure 4.15.

To obtain this result two additional corrections were necessary :

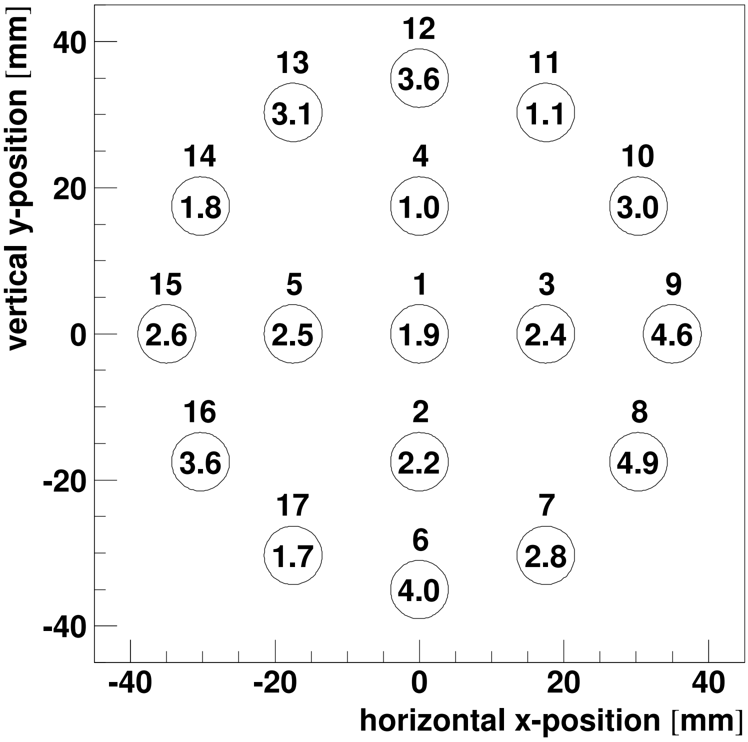

Figure 4.15: *The arrangement of the probes in the Trolley. The numbers in the circles are the calibration offsets for the NMR-probes in the Trolley in ppm. These values have to be subtracted from the NMR-frequency measured with the Trolley to obtain the NMR-frequency of a cylindrical water sample without offsets produced by surrounding material. The numbers on top of the circles are the probe numbers used internally by the Trolley. In azimuthal direction the probes are located near to one end of the Trolley as far as possible away from the electronics and the position readout.*

The plunging probe could not reach the uppermost position, instead of measuring at $(0\,mm, 35\,mm)$ the position $(0\,mm, 34\,mm)$ was measured and the field-gradient of $0.3\,ppm/mm$ in y-direction obtained by the measurements at $(0\,mm, 0\,mm)$, $(0\,mm, 17.5\,mm)$ and $(0\,mm, 34\,mm)$ was used to add $0.3\,ppm$ to this value.
Measuring the positions of the probes inside the Trolley gave a deviation of $2mm$ in azimuthal direction. During the calibration the gradient in azimuthal direction was determined to be $0.2\,ppm/mm$ which adds another correction of $0.4\,ppm$ for each probe.
The positioning inaccuracy during this measurement was about $\pm 2\,mm$ in azimuthal direction and about $1\,mm$ in the x-y plane. Added together with the inaccuracy of the calibration of the plunging probe this gives an overall inaccuracy of $0.5\,ppm$ for the calibration of each probe inside the trolley.
Temperature effects can be neglected on this scale, they are only $0.01\,ppm/°C$ [92].
$1.5\,ppm$ of the calibration offsets are due to the cylindrical shape of the active vol-

ume, the rest comes from paramagnetism of the material surrounding the probe. At positions where the differences between neighboring probes are bigger than usual (for example probe 9, 10, 11 and 12) there is additional aluminum to hold the Trolley wheels, the offsets can be explained by the shape of the aluminum housing of the Trolley.
To obtain the Larmor frequency of free protons, a correction of $+25.79(14)\,ppm$ has to be applied to these values. This is due to the internal diamagnetic shielding. For an atom or a molecule the diamagnetic shielding arises from the Larmor precession of the electrons induced by the applied magnetic field B. The shielding constant of atomic hydrogen has been calculated by Lamb [93] and Grotch [94]

$$\sigma(H) = 17.733 \times 10^{-6}. \tag{57}$$

It is not possible to calculate this value accurately for water molecules but it has been determined by an experiment performed by Phillips, Cooke and Kleppner [95, 96] which compared the NMR frequency of a spherical pure water sample with the oscillation frequency of a hydrogen maser in the same magnetic field. Including the shielding given in equation (57) they obtained

$$\sigma(H_2O, 34.7°C) = 25.790(14) \times 10^{-6}. \tag{58}$$

4.5 The Magnet

The storage ring magnet has a super-ferric design, a combination of superconducting coils with an iron yoke. The C-shaped flux return yoke makes up the great bulk of the magnet weight. For the yoke iron of conventional quality (0.06% carbon content) was used whereas the poles are made of very pure continuous vacuum cast iron with a typical carbon content of only 0.0003% [97]. The higher purity increases the permeability and more important reduces the number of inclusions and air bubbles in the iron significantly. The total weight of the magnet is about 750 metric tons and the nominal field is $1.45\,T$ at a current of $5178\,A$.
There are 4 superconducting coils. 2 coils have a smaller radius and are located above and below the horizontal plane, both with 24 windings. The outer coils form a double coil held together by a strong aluminum support. Both parts consist of 24 windings. All coils are connected in series. The superconductor has a critical current of $10000\,A$ at $2\,T$ and $4.5\,K$. It is operated very conservatively far from its critical region. The outer coil is the largest diameter superconducting coil in existence, the inner ones share the second place.

4.5.1 The Shimming of the Dipole Component of the Magnetic Field

In addition to the careful design the magnet has several features which can be used to improve the field homogeneity.

1. Iron can be added to the plates on top of the yoke, to the backleg or below the yoke. The effect of adding iron at those locations has been measured and can be used to reduce wide range inhomogeneities of the magnetic field. Instead of removing iron it is also possible to put aluminum spacers between the yoke and the top or bottom plates. Adding iron causes the magnetic field to be stronger at that location. The effect has a typical half-width of 25 degrees in azimuthal direction. This method has been applied to reduce the effect of the hole through the backleg for the beam and at two other locations. The iron pieces were added to the backleg to cause an effect which is symmetric in vertical direction. To some extend the method can also be used to reduce the magnetic field gradient in vertical direction, for example by putting spacers between the bottom plate and the yoke and adding iron on top.

2. There is an air-gap between the poles and the yoke which is filled with iron wedges. Moving those wedges in the radial direction reduces or increases the air-gap at that position. There are 24 wedges for each 10 degree section making a total number of 864 wedges, 12 above each upper pole and 12 below each lower pole. The effect of moving all 24 wedges of one pole-section from one extreme position to another is about $300\,ppm$. Moving one wedge produces an effect with a typical half-width of 10 degrees. The effect of moving many wedges can be added linearly and the effect on the higher multi-pole components of the magnetic field is small. If bigger changes are needed it is possible to add iron to the wedges.

3. The shimming in 1997 showed the necessity of a tool to shim the dipole component of the magnetic field very locally at the edges of the poles. This can not be done by moving the wedges as described above because they act through the poles and therefore any change is spread out in the azimuthal direction. To cover this problem another method is applied. Thin sheets of shim iron ($25\,\mu m$ to $100\,\mu m$) are cut to stripes and put between aluminum plates to provide the necessary mechanical strength. They are inserted directly on top or below the vacuum chambers. The location of the stripes and their thickness and width is calculated using the measured field-maps. In 1997 tests have been done to evaluate the size of the effect of these plates and during spring 1998 they will be installed at all locations. Tests at selected locations have shown that a reduction of the effect by at least a factor of 5 is possible.

4. Additionally to these passive components there are 72 dipole correction coils, one for each pole. They can be used to reduce the effects of different temperature changes at different azimuthal locations shown in figure 4.19. At their nominal current of $\pm 1\,A$ the upper and the lower coil together produce a field-change of $\pm 200\,ppm$. This is enough to cover temperature effects. It has been shown that they could be used to stabilize the magnetic field within $0.05\,ppm$ using active feedback from the fixed NMR-probes. It is however planned to use active feedback to control the main power-supply current, therefore feedback for the dipole correction coils will not be used.

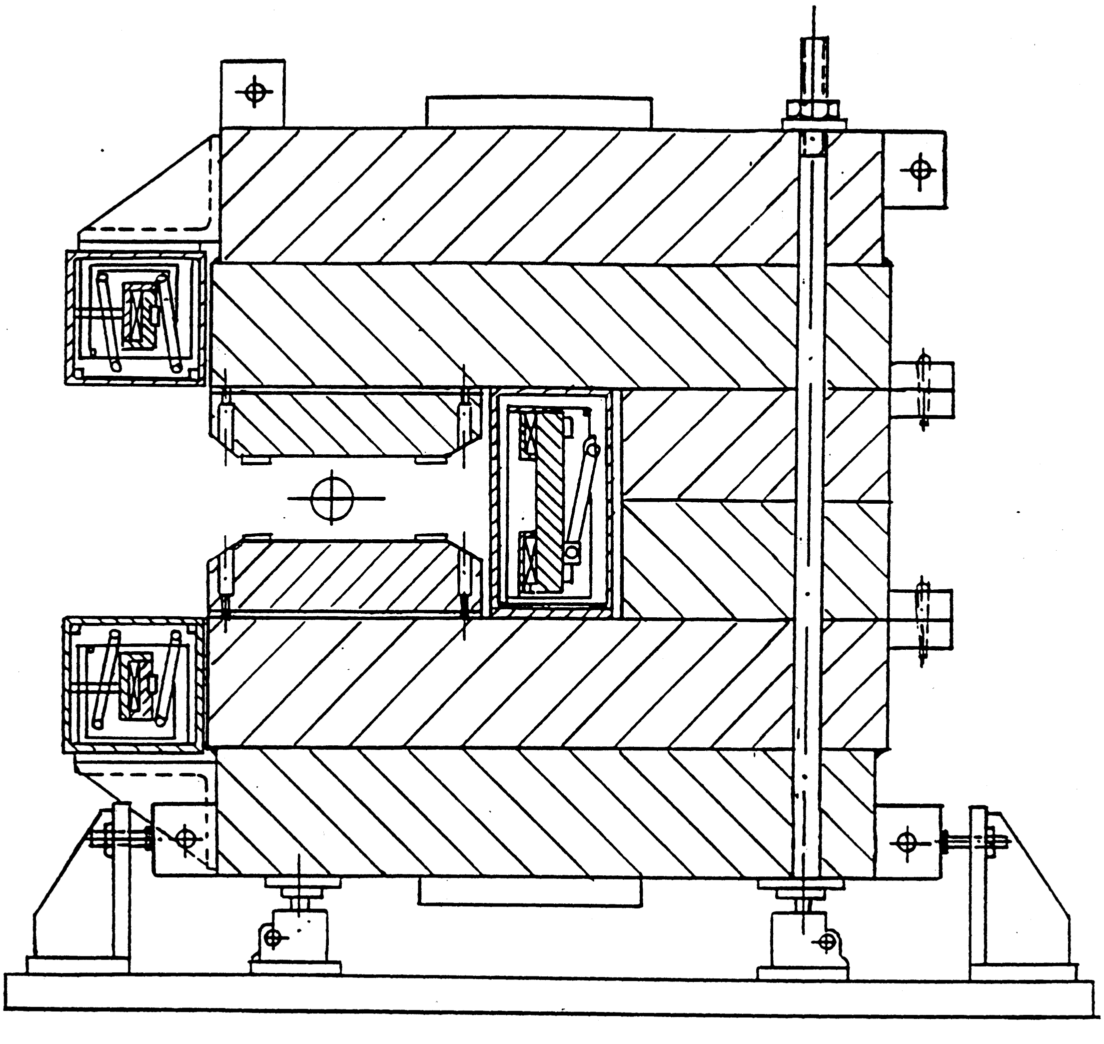

Figure 4.16: *The yoke of the $g_\mu - 2$ magnet. The magnet has a super-ferric design which consists of 4 superconducting coils around the ring with a C-shaped iron yoke open towards the center of the ring. The 4 coils are embedded in 3 ring cryostats where the 2 outermost coils share one of them. The poles are high quality extremely low carbon* ($< 0.005\%$) *content iron whereas the yoke is usual low-carbon* ($< 0.05\%$) *steel.*

4.5.2 Reducing the Higher Multi-Pole Components of the Magnetic Field

The magnet has a powerful feature to reduce the multi-pole coefficients up to octupoles. The higher multi-pole coefficients are already near to zero by design.
On top of the poles at the edges in radial direction there are shim iron pieces (Rose/Danby shims). They are 5 cm wide and originally had a thickness of 3.8 mm and 4.5 mm at the outer and inner radius, respectively. The thickness of these irons

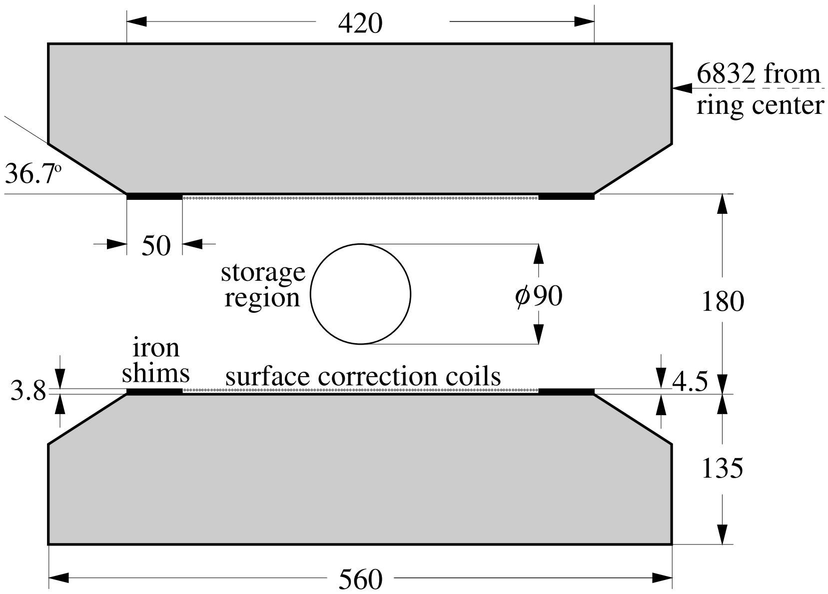

Figure 4.17: *The cross-section of the poles. All dimensions are in millimeters. The original dimensions of the shims are shown, but they have been machined in the shimming process to minimize the higher multi-pole components of the magnetic field. The circle in the center is the cross-section of the storage region. The surface correction coils cover* 360 *degrees in azimuthal direction. There are 120 current loops each on the upper pole and the lower pole.*

can be reduced by machining them on a milling machine. This can be done in a way that the multi-poles coefficients are minimized. It is possible to reduce up to 4 multi-poles to zero since there are 4 free parameters, the thicknesses of the 4 shim irons. To determine the size of the field change due to the shim irons the magnetic field was measured without the shims and then compared with regular measurements. This was also done with only some of the shims removed.
A multi-pole analysis (for details see chap. 5) was carried out and the optimum thicknesses were obtained. Since it was not clear that the effect is linear on such a big scale it was decided to reduce the thickness of the shims only by 90% of the calculated values. After remounting the shim irons measurements showed that the field change is in fact linear.
During spring 1998 a second iteration of this process was performed further improving the field homogeneity. The iron shims were primarily used to minimize the

360 degree averages of the multi-pole coefficients at $r = 4.5\,cm$				
Multi-pole	before shimming	after shimming	during data taking 10.07.97 6:45	during data taking 11.07.97 14:45
normal quadrupole	$100\,ppm$	$7\,ppm$	$6.5\,ppm$	$4.6\,ppm$
skew quadrupole	$40\,ppm$	$10\,ppm$	$11.4\,ppm$	$11.6\,ppm$
normal sextupole	$135\,ppm$	$3.5\,ppm$	$1.7\,ppm$	$1.6\,ppm$
normal octupole	$40\,ppm$	$-1.3\,ppm$	$-2.4\,ppm$	$-2.4\,ppm$
normal decapole	$20\,ppm$	$2\,ppm$	$0.2\,ppm$	$0.2\,ppm$

Table 4.1: *The improvements due to the shimming in 1996. The changes between the last field-map during shimming and the ones taken during the run are due to the installation of the detectors and the vacuum-chambers as well as due to the different room temperature. The changes between 10.07.97 and 11.07.97 reflect the change in the room temperature. The change of the normal quadrupole component agrees with the values obtained using the fixed NMR-probes in figure 5.5. By July 1998 the second iteration of the shimming process is expected to be finished. The field homogeneity will be improved significantly [98].*

skew quadrupole component and the normal and skew sextupole components of the magnetic field.
The normal quadrupole component can be minimized using the surface correction coils (SSCs). A program is available [99] to minimize the average multi-pole components of the magnetic field. This program also tries to keep the sum of all currents in the surface coils minimal.

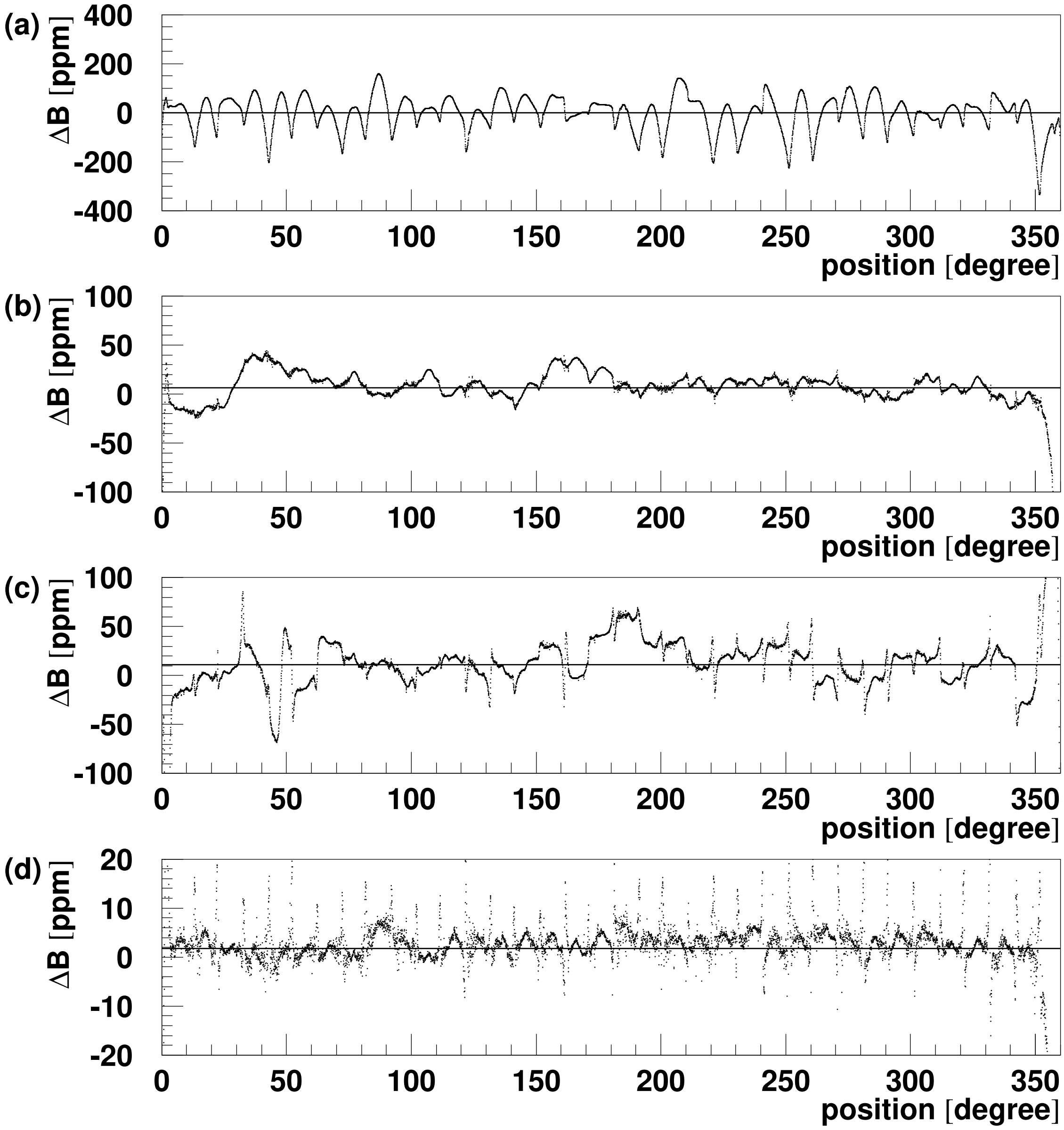

Figure 4.18: *The variation of the magnetic field in azimuthal direction (10.07.97 ≈ 6:45 am). The magnetic field is expanded into multi-pole components. (a) The dipole component, (b) the quadrupole gradient in the horizontal plane (normal quadrupole), (c) the quadrupole gradient in the vertical plane (skew quadrupole) and (d) the normal sextupole. The values for the higher multi-poles are given at a distance of* 4.5 *cm to the center which is the outer diameter of the storage region. All higher multi-poles are of comparable size to the sextupole (other sextu-and-octupoles) or much smaller (decapoles, higher multi-poles). For the 1998 run shimming the magnet will improve the field homogeneity.*

4.5.3 Stability of the Magnetic Field

The absolute stability of the magnetic field is only necessary at the 100 *ppm* level to insure that the momentum of the stored muons still complies with eq. (43) (magic gamma) as long as the fixed NMR-probe measurements can track the changes in the strength of the magnetic field.
If however the multi-pole coefficients change or the field changes within a small re-

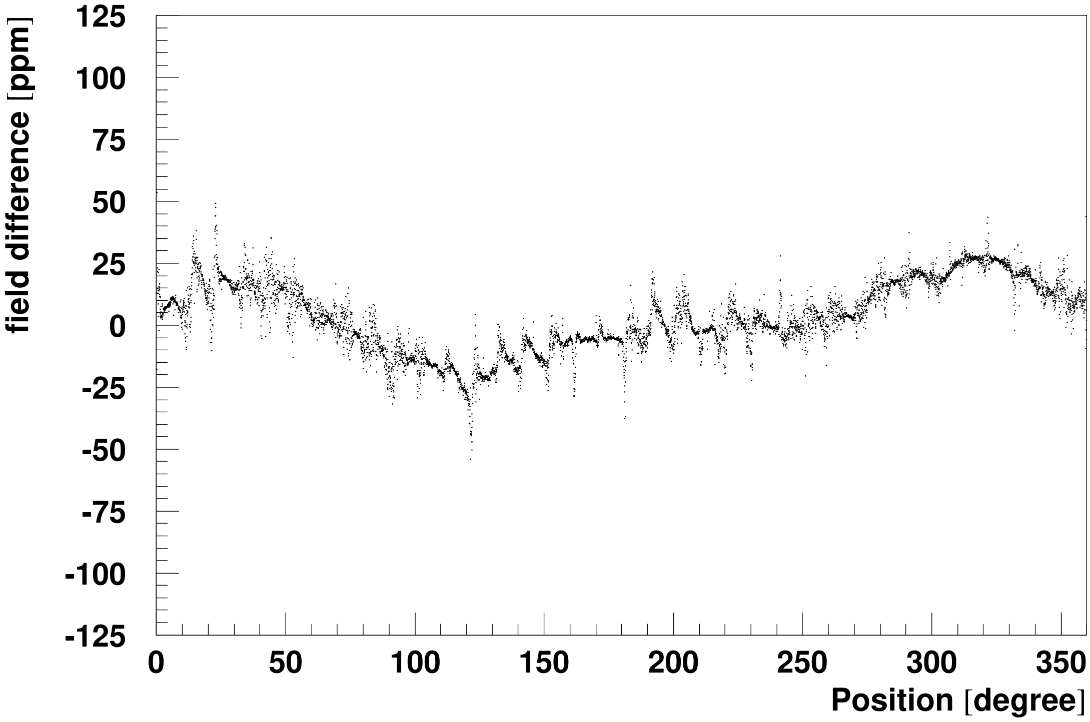

Figure 4.19: *Here the difference between two field-maps is plotted (26.06.97 and 29.06.97). The underlying sinusoidal structure is due to the different temperature changes at different locations around the ring. The 36 bumps are at the points where 2 poles touch each other. There the field gradients in azimuthal direction are high and due to the limited accuracy of the position readout of the NMR-Trolley these bumps appear.*

gion azimuthally, the changes can not be detected sufficiently using the fixed probes. There are three types of effects changing the homogeneity of the magnetic field:
Temperature changes cause a change in the distance between the poles, and if they come together with a temperature gradient in the magnet backleg they also change the angle between the poles. They also change the relative positions of the poles to each other in a way that the magnetic field near to the pole edges in azimuthal direction can have bigger variations compared to the field at the center of the poles. Temperature effects comparing field-maps taken at different days can be seen in figure 4.19 and the change of the normal quadrupole component tracked with the fixed NMR-probes can be seen in figure 5.5.

Second there are magnetic field changes due to changes in the environment. For example when the beam-line is turned off this changes the average magnetic field in the magnet by $\approx 6\,ppm$. This is reproducable and the field goes back to its original value when the beam-line is turned on again. Moving ferromagnetic equipment within the experimental hall inside the ring area also causes changes in the magnetic field and is restricted to emergencies.
It takes about 45 minutes to ramp the magnet to full field. During ramping eddy currents are induced in the yoke and the poles. The 36 poles are electrically isolated from each other with Kapton foils. The eddy currents stop at the boundaries of the poles. Since the eddy currents change the magnetization of the pole pieces, there are differences between the pole ends and the center. This effect is described by Halbach [100] and called 'Umbrella' effect. If the magnet is always powered and ramped down using the same procedure, those effects are always the same and can be compensated by shimming. The magnet was once ramped down very fast during a test for the quench control system. When it was powered again the homogeneity of the magnetic field had changed. This effect can be seen in figure 4.20. After another power up and down cycle the field was the same as before the quench.

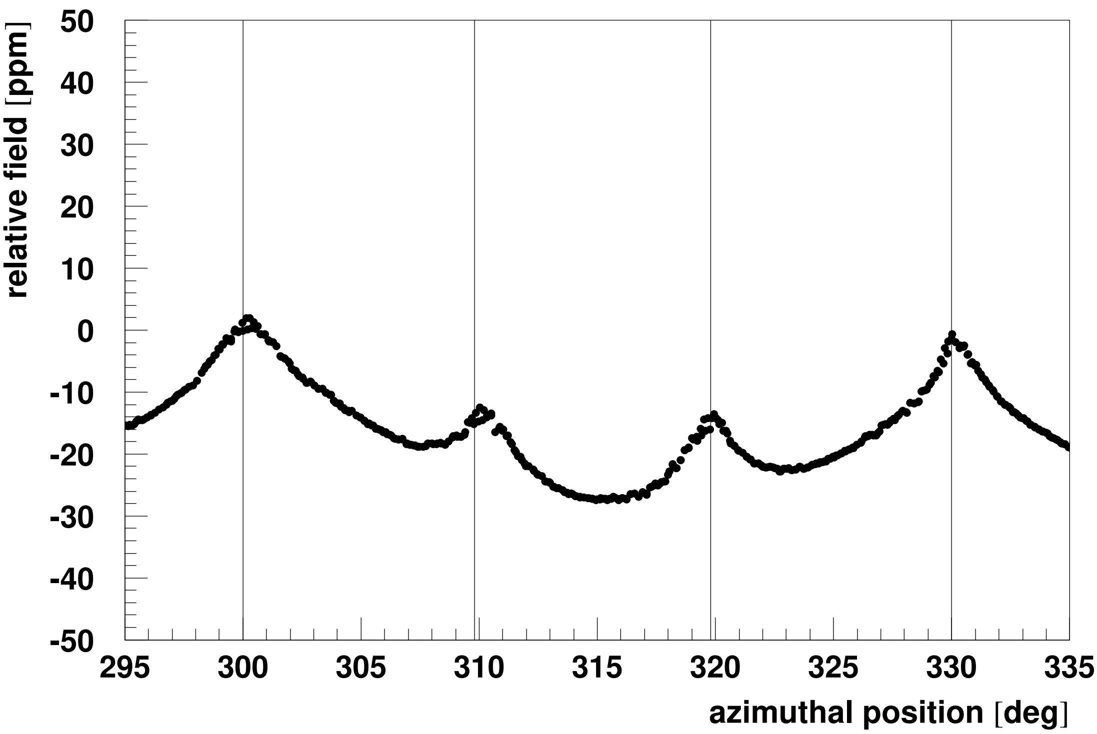

Figure 4.20: *Difference between a field-map taken after a magnet quench and a field-map taken before a magnet quench. During a quench the magnet is ramped down with a time constant of* $34\,s$ *[101]. The 'umbrella'-effect is due to eddy currents in the iron poles due to fast changes in the magnetic field and causes the magnetic field at the edges of the poles to be stronger. After cycling the magnet the effect disappears.*

4.6 The Inflector

In order to inject the beam into the storage ring magnet, it is necessary to bring the particles on a straight line as close as possible to the storage region. In the ideal case the particles would be injected tangentially. This is impossible because the charged particles of course interact with the magnetic field in the magnet before entering the storage volume. To bring the particles as near to the storage region as possible an inflector magnet was built to screen the magnetic field of the main magnet. This is a difficult task because inside the inflector the main magnet field of about $1.45\,T$ should be cancelled completely but in the storage region, just outside the inflector, the field should be distorted as little as possible. The region where the

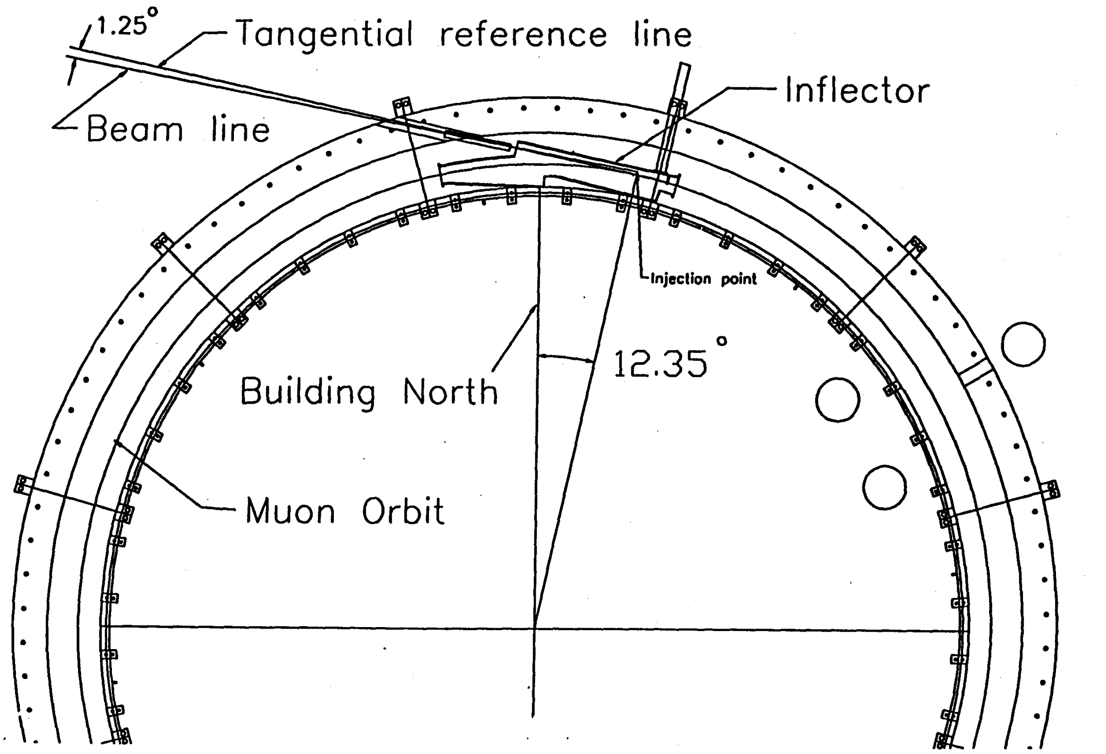

Figure 4.21: *Injection is done using a static superconducting inflector. The injected particles would leave the storage region after less than one turn, but the injection angle is very small. Therefore there are two possible injection schemes: (a) Pion injection: Higher momentum* (+0.5%) *pions are injected, some of the decay muons get stored. (Low efficiency* $\approx 10^{-4}$*)(1997). (b) Muon injection: The muons pass through a pulsed kicker (1998).*

field goes from about zero to full field has to be very small otherwise the injection angle is too big. The inflector magnet [102, 103] was build at KEK in Japan and is a superconducting magnet with a superconducting shield which screens the storage region from the inflector fringe field. The inflector which was used in the 1997 run

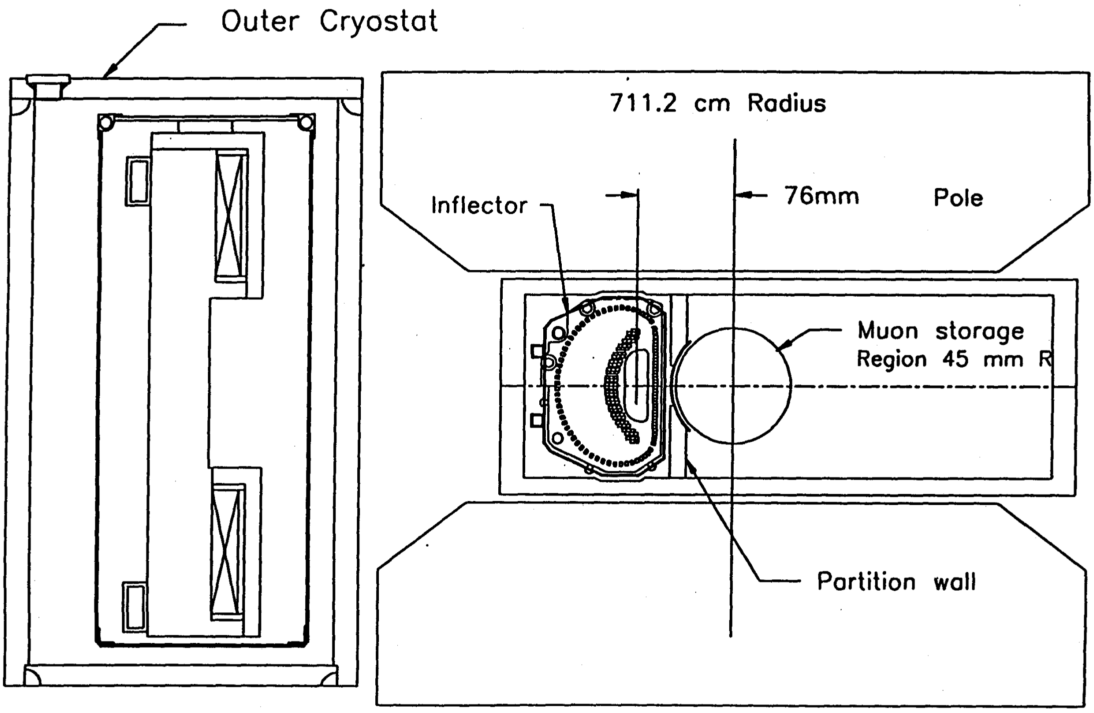

Figure 4.22: *The inflector consists of a superconducting magnet which eliminates the magnetic field of the main magnet inside the beam-line and a superconducting shield between the inflector and the storage region. The particle beam goes through this superconducting shield.*

had a problem: During the manufacturing the superconducting shield had to be cut to repair one of the superconducting interconnects between the two superconducting coils which make up the inflector magnet. This cut caused the inflector field to penetrate the superconducting shield more than expected. A new inflector is built at KEK now and it should be operational before 1999.
The magnetic field inside the storage region near to the inflector shows higher variations both azimuthally and over the storage cross-section. The length of the NMR-FID signal is limited in such an inhomogeneous magnetic field to a very small number of zero-crossings and also the shape of the signal is perturbed (figure 4.23 compared to figure 4.3). With the normal setup in the NMR-Trolley it was impossible to measure the magnetic field at some locations very near to the inflector exit. It is easy to make a rough estimate for the approximate length of the NMR-signal:

$$t_s \approx \frac{1}{d \cdot \frac{dB}{dx}} \cdot \frac{B}{2f_l} \tag{59}$$

where d is the probe size, dB/dx is the magnetic field inhomogeneity and f_L is the Larmor frequency of the protons. Since the length of the probe is $1.5\,cm$ and the field inhomogeneities near to the inflector exit are of the order of $100\,ppm/cm$ in azimuthal direction the signal length is roughly $0.05\,ms$. For mapping the magnetic

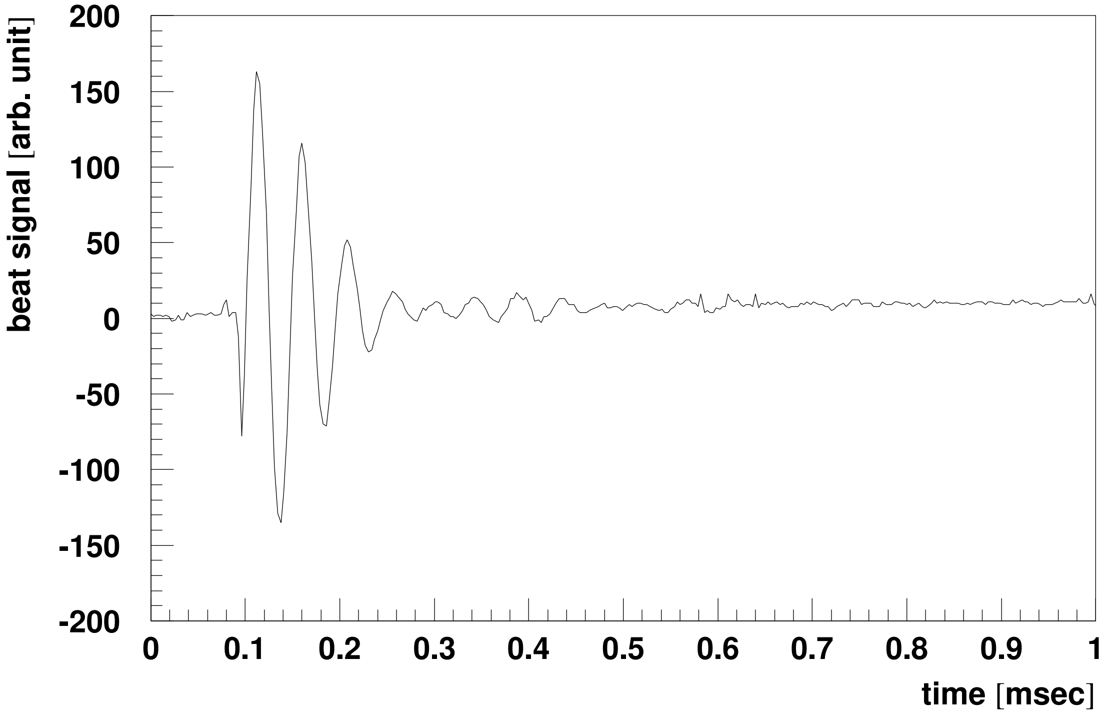

Figure 4.23: *In an inhomogeneous magnetic field the length of NMR-FID signals is very short. The nuclei in the water sample get out of phase very fast. When the nuclei are out of phase the (measured) sum signal cancels out. It can also happen that most nuclei are out of phase after some time and some of them come back into phase and the NMR-signal increases again after some time [84].*

field inside the inflector a special set of NMR-probes with shorter length of the active volume was made. This made it possible to measure the magnetic field at most locations.

To determine the average magnetic field the muons saw during the time they got stored in the ring this additional data was taken and replaced the missing $\approx 10\,cm$ in the original field-maps. Since this data was just taken once at the end of the run and the magnetic field varied about $150\,ppm$ during the data taking period 1997 the absolute magnetic field value was fitted using the overlap between the different field-maps.

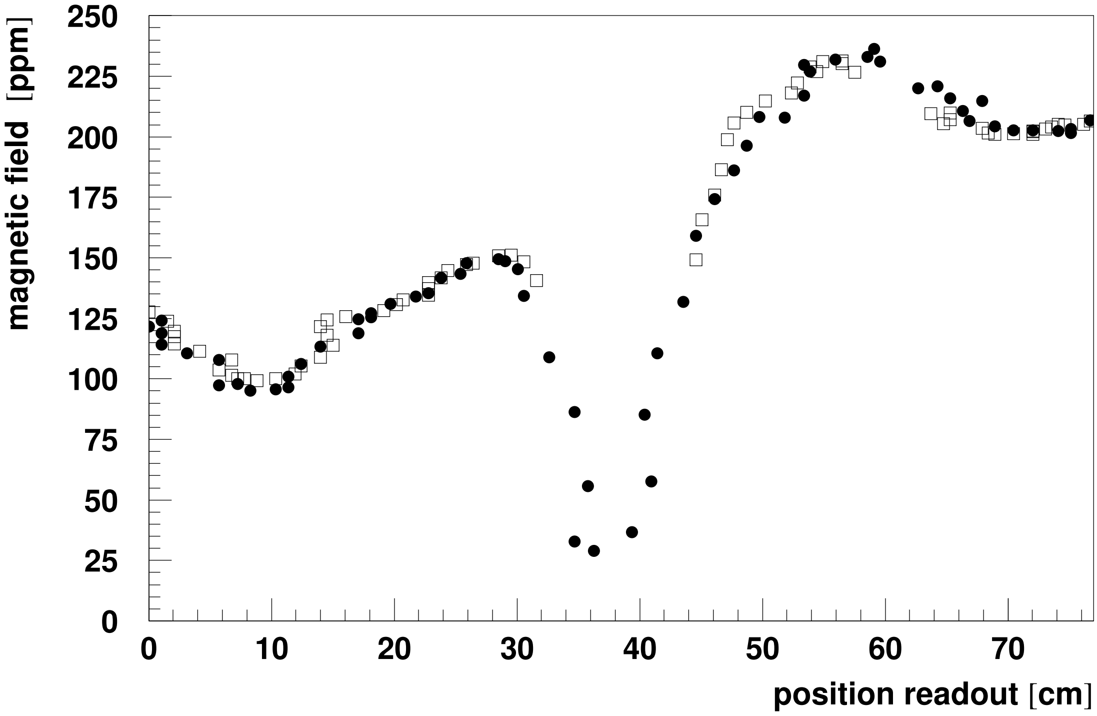

Figure 4.24: *The squares are the magnetic field values taken from a regular field-map (10.07.98 6:30am). The dots are the additional points from a dedicated inflector field measurement (12.07.98 22:10). All data points are taken with the central probe* (1). *Since the average magnetic field drifted about* 8 *ppm during that time the dots are shifted by* 8*ppm to match the squares. This is done by a fit which minimizes the differences between the two measurements in the regions where the two data sets overlap. The irregular shape of the curve is due to the limited resolution of the (backup) position readout of the Trolley.*

5 Magnetic Field Measurement

In 1997 when the experiment was commissioned it was not only necessary to calculate the average magnetic field $< B >$ for any given time but also to perform many systematic studies to understand the behaviour of the main magnet and the magnetic field measurement system under various conditions. Additionally the NMR-Trolley which measures the absolute B-value had to be calibrated against the NMR-frequency of free protons. There are 4 steps necessary to calculate the average magnetic field $< B >$ that the particles see:

1. The NMR-Trolley has to be calibrated to measure the absolute magnetic field value. It is desirable to use the NMR-frequency of unperturbed free protons as unit for the magnetic field because the magnetic moment of protons is known very precisely. The comparison between this frequency and the measured modulation frequency of the muon decays give the ratio between the magnetic moment of the proton and the anomalous magnetic moment of the muon.

2. The B-field has to be measured in detailed field-maps using the NMR-trolley. At least every time the magnet is powered and before it is turned off again a field-map has to be taken.

3. The B-field has to be tracked with the fixed probes during the time when the beam is on.

4. The average B-field the particles see has to be calculated using information about the position of the muon beam inside the storage volume. This information can be provided using 3 independent devices: There are scintillating fiber harps which can be flipped into the muon beam to measure directly the position distribution of the beam. The disadvantage of this method is the destructive influence of the fiber counters on the beam. There are also two non-destructive devices: The pickup-electrodes which pick up the induced charges which are produced by the muon beam, and the trace-back chamber. The trace-back chamber is used to detect decay electrons (positrons) and to reconstruct the point where the muons decayed inside the storage volume. With this information and sufficient statistics it is possible to reconstruct the muon beam distribution. To measure the position where the muon decayed it is necessary to both measure the momentum and the direction of the decay electrons (positrons) with a very high resolution.

The time dependent $< B(t) >$ then has to be combined with the measured $\omega_a(t)$ to obtain the final $g_\mu - 2$ value. For the startup run 1997 field-maps were taken every 24 to 72 hours. Every field-map consists of ≈ 6000 readings for each of the 17 probes. The muon storage ring has a circumference of $\approx 45\ m$ and thus the average distance between two measured positions is $7 - 9\ mm$. The active volume inside

the NMR-probes is a cylinder of 2.5 mm diameter and 15 mm length. The probe signal is the sum signal of the nuclei within the active volume. This means that two successive measurements already overlap.
The measurements are done with the NMR-Trolley in motion. Possible effects due to eddy currents induced in the aluminum housing of the Trolley are proportional to the velocity of the Trolley times the magnetic field gradients. Since the field is very homogenous and the velocity is very low they can be neglected. This has also been verified by a comparison between a regular field-map and a 'stop and go' measurement.
The azimuthal position of the NMR-Trolley in the storage ring can be determined with 2 independent readout devices and also using the magnetic field data:

1. Below the Trolley rails is a barcode. The NMR-Trolley has two sensors to read this barcode. Two sensors at different positions are necessary because the barcode is discontinued at some locations. The contrast of the barcode on the aluminum structure is low and there were many misreadings. For the 1998 run it is planned to improve the barcode in the inflector region.

2. The Trolley-drive has a readout for the drum position. Since the cables from the drive to the NMR-Trolley are 45 m long and are stretched by the tension this readout can not be better than ± 2 cm. This position information was used to analyse the 1997 NMR-data and it proved to be sufficient to determine the average magnetic field in the storage ring at the 0.5 ppm level. The barcode was only used to cross-calibrate the Trolley-drive readout at specific points.

3. The poles of the magnet consist of 36 pieces. Between two pieces the magnetic field is lower than in the middle of the poles. For different Trolley measurements these structures can be compared and the position readout can be checked.

To be able to perform a multi-pole-expansion in the plane perpendicular to the flight direction of the muons an equidistant field-map with 7200 points is interpolated from the raw data. A two dimensional multi-pole-expansion in the horizontal axis x and the vertical axis y describes the magnetic field very well and can be used to calculate the magnetic field at arbitrary locations within the storage volume

$$B_y = \sum_{n=0}^{\infty} C_n \, r^n \; \cos(n\phi) - \sum_{n=0}^{\infty} D_n \, r^n \; \sin(n\phi), \tag{60}$$

$$B_x = \sum_{n=0}^{\infty} C_n \, r^n \; \sin(n\phi) + \sum_{n=0}^{\infty} D_n \, r^n \; \cos(n\phi). \tag{61}$$

The coefficients C_n and D_n are the normal and the skew multi-poles respectively. C_0 and D_0 are the dipole terms, C_1 the quadrupoles, C_2 the sextupoles and so on. Since the field is very homogenous all other coefficients are very small compared to C_0. The field variations produced by the different multi-poles go with r to the n-th power and the field shaping elements of the magnet are far away from the storage region. Therefore the coefficients of the higher multi-poles quickly go to zero [99]. For the magnetic field analysis multi-poles up to $n = 4$ were used. The multi-pole data is used in a particle tracing algorithm which then calculates the average magnetic field seen by the particles [104]

$$\bar{B}(\text{field-map}) = \int \rho_\mu(\vec{r}) \cdot B(\vec{r}) d^3 r, \tag{62}$$

where $\rho_\mu(\vec{r})$ is the muon population at the location $\vec{r}$ integrated over time and $\int \rho_\mu(\vec{r}) d^3 r = 1$. A large number of particles is traced through the ring and the average magnetic field $\bar{B}$ is calculated.
As a cross-check the unprocessed raw data was used to calculate the average magnetic field the 17 probes of the Trolley see

$$\bar{B}_i = \int B_i(\phi) d\phi, \tag{63}$$

where i is the probe number and $\int d\phi = 1$.
The locations of the NMR-probes can be seen in figure 4.15. The comparison in table 5.1 shows very good agreement between the cross-check and the calculated average magnetic field seen by the muons.

The average magnetic field $\bar{B}$ in Gauss-14510 Gauss					
Day	probe 1 inner probe	probe 2-5 mid. circle	probe 6-17 outer circle	probe 1-17 all probes	muon population
26.06	0.8397	0.8384	0.8379	0.8381	**0.8380**
29.06	0.7921	0.7891	0.7918	0.7912	**0.7914**
03.07	2.7626	2.7605	2.7586	2.7593	**2.7594**
06.07	2.9237	2.9208	2.9195	2.9200	**2.9201**
10.07	2.2689	2.2667	2.2656	2.2661	**2.2662**
11.07	2.7117	2.7078	2.7088	2.7087	**2.7089**
The differences between probe averages and the muon population weighted average in ppm					
26.06	0.12	0.03	-0.01	0.01	0
29.06	0.05	-0.16	0.03	-0.01	0
03.07	0.22	0.08	-0.06	-0.01	0
06.07	0.25	0.05	-0.04	-0.01	0
10.07	0.19	0.03	-0.04	-0.01	0
11.07	0.19	-0.08	-0.01	-0.01	0
average	0.17	-0.05	-0.02	-0.01	0
RMS	0.07	0.09	0.03	0.01	0

Table 5.1: *The calculated average magnetic field of the* 6 *field-maps taken during the engineering run. For pion injection the muon population can be obtained using a simulation and assuming a full occupation of all available phase space. Results from direct muon distribution measurements are not available yet. The differences between taking the average field seen by one or some of the NMR-probes in the Trolley and the muon distribution weighted average is very small. This fact and the small RMS values of the results add confidence in the calculations and measurements.*

The results shown in table 5.1 lead to the following conclusions :

- The interpolation of the data points in azimuthal direction as well as the multipole expansion and the particle tracking code work fine and the accuracy is not limited by the calculation accuracy.
- The calibration of the different NMR-probes inside the Trolley does not shift on the 10^{-7} level between the measurements.
- The number of $\approx$ 6000 data points in azimuthal direction is sufficient to measure the magnetic field to 0.1 *ppm* as proposed in the design report.

For the experiment it is necessary to know the average strength of the magnetic field at any given time. After a field-map is taken and even during the time when the field-map is taken the field-changes have to be tracked. This is done with a subset of the 366 fixed NMR-probes located on top and below the vacuum chambers at 72

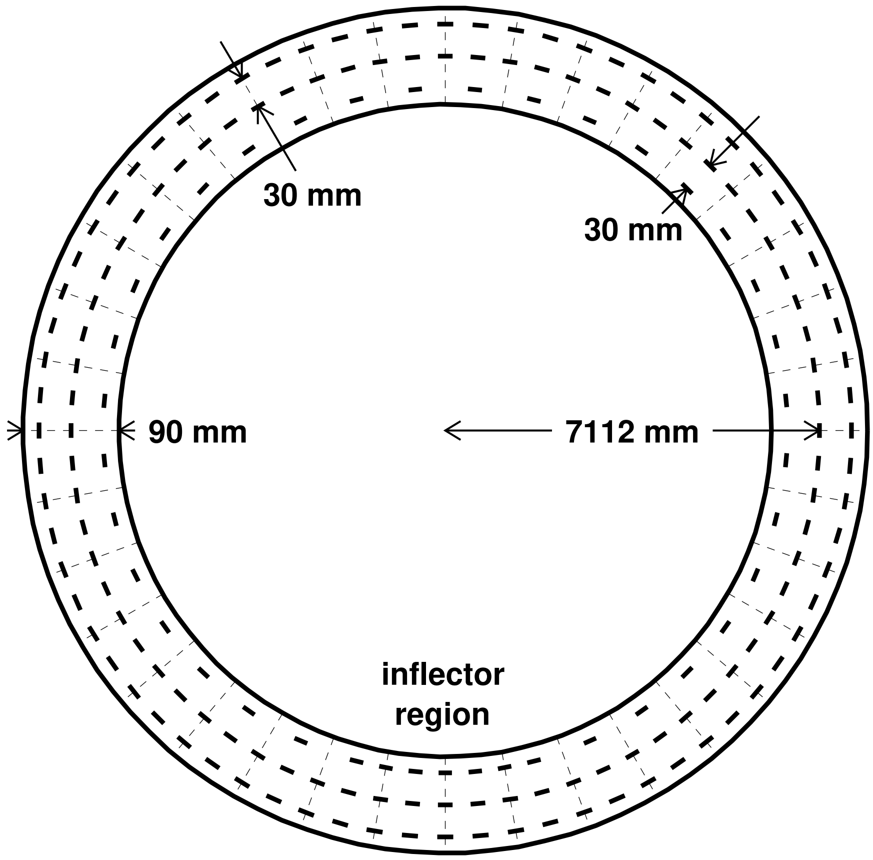

Figure 5.1: *The locations of the fixed NMR-probes. The figure is not to scale and the layout of the poles is not shown in exact detail. They are not symmetric, otherwise it would be impossible to mount or dismount them. There are 183 probes indicated in their position, the probes on top and below the vacuum chambers are at the same azimuthal positions. Since there are probes at different radii and above and below the vacuum-chambers it is also possible to track changing field gradients in these directions.*

azimuthal locations shown in figure 5.1. The average magnetic field is then

$$\bar{B}(t) = \frac{1}{108}\sum_{i=1}^{108} B_i(t) + C_{cal}, \tag{64}$$

where the $B_i(t)$ are the magnetic field values measured by the 108 fixed probes used for this analysis and C_{cal} is a calibration offset, very small compared to the absolute value of $\bar{B}$. The magnetic field is always expressed in terms of the Larmor frequency of protons in water and the final result is given as the Larmor frequency of free protons at the field $\bar{B}(t)$.

A difficulty arises from the fact that it takes about 1 hour to obtain a field map and the average magnetic field can change up to $1\,ppm$ during that time. Therefore each fixed probe has to be evaluated at the time when the Trolley passed the probes

azimuthal position.
Since the Trolley itself influences the magnetic field as shown in figure 4.14, the value is interpolated between the values $60\,s$ before and $60\,s$ after the Trolley passed this fixed probe. Using this method the effects of the Trolley on the magnetic field as well as the time drift are negligible.
The value C_{cal} for each field-map is then given by

$$C_{cal} = \bar{B}(\text{field-map}) - (1/108)\sum_{i=1}^{108}(B_i(t_i - 60s) + B_i(t_i + 60s))/2, \qquad (65)$$

where B_i is the magnetic field seen by probe i and t_i is the time when the Trolley passed this probe.
Figures 5.2, 5.3 and 5.4 show the average magnetic field obtained using equation 62, 64 and 65 during the three measurement periods. The abrupt changes are due to the beam-line magnets which are switched off during times without beam to conserve energy ($4\,MW$). The enlargements with the Trolley measurements indicate the values obtained by the field-maps.

Figure 5.5 shows the room temperature and the average yoke surface tempera-

Date	Time	Calibration offset C_{cal}
26.06.97	21:30	-10.6 ppm
29.06.97	20:15	-10.3 ppm
Average Period 1		-10.5 ppm
03.07.97	15:15	-6.7 ppm
06.07.97	20:45	-6.6 ppm
Average Period 2		-6.7 ppm
10.07.97	6:45	-11.2 ppm
11.07.97	14:45	-10.1 ppm
Average Period 3		-10.6 ppm

Table 5.2: *The calibration offset between the average NMR-frequency of the selected fixed probes which is proportional to the magnetic field and the average free proton NMR-frequency ω_p which is used to calculate $a_\mu = R/(\lambda - R)$, where $R = \omega_a/\omega_p$ and $\lambda = \mu_\mu/\mu_p$. ω_a is the measured $g_\mu - 2$ oscillation frequency, μ_μ is the magnetic moment of the muon and μ_p is the magnetic moment of the proton. The offsets in period 1 and period 3 agree whereas period 2 is different due to a magnet quench between period 1 and 2.*

ture of the magnet during the last measurement period. The temperature curves are shifted because of the big heat capacity of the magnet. Comparing this curve with figure 5.4 shows the correlation between temperature and the strength of the magnetic field. It has to be taken into account that the average yoke temperature lags behind the surface temperature by another $6-8$ hours.
There is not only a direct correlation between temperature and the strength of

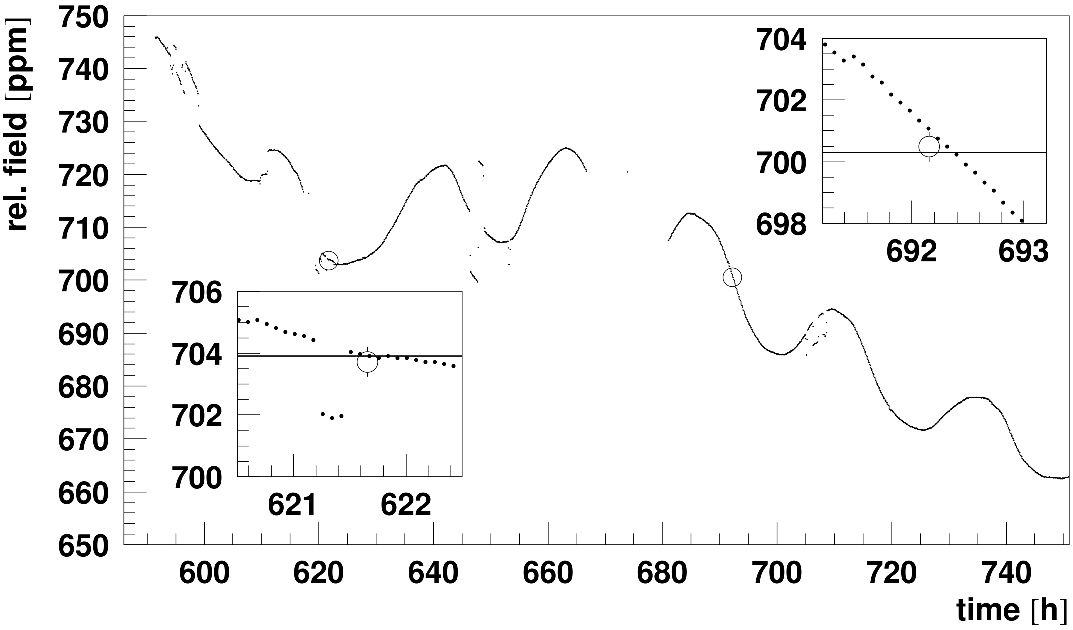

Figure 5.2: *The average magnetic field in the storage ring during the first measurement period versus time. At times when the beam-line magnets are turned on and off or when the inflector magnet is tuned there are abrupt changes. The time is measured in hours starting at 01.06.97 0:00. The two dots indicate the results of the two Trolley field-maps during this period. They are also shown in the enlargements. The horizontal lines represent the calculated average field of the fixed probes during the field-map measurement as explained in the text section. The calibration offset determined using the two field-maps is already taken into account.*

the magnetic field, the temperature gradient in the magnet yoke dependent on $dT(room)/dt$ also contributes to the thermal effects. The inwards pointing side of the yoke is fairly well isolated by the vacuum-chambers and cryostats while the other side pointing towards the walls of the building is not. If the temperature rises, this part of the yoke expands, bending the magnet. This effect does not only change the dipolar component of the magnetic field, it also changes the normal quadrupole component up to $2.5\,ppm$ at $4.5\,cm$ radius. The change of the quadrupole component shows the same time dependency as the difference between the room temperature and the magnet surface temperature. It is important to note that it is much easier to trace the change in the dipolar field with the fixed probes. The quadrupole change is obtained by subtracting the magnetic field seen by a set of fixed probes at bigger radius from a set at smaller radius. At the current level of accuracy it is not necessary to take the change of the quadrupole component into account for calculating the field averages, the effect can be estimated to be less than $0.1\,ppm$ due to the homogeneous beam distribution.

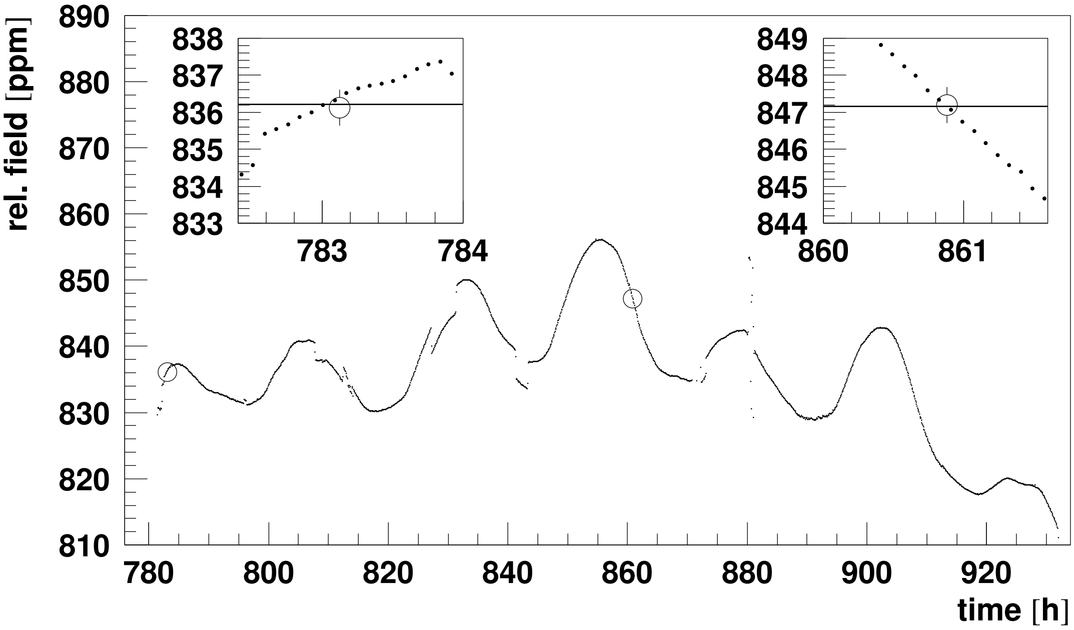

Figure 5.3: *The average magnetic field in the storage ring during the second measurement period versus time. Most of the muon decay data was taken during this period and period three.*

Between January and March 1998 the magnet has been thermally isolated and therefore these effects are smaller by at least a factor of 5 as measured in preliminary tests.

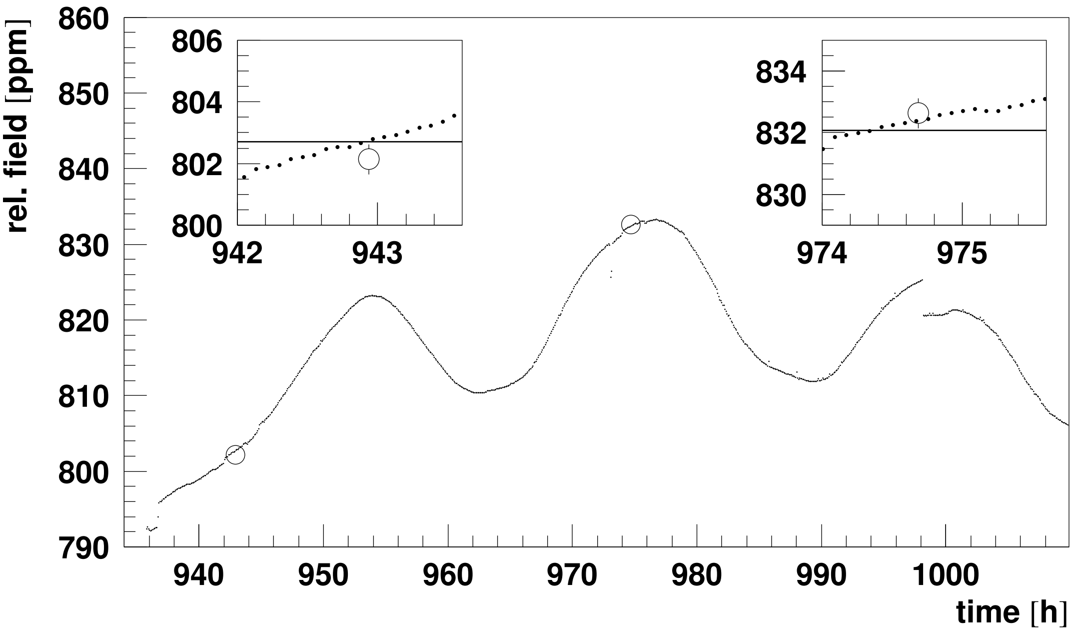

Figure 5.4: *The average magnetic field in the storage ring during the third measurement period versus time. During this period the temperature change inside the experimental hall was biggest. The two Trolley measurements were taken at the temperature extremes: At 6:00 in the morning and at 15:00 during the afternoon. Therefore there are small deviations between the Trolley field-maps and the prediction measured with the fixed probes. These deviations can be reduced by taking into account the magnetic field seen by the fixed probes near to the pole edges which have not been included in this years data analysis. Additionally, since the magnet is now thermally isolated, the temperature change will be reduced by at least a factor of 5.*

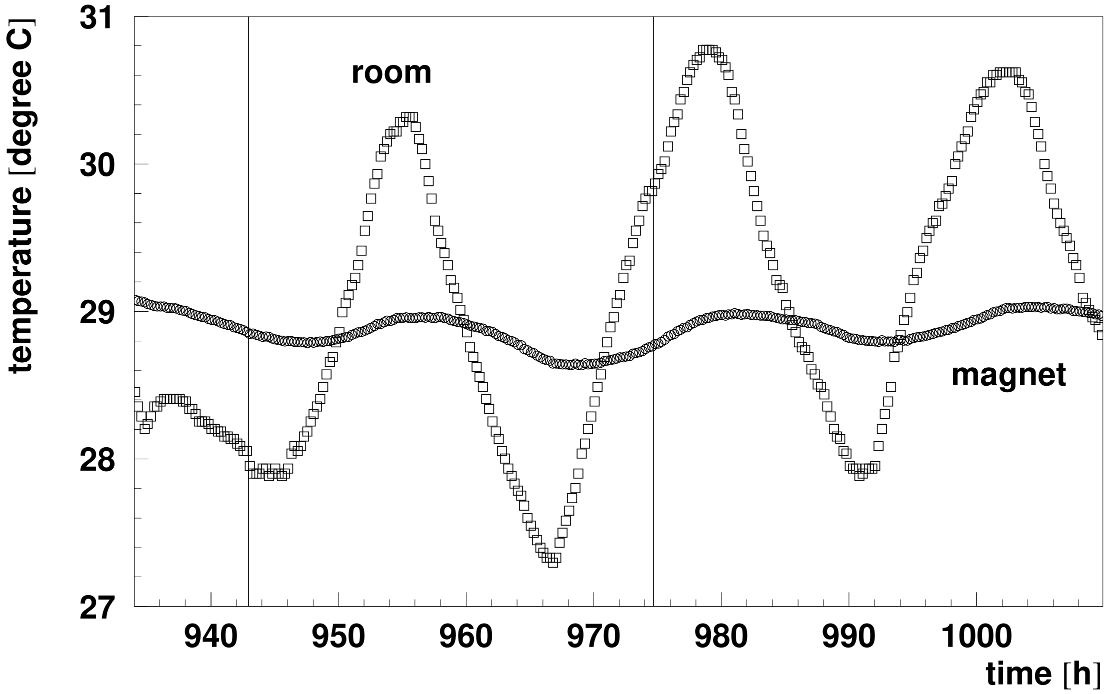

Figure 5.5: *The temperature inside the experimental hall and the average of 12 temperature probes located at outer surface of the iron yoke. The times when trolley-runs were taken are indicated by the two lines. The minima and maxima of the magnet temperature are time-shifted against the minima and maxima of the room temperature and the differences are smaller. This is due to the large heat capacity of the magnet.*

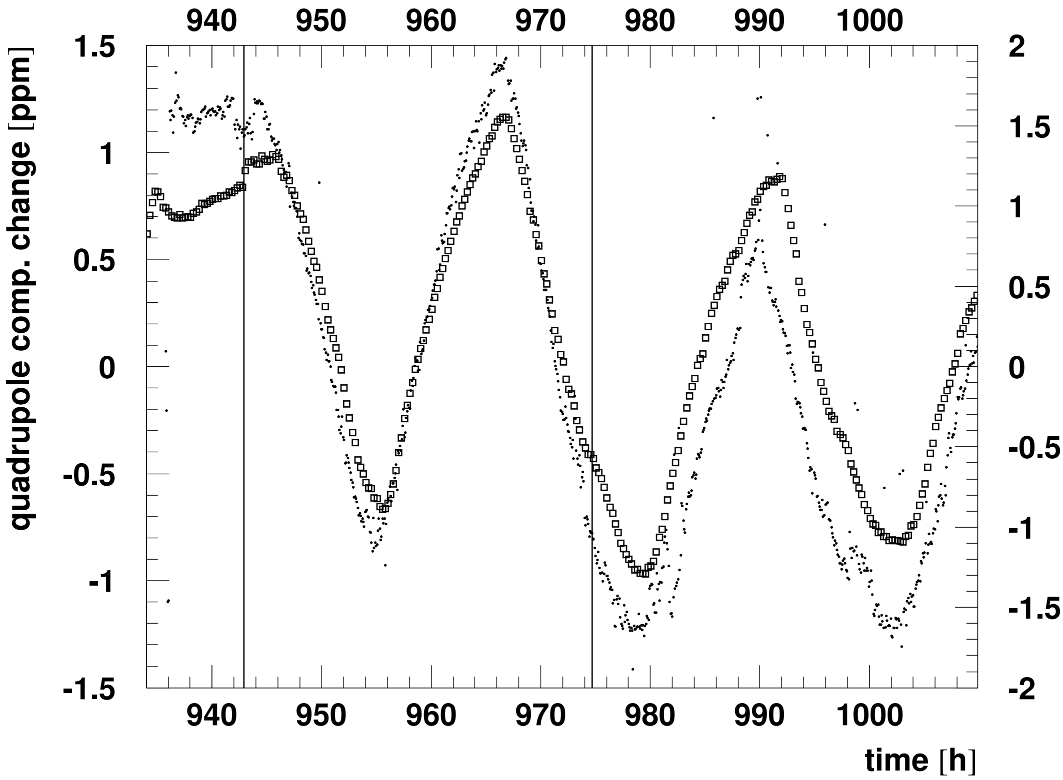

Figure 5.6: *The squares and the dots indicate the temperature difference between the magnet yoke and the experimental hall and the change of the quadrupole component of the magnetic field respectively. The correlation can be explained by a temperature gradient in the yoke of the magnet. During day the outwards facing side is heated by the warm air in the experimental hall whereas the inwards facing side is well isolated by the vacuum chambers. The yoke starts to bend inwards thus inducing a change in the quadrupole gradient in radial direction due to misalignment of the poles. During nights the effect is reversed. Since the magnet is thermally isolated now, the effect is at least a factor of 5 smaller.*

5.1 The Uncertainties of the Magnetic Field Measurement

The magnetic anomaly is obtained through equation (35)

$$\omega_a = \omega_s - \omega_c = a_\mu \left(\frac{e}{2m_\mu c}\right) B \quad , \quad a_\mu = \frac{m_\mu c}{eB}\omega_a. \tag{66}$$

Therefore the magnetic field should be known significantly better than the relative accuracy in ω_a which in the optimal case will depend on statistics mainly and is in principle limited by running time. The accurate measurement of the magnetic field in absolute terms is crucial for the $g_\mu - 2$ experiment in Brookhaven. To reach the design accuracy of $0.35\,ppm$ in a_μ it is necessary to determine the average magnetic field to $0.1\,ppm$. Several uncertainties contribute to the overall uncertainty in the absolute magnetic field value.
The statistical error due to noise for a single $250\,\mu s$ NMR-measurement with the Trolley is $0.1\,ppm$ RMS. The noise shifts the time when the signal height crosses the threshold of the counters [89]

$$\frac{\Delta\omega_L}{\omega_L} = \frac{1}{[S/N]_{t=t_{gate}}} \cdot \frac{1}{\omega_L \cdot t_{gate}}, \tag{67}$$

where ω_l is the Larmor frequency of the nuclei, $[S/N]$ is the signal to noise ratio and t_{gate} is the duration of the measurement. This uncertainty shows a Gaussian distribution which can be seen in figure 4.9. Since a field-map consists of a large number of NMR-measurements this uncertainty is completely negligible for determining the average magnetic field.
There are several sources for systematic uncertainties of a single measurement point.

1. The difference of the Larmor frequency of protons in a spherical water sample and the Larmor frequency of free protons is $(25.790 \pm 0.014)\,ppm$ [95, 96] at $34.7\,^\circ C$ water temperature and the temperature correction is $(0.01036 \pm 0.00030)\,ppm/\,^\circ C$ [92]. The temperature in the experimental hall was $(29 \pm 4)\,^\circ C$. The corresponding uncertainty of not taking temperature changes into account is smaller than $0.05\,ppm$.

2. The absolute calibration of the standard probe used was done by Fei, Prigl and Hughes in 1996 [90]. The offset between the NMR-frequency of this probe and a pure spherical water sample was measured to be $(-0.044 \pm 0.034)\,ppm$.

3. The preliminary calibration of the NMR-probes inside the Trolley versus the standard probe is described in the chapter 4.4 on the Trolley calibration. The overall uncertainty mainly due to positioning uncertainties during the calibration is $0.5\,ppm$.

Therefore the systematical uncertainty for a single measurements is $0.5\,ppm$. Further uncertainty arises from tracking the magnetic field with the fixed probes. Since the shimming of the magnet was not finished in 1997, many probes, particularly those

at the edges of the poles, had a very bad signal quality due to big field gradients. It is possible to select 108 probes with a statistical uncertainty of less than $0.2\,ppm$ per single shot. All those probes are located azimuthally in the middle of the poles. Radially 36 probes are at positions $3\,cm$ inwards from the center of the storage region, 36 are centered and 36 are positioned $3\,cm$ outwards from the radial center of the storage region. This allows to monitor changes in the field gradient. Figure 5.6 was obtained that way.
The regions near to the edges of the poles have been monitored too, but it was not possible to use all the NMR-probes at some locations due to the large field gradients. The magnetic field values there differ up to $1\,ppm$ from the values obtained in the middle of the poles due to thermal motion. It has been measured that the average magnetic field is affected by this effect to $0.5\,ppm$ using comparisons between the field changes measured by the fixed probes and field changes seen by the Trolley. It was also shown that combining the data obtained by selected 108 probes with data from probes near to the pole edges can improve the accuracy of the tracking. Since it was not possible to obtain this additional data at all locations it was decided to use the probes in the center of the poles only. The field seen by the probes at the edges and the ones in the middle of the poles varies by $\pm 1\,ppm$. Since only the probes in the middle of the poles are used for tracking the average magnetic field this causes an uncertainty of $0.5\,ppm$.
The change of the normal quadrupole component was tracked but the information was not used for the analysis. As can be seen from figure 5.6 the normal quadrupole varied about $\pm\,1 ppm$ during the measurement. Since the beam distribution is well centered over the storage cross-section for pion injection the effect caused by this variation is less than $0.1\,ppm$ according to beam dynamics Monte Carlo simulations.
The position of the Trolley in z-direction was only known to $\pm 2\,cm$ during the measurement. This adds another uncertainty since the position information is used to generate the field-map. Only one probe can be measured at a time, therefore all measurements are acquired at different positions since the NMR-Trolley is moving during the measurements. The uncertainty of the position readout has a symmetric distribution. Therefore the shifts of the average field caused by the inaccuracy of the position readout cancel out to a large degree. Statistical considerations comparing different field-maps give that the uncertainty of this effect is less than $0.2\,ppm$ for a complete field-map. It is also possible to calculate a rough estimate for the worst case: The biggest field deviation is near to the inflector. There the field is about $300\,ppm$ lower than the average. If $\pm 2\,cm$ of this section were not taken into account that would change the final result by $0.04\,m/45\,m \cdot 300\,ppm = 0.27\,ppm$ upper limit. Another possibility to estimate this effect is comparing the average field seen by different probes during the same field-map and compare the difference with the differences in other field-maps. For example the difference for the average field measured by probe one minus the average of all probes at a radius of $1.75\,cm$ is $0.18\,\pm\,0.06\,ppm$. The offset is most probably due to the calibration uncertainty. It would be very unlikely that this result obtained by 6 independent measurements would show such a small deviation if the average value measured by the inner probe would not be stable. It should also be noted that the position readout was cross

calibrated against the position of the pole edges which can be found by analysing the measured magnetic field data. No non-linearity and no deviation bigger than $\pm 2\,cm$ was found. Therefore it is safe to assume that the uncertainty due to the limited accuracy of the position readout is less than $0.3\,ppm$.
In the inflector region there are locations where it was impossible to perform NMR-measurements with the regular NMR-Trolley setup due to the big gradients in the magnetic field. Additional data was collected in dedicated inflector field-maps using different probes with a smaller active volume. This data was fitted into the normal data to improve the measurement. In average about $10\,cm$ of the regular data was replaced. Since the differences between the regular field-maps and special inflector field-maps are less than $10\,ppm$ at positions where there is data available for both the uncertainty due to the replacement is less than $0.1\,m/40\,m \cdot 10\,ppm = 0.025 ppm$. However, even in the dedicated field-maps there is no data available for about $8\,cm$ in azimuthal direction for the 3 probes next to the inflector. The data of the other probes could be used to do a multi-pole expansion and then to calculate the magnetic field. However multi-pole expansions with a limited number of measured positions and therefore a limited number of multi-poles are unreliable if there are local effects changing the field. The higher multi-pole coefficients only go to zero if the changes are produced by inhomogeneities far away from the center which therefore cover a wide angular range. Since the field changes are produced by the nearby inflector magnet this is clearly not the case.
A calculation has been done by Morse [105] using a mathematical model of the current distribution in the inflector shield which showed that the total effect of the inflector magnet on the average magnetic field seen by the muons is $0.5\,ppm$. It is also possible to do an estimate of the uncertainty due to the missing data. The field measured by the central probe decreases about $120\,ppm$ at that azimuthal position, the field measured by the probe which is located at $x = +17.5\,mm$, nearer to the inflector, decreases about $280\,ppm$ and the field at $x = -17.5\,mm$ is only reduced by $50\,ppm$. The change gets bigger by a factor of 2.4 every $17.5\,mm$. At the inflector this would mean that the field shows a dip of about $700\,ppm$ which also agrees with calculations. Assuming $1000\,ppm$ yields a change in the average field of $0.08/40 \cdot 1000 ppm = 2\,ppm$. Only a small fraction of the muon population passes through this part of the cross-section of the storage ring, less than 25%. This gives an upper limit for the uncertainty due to the inflector of $0.5\,ppm$.
There could be another uncertainty due to the inhomogeneities : The shape of an NMR-signal changes if the magnetic field has a gradient as depicted in figure 4.23. This causes the measured frequency from the FID-signal to be slightly different from the real frequency average of the nuclei in the probe [106]. This effect is smaller than $0.2\,ppm$ for a normal measurement of $300\,\mu s$ length and is symmetrically distributed for a large number of measurements at different positions with different gradients. It therefore has no effect on the result.
All uncertainties are added together in quadrature, taking into account that they are independent of each other and yield a total uncertainty of $1\,ppm$ for the average magnetic field value during the relevant data taking periods in 1997.

Reason for uncertainty	Uncertainty single measurement	Uncertainty magnetic field average	Improvements 1998
electronics noise	$0.1\,ppm$	$< 0.01\,ppm$ -	
absolute calibration Trolley versus free proton Larmor frequency	$0.5\,ppm$	$0.5\,ppm$	calibration plunging probe and shimming
tracking average field with fixed NMR-probes	-	$0.5\,ppm$	thermal insulation of magnet and shimming
quadrupole change	-	$< 0.2\,ppm$	thermal insulation and including in Monte-Carlo
position readout Trolley	-	$0.3\,ppm$	improving barcode and shimming
large gradients in inflector field	-	$0.5\,ppm$	dedicated field-maps, shimming, new inflector (end 1998)
effect of large gradients on shape of NMR-signal	$0.2\,ppm$	$<< 0.1\ ppm$	shimming of the magnet
Sum		**1 ppm**	mainly shimming

Table 5.3: *Summary of the statistic and systematic uncertainties in the B field measurement.*

6 The Results of the 1997 Measurement

The analysis of the data collected during the engineering run in 1997 has been completed. The first step was to identify the decay positrons in the digitized raw data which were characterized by exceeding a certain threshold energy value in the calorimeters and a particular time dependent shape. Then the typical pulse shape for positrons was fitted to the data to determine the energy and the exact time when the positron hit the calorimeter. It is important to discriminate the positron data from the huge amount of background due to the pion-injection which causes a tremendous amount of decay particles including neutrons. Background from γ's and n's can be discriminated due to the significantly lower energy and pulse shape as compared to the shower signals. The decay data taken directly after injection has been discarded since it is impossible to observe single positron pulses during that time.

The ideally expected decay signal for each of the calorimeter stations, which can be regarded as separate experiment each is

$$N(t) = N_0 \cdot e^{(-t/\tau_\mu)} \cdot (1 + a\cos(\omega_a t + \phi)), \tag{68}$$

where N_0 is proportional to the number of decay positrons in the sample, τ_μ is the muon lifetime where time dilatation has to be taken into account, a is the asymmetry, ω_a is the frequency which is proportional to the magnetic anomaly of the muon and ϕ is an arbitrary phase.

4 parameters are unknown and τ_μ may not be the real muon lifetime if there are beam losses. If τ_μ is fitted to the data too, it can also provide information about the quality of the fit.

This fit was used to process the data and the result obtained with this fit agrees with the other methods within the error bars, however it is not possible to achieve a chi-square of 1 since this fit does not describe the experiment completely.

The large amount of background causes a difficulty. There are thresholds for the wave form digitizers used to digitize the decay pulses. If the signal passes this threshold the digitizers start to sample the signal. If there is background added to the real signal this threshold can also be passed by a smaller pulse. Therefore the sample of positrons at the beginning of the measurement has a lower average energy than the positrons at the end. Lower energy means lower decay asymmetry, thus rising the asymmetry to the end. Since the change is small it is possible to linearize the problem $a(t) = a_0 + a_1 \cdot t$. Also beam losses have to be taken into account and there is a very small amount of constant background N_B which adds another parameter. The fit function is

$$N(t) = N_B + N_o \cdot (1/t)^\alpha \cdot e^{(-t/\tau_\mu)} \cdot (1 + (a_0 + a_1 \cdot t) \cdot \cos(\omega_a t + \phi)), \tag{69}$$

where N_B, α and a_1 are the additional parameters, constant in time for a single detector and a beam period, due to the background. The term $(1/t)^\alpha$ was empirically found to describe gain changes and muon losses. This 8 parameter fit typically gives a chi-square which agrees with 1. The additional parameters are only very weakly

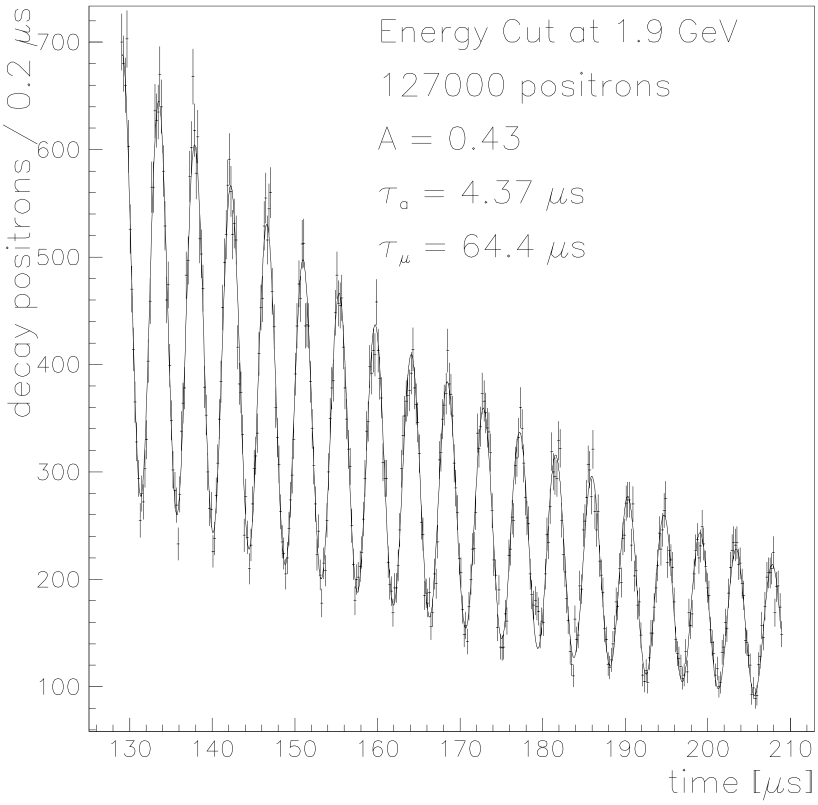

Figure 6.1: *The decay signal of the muons in the storage ring. The frequency due to the magnetic anomaly can be seen. The data is just a small fraction of the measured positron decays. The asymmetry is bigger than at CERN by about* 10% *(*$\approx$ 40% *instead of* 30%*) due to the minimization of scattering in the vacuum chamber by an appropriate shape of the vacuum tank.* τ_a *is the inverse anomaly frequency* ($\omega_a = 2\pi/\tau_a$)*.*

correlated with ω_a, the only parameter strongly correlated with ω_a is the arbitrary phase ϕ as observed already in the last CERN experiment [18]. The fit starts at different times after the injection for different detectors with a delay ranging from $35\,\mu s$ to $100\,\mu s$ depending on the location of the detectors. As a cross-check there was another fit method applied to the data called ratio fit which eliminates the exponential term before performing the fit. The result agreed with the two other fits within the error-bars. For t in units of $100\,\mu s$ typical values of the parameters are $1 < \alpha < 2$, $a_0 \approx 35\%$ and the asymmetry rises about 10% for late positrons. The averaged anomaly frequency from the 8 parameter fit is

$$\omega_a = 229.0633\,kHz \pm 13\,ppm. \tag{70}$$

All these fits were applied separately to the 3 measurement periods and the 20 detector stations used in this analysis and then the results were combined. The

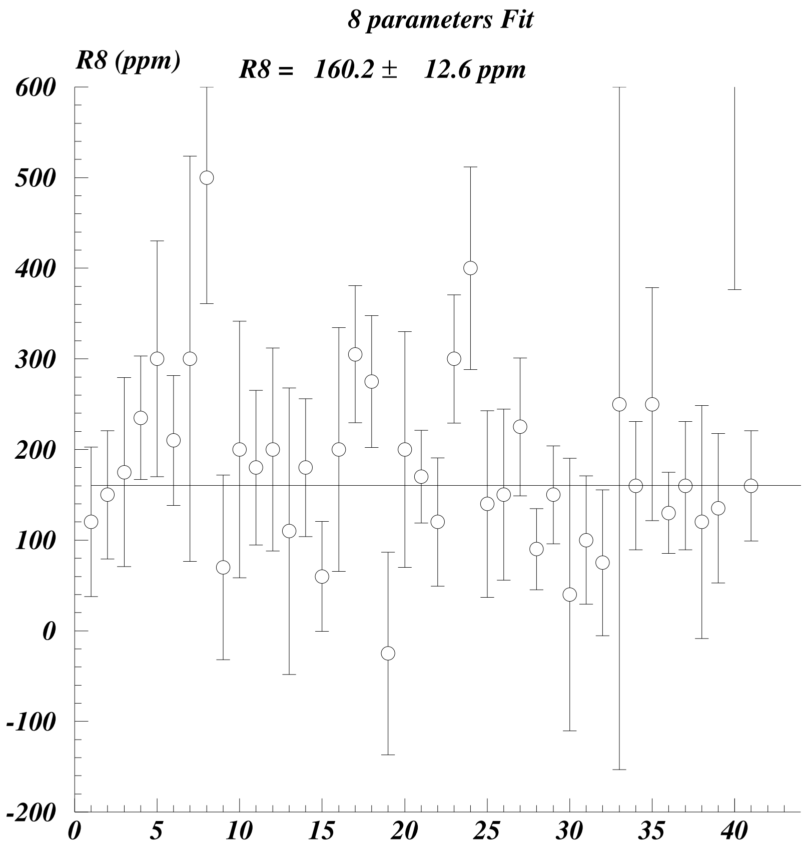

Figure 6.2: *The results obtained in 3 measurement periods for individual detector stations. Since tests for improving the detectors were performed simultaneously not all could be included. 3 detectors near to the inflector could not be used due to pion flash.* $\omega_a = 2\pi \cdot 229.1\, kHz(1 - 10^{-6} \cdot R_8)$ *for a magnetic field equivalent to* $\omega_p = 2\pi \cdot 61788.5 kHz$ *yielding* $a_\mu = 1.165925 \cdot 10^{-3} \pm 13\, ppm$.

typical duration of one run is about one hour. During that time the magnetic field typically changes about 1 to $2\, ppm$. Therefore an average magnetic field can be calculated for each run and then the time scale of $N(t)$ for each run was stretched as if all the data was obtained at constant magnetic field strength equivalent to $\omega_p/2\pi = 61788500\, Hz$. The final ratio of anomaly and proton resonance frequency R is

$$R = \frac{\omega_a}{\omega_p} = 3.70722(5) \times 10^{-3} \tag{71}$$

with

$$\omega_a = 2\pi \cdot 229.1\, kHz\, (1 - R_8 \times 10^{-6}) \quad \text{and} \quad \omega_p = 2\pi \cdot 61788.5\, kHz. \tag{72}$$

Together with [107] muon magnetic moment in units of the proton magnetic moment

$$\lambda = \frac{\mu_\mu}{\mu_p} = 3.18334547 \pm 0.15\, ppm \tag{73}$$

we obtain

$$\mathbf{a}_\mu(\mathbf{BNL}) = \frac{\mathbf{R}}{\lambda - \mathbf{R}} = \mathbf{1.165925 \times 10^{-3} \pm 13\,ppm}. \tag{74}$$

This value fully agrees with the last CERN results and with the present theoretical predictions. As a combined result of all $g_\mu - 2$ experiments one finds

$$a_\mu(\text{combined}) = \frac{R}{\lambda - R} = 1.165923 \times 10^{-3} \pm 6.5\,ppm. \tag{75}$$

This starting run has proven the feasibility of the $\mathbf{g}_\mu - \mathbf{2}$ experiment at BNL.

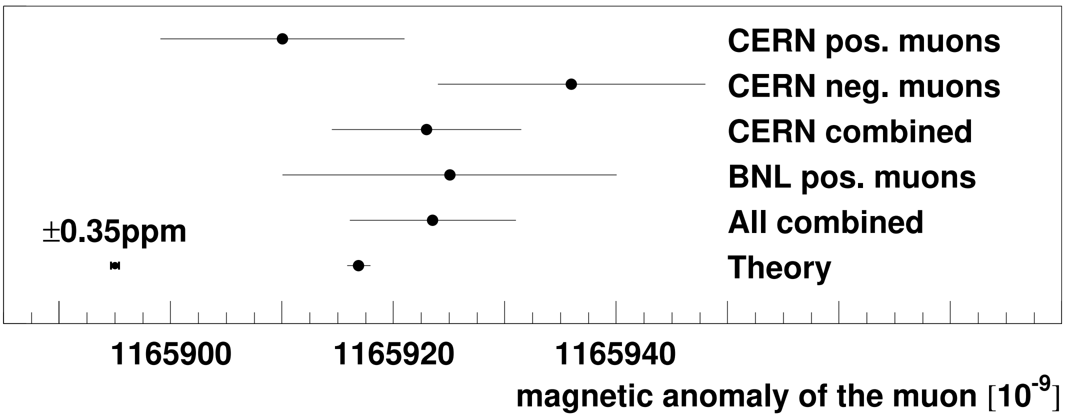

Figure 6.3: *The results of the new measurement of the magnetic anomaly of the muon at BNL compared with the values obtained at CERN. Additionally the uncertainty of todays theoretical prediction is shown and the proposed accuracy of the new $g_\mu - 2$ experiment is indicated.*

7 Outlook

The engineering run of the new $g_\mu - 2$ experiment in 1997 was able to provide data to determine the magnetic anomaly of the muon to an accuracy comparable to the CERN III experiment within 14 days of data-taking. Many improvements have been implemented since to further enhance the accuracy of the measurement.

1. The muon kicker has been tested extensively and is now being installed. It will improve the number of stored muons by an order of magnitude and at the same time reduce the background due to decaying pions. This will make it possible to take data at earlier times, thus additionally improving the number of measured decay positrons significantly.

2. The calorimeters have a higher efficiency now due to refurbishing the light couplers between the scintillators and the light guides. A fabrication error has been discovered as a result of the engineering run. This will improve the timing and gain stability.

3. A second iteration of the shimming process is in progress. The additional shimming improves the homogeneity of the magnetic field in azimuthal direction as well as it decreases the size of the higher multi-pole components of the magnetic field.

4. The storage ring magnet is thermally isolated now and active feedback from the fixed probe NMR-system will be used to control the current of the main power supply. This will keep the dipole component of the magnetic field stable against temperature changes and also reduce the change of the normal quadrupole component significantly. Temperature changes at the yoke have been measured to be 5 times smaller than before.

5. A new inflector magnet is in construction at KEK. It will not be operational for the next data taking period in summer 1998 but after that it will improve the magnetic field homogeneity in the inflector region. The magnetic field near to the old inflector is being mapped very carefully and magnetic field information will be obtained at all locations using improved NMR-measurements making use of different NMR-probes. In addition the regions with the largest field gradients are being mapped by precision Hall probes.

With all these improvements it is expected to reach an accuracy of about $1\,ppm$ within 2 to 3 weeks of data taking and it is possible to reach the proposed accuracy of $0.35\,ppm$ in a reasonable time ($\approx$ 18 to 27 weeks). By inverting the magnetic field of the storage ring and inflector magnet it is possible to measure the magnetic anomaly of the negative muon as an important test of the CPT theorem. It is planned to do this in additional runs. Since high energy protons shot on a target produce twice as many positive pions as negative pions the expected rate for measuring negative muons is about half the rate of the positive ones.

The electric dipole moment (edm) can be extracted from the experiment in two ways.

1. The uncertainty in a_μ can be converted into an edm upper limit [18].

2. A finite edm of the muon would result in a time dependent up/down asymmetry of the decay positrons which can be detected by the PSD and FSD detectors.

There are two working groups preparing possible proposals :

- One is to measure the mass of the muon-neutrino using the storage ring as a precision spectrometer [108]. By injecting relativistic pions and comparing the positions of the decay muons after one single turn in the magnet with the ones of pions one can expect a sensitivity of about $8\,keV/c^2$ which is 20 times better than the present limit obtained at PSI [109]. Since the proposed experiment would measure with highly relativistic pions ($\gamma = 22$) the uncertainty of the pion mass would not pose a problem for this type of measurement as it is the case for the PSI experiment. The existing magnetic field measurement system built for the $g_\mu - 2$ experiment would be of essential importance.

- The other is a dedicated measurement of the electrical dipole moment of the muon[110] . This experiment would have to change the geometry of the poles and would run at a lower magnetic field. The best upper limit so far from the CERN $g_\mu - 2$ experiment for the electric dipole moment of the muon is $3.4 \pm 3.7 \times 10^{-19}\,ecm$, where e is the muon charge. With a dedicated electric dipole experiment using the $g_\mu - 2$ storage ring it would be possible to achieve a limit of $1 \times 10^{-24}\,ecm$. Since the electric dipole moment of the muon is enhanced compared to the electron by a factor of $m_\mu/m_e \approx 207$ this experiment would be competitive or better than the results for the electric dipole moment of the electron $(-0.27 \pm 0.83) \times 10^{-26}$ [111].

Another important detail in connection with the $g_\mu - 2$ experiment concerns the absolute calibration of the NMR-probes. Even though the calibration is known to 1.4×10^{-8} [90, 96] it would be advantageous to have an independent measurement not relying on the reproducibility of original work.
For ^3He the screening factor of the electrons on the magnetic field seen by the nucleus can be calculated and the magnetic moment of the ^3He nucleus is known to 4 ppb [112]. A comparison between the NMR-frequency of gaseous ^3He and water in the same magnetic field can provide an independent absolute calibration for the magnetic field measurement system.

A Circuit Diagrams of the Trolley Electronics

1. The preamplifier for the NMR-signals.
2. The barcode reader for the position readout.
3. The communication module for the one-cable solution.
4. The same module inside the NMR-Trolley.
5. The analog part of the NMR-electronics.
6. The digital part of the NMR-electronics.

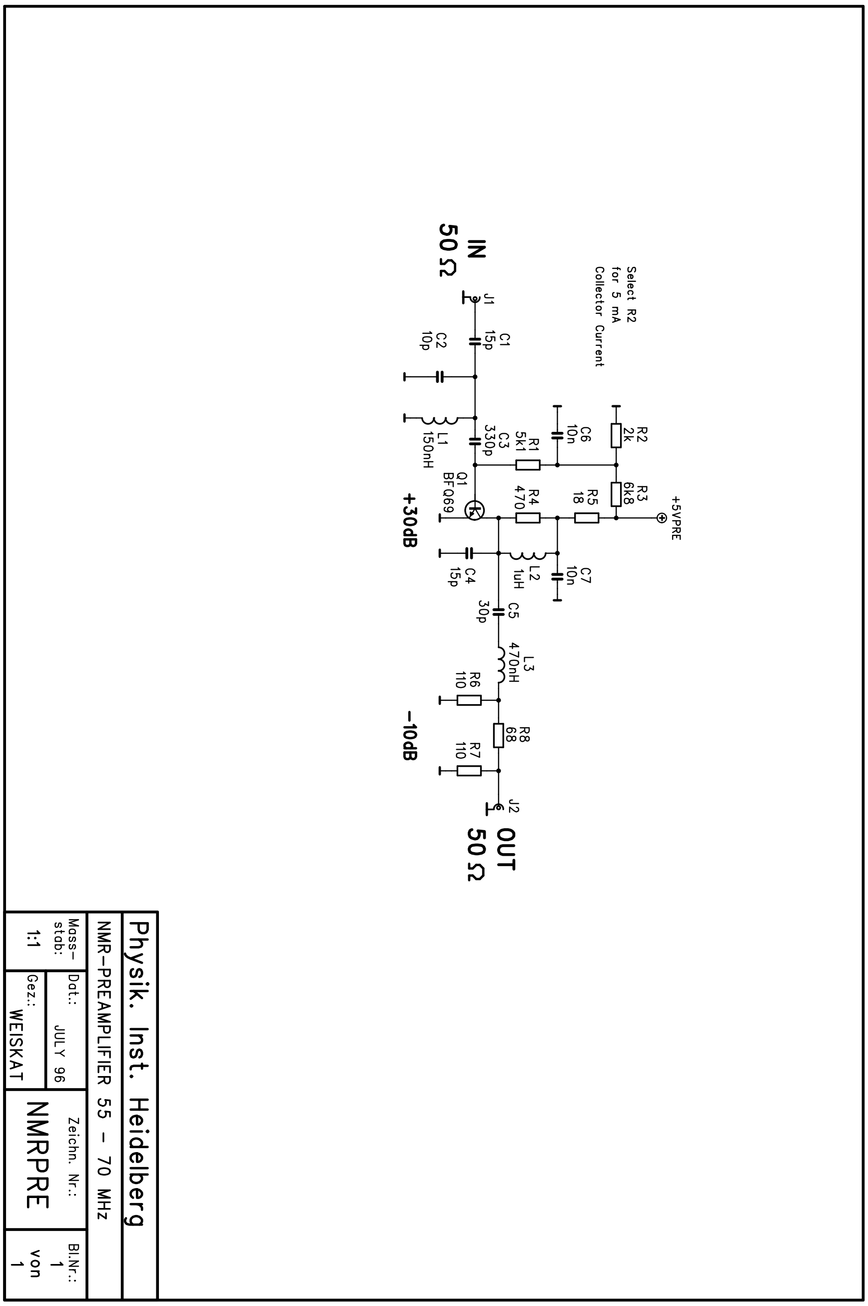

Figure A.1: The preamplifier. The preamplifier is located in a separated housing to reduce crosstalk with the reference frequency and the frequencies produced by the digital part.

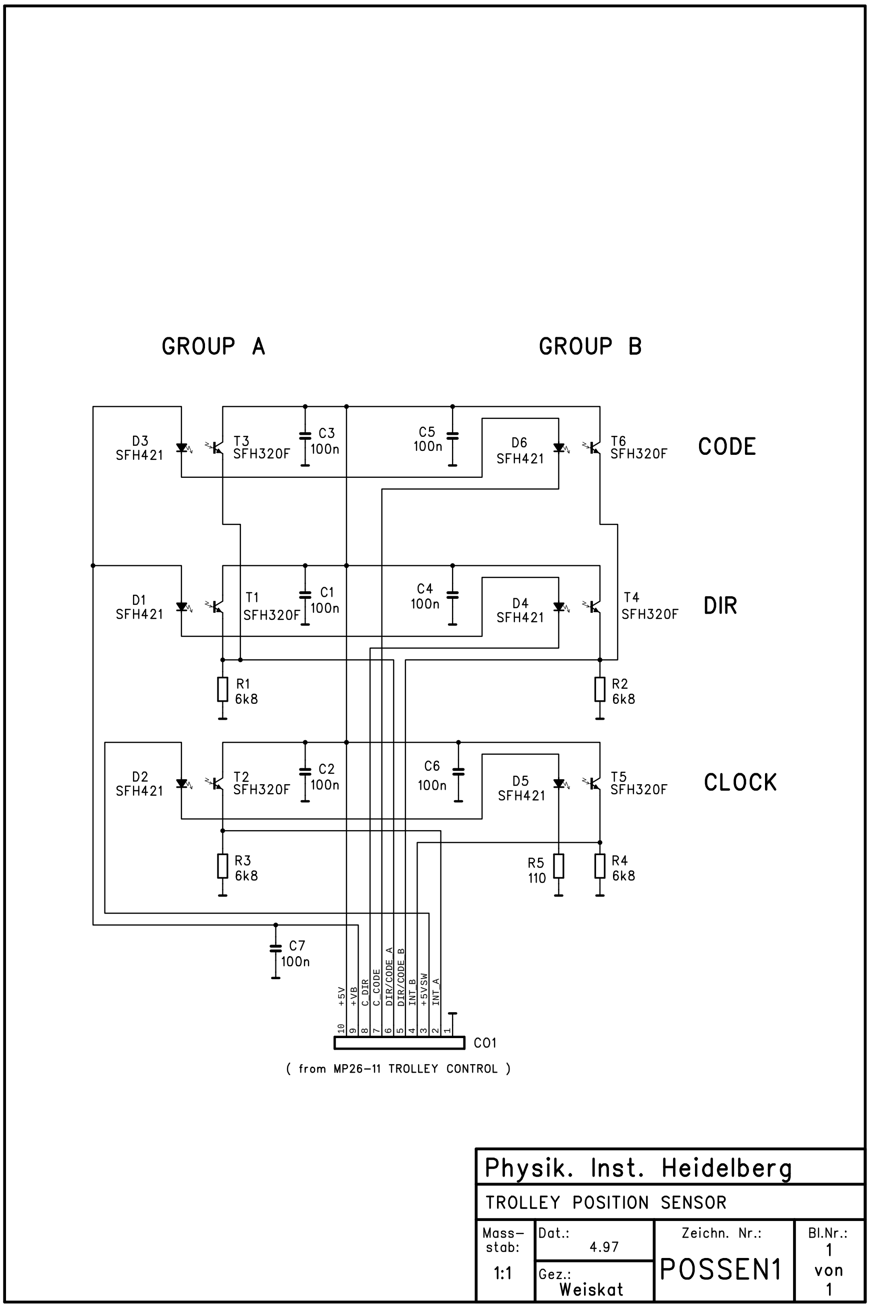

Figure A.2: The barcode reader. This part of the electronics is located outside the vacuum-housing.

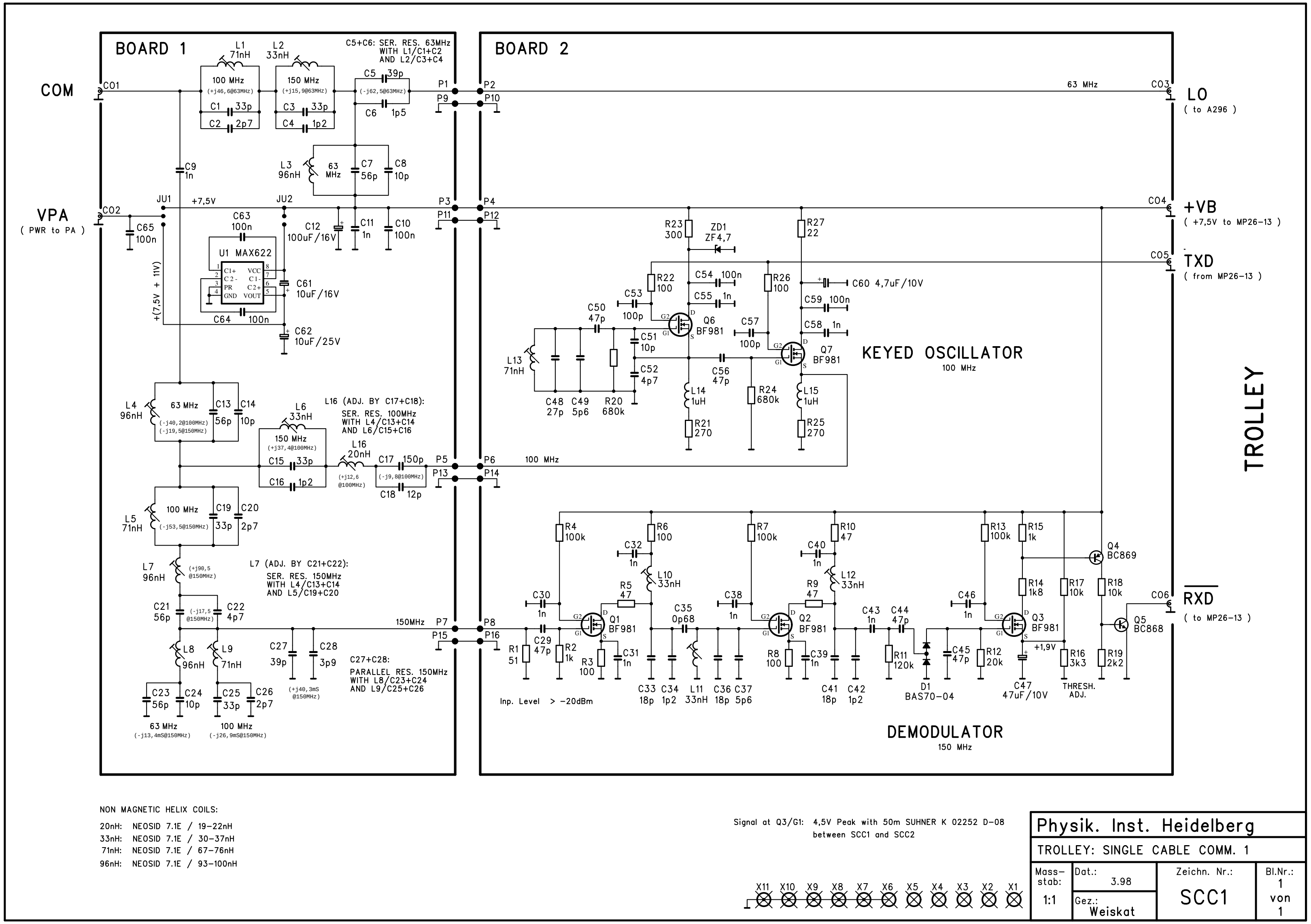

Figure A.3: The one-cable-solution interface (Ring-side).

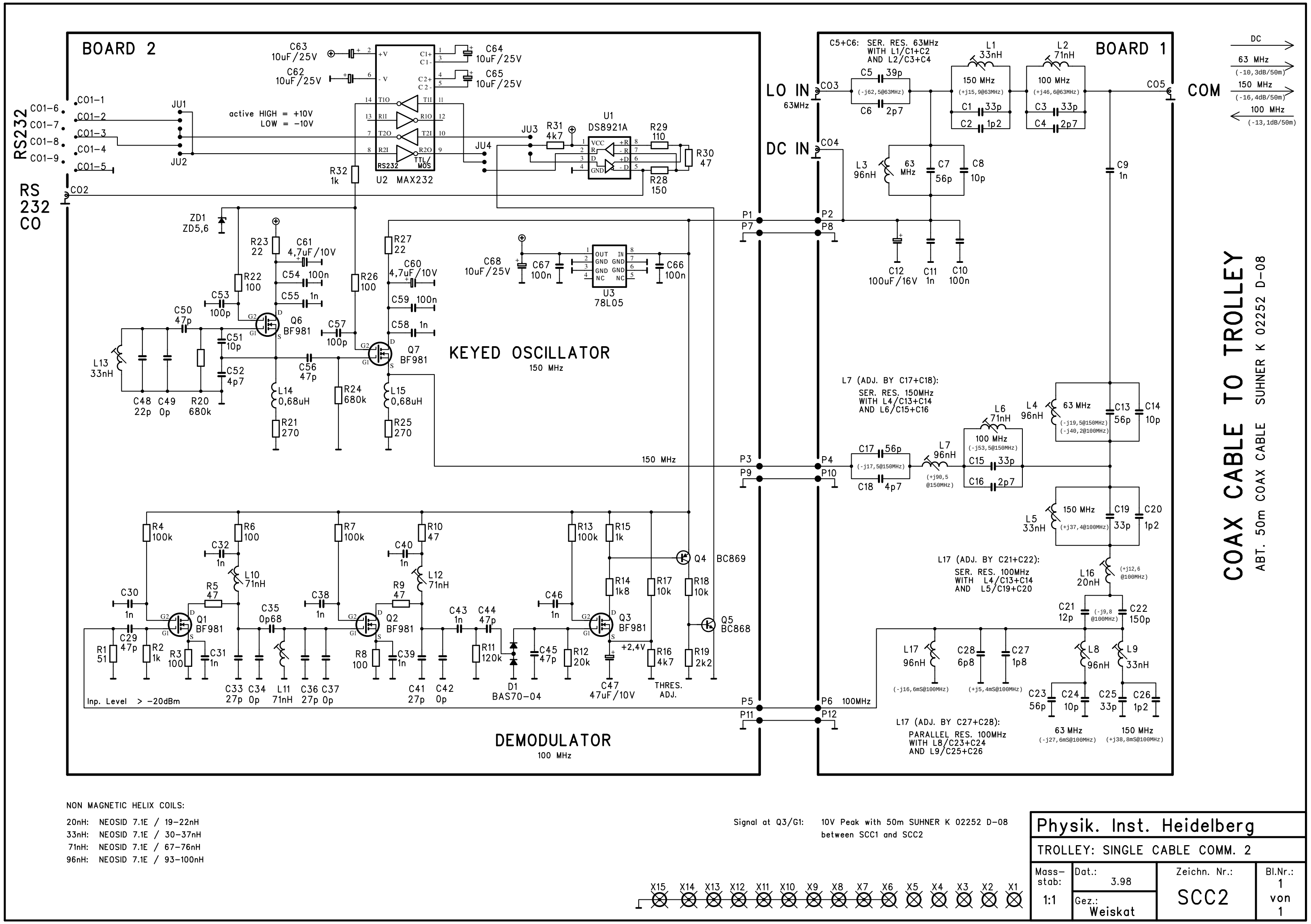

Figure A.4: The one-cable-solution interface (Trolley-side).

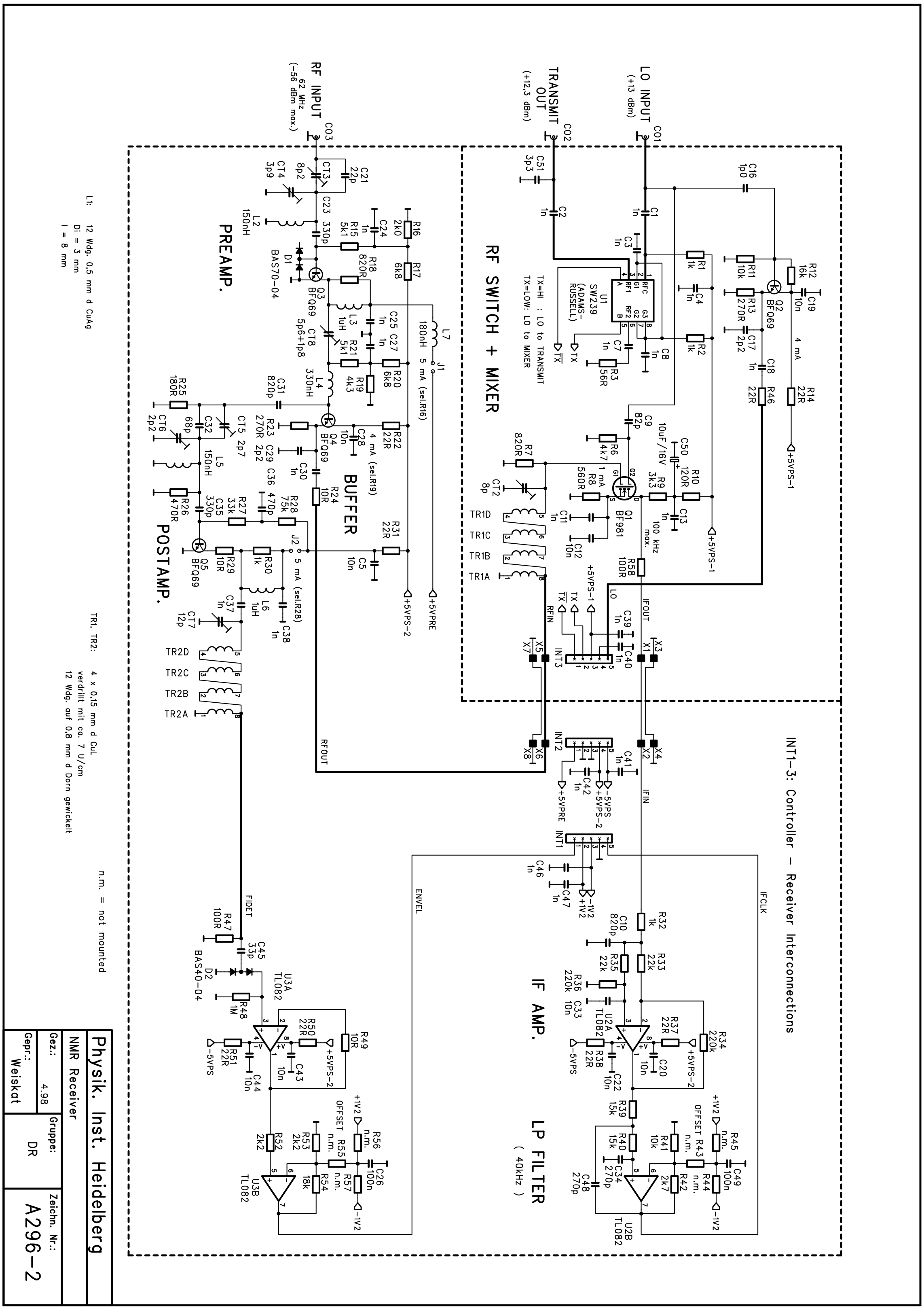

Figure A.5: The analog part of the Trolley electronics.

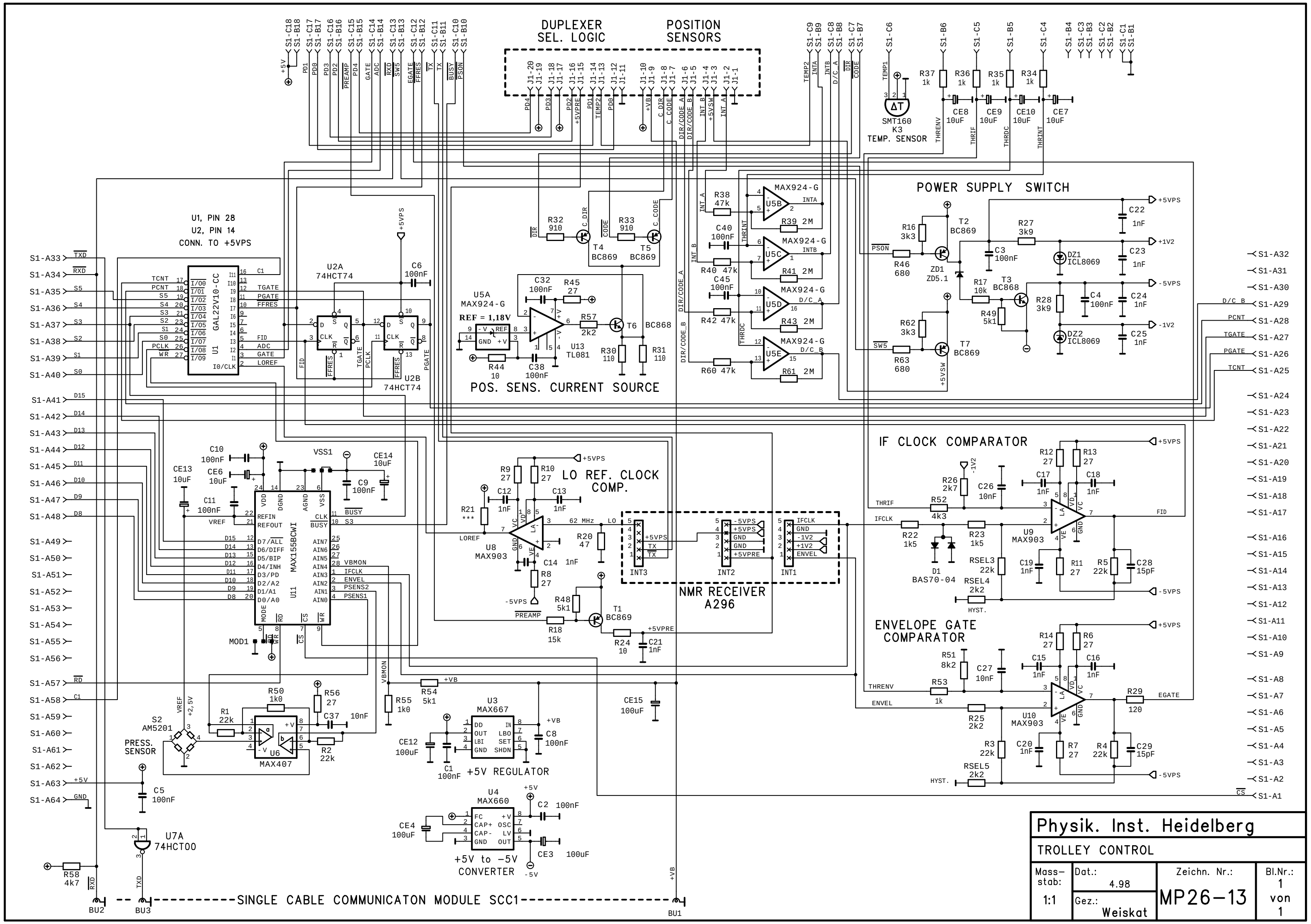

Figure A.6: The digital part of the Trolley electronics.

References

[1] J. Steinberger, Phys. Rep. 203, p. 345 (1991).

[2] J.E. Nafe, E.B. Nelson and I.I. Rabi, Phys.Rev. 71, p. 914 (1947).

[3] D.E. Nagle, R.S. Julian and J.R. Zacharias, Phys. Rev. 72, p. 971 (1947).

[4] G. Breit Phys. Rev. 72, p. 984 (1947).

[5] P.A.M. Dirac, Proc. Roy. Soc. A117, p. 610 (1928) and in The Principles of Quantum Mechanics, Oxford University Press (1947).

[6] P. Kusch and H.M.Foley, Phys. Rev. 72, p. 1256 (1947) and P. Kusch and H.M. Foley Phys. Rev. 74, p. 250 (1948).

[7] W.E. Lamb and R.C. Retherford, Phys.Rev. 71, p. 241 (1947).

[8] J. Schwinger, Phys. Rev. 73, p. 416L (1948).

[9] R. van Dyck jr., P. Schwinberg and H. Dehmelt, Phys. Rev. Lett. 59, p. 26 (1987).

[10] R. van Dyck jr. in Quantum Electrodynamics, (Directions in High Energy Physics Vol. 7) T. Kinoshita ed. World Scientific, Singapore, p. 322 (1990).

[11] P. Kunze, Z. Phys. 83, p. 1 (1933).

[12] S.H. Neddermeyer and C.D. Anderson, Phys. Rev. 51, p. 884 (1937).

[13] J.C. Street and E.C. Stevenson, Phys. Rev. 52, p. 1003 (1937).

[14] H. Yukawa, Proc. Phys. Math. Soc. Japan 17, p. 48 (1935).

[15] C.M.G. Lattes, H. Muirhead, C.F. Powell and G.P. Occhialini, Nature 159, p. 694 (1947).

[16] C.M.G. Lattes, G.P. Occhialini and C.F. Powell, Nature 159, p. 486,453 (1947).

[17] G. Charpak et al., Nuovo Cim. 37, p. 1241 (1965).

[18] J. Bailey et al., Nucl. Phys. B150, p. 1 (1979).

[19] A. Jeffery et al., IEEE Trans. Instrum. Meas. 46, p. 264 (1997).

[20] T. Kinoshita and W.J. Marciano in Quantum Electrodynamics, (Directions in High Energy Physics Vol. 7) T. Kinoshita ed., World Scientific, p. 1 (1990).

[21] T. Kinoshita and W.J. Marciano in Quantum Electrodynamics, (Directions in High Energy Physics Vol. 7) T. Kinoshita ed., World Scientific, p. 420 (1990).

[22] T. Kinoshita 'Current status of Quantum Electrodynamics', to be published.

[23] E.R. Williams et al., IEEE Trans. Instrum. Meas. 38, p. 233 (1989).

[24] E. Krüger, W. Nistler and W. Weihrauch, Metrologia 32, p. 117 (1995).

[25] T. Kinoshita, IEEE Trans. Instrum. Meas. 46, p. 108 (1997).

[26] B.L. Roberts, g-2 internal note 285 rev. Status of the Theoretical Value of (g-2).

[27] H. Terazawa, Phys. Rev. 177, p. 2159 (1969) and Progr. Theor. Phys. 39, p. 1326 (1968).

[28] J. Bell and E. de Rafael, Nucl. Phys. 11B, p. 611 (1969).

[29] R. Alemany, M. Davier and A. Höcker, Eur. Phys. J. C2, p. 123 (1998).

[30] R. Alemany, The Fourth International Workshop on Tau Lepton Physics (TAU 96), Estes Park ,Colorado, 16-19 September 1996, Tau Vector Spectral Functions and The Hadronic Contribution to ($g_\mu - 2$ and $\alpha(M^2_{Z^0}$.).

[31] M. Davier and A. Höcker, not published yet.

[32] D. Buskulic et al., Z. Phys. C20, p. 539 (1994).

[33] ALEPH collaboration (D. Buskulic et al.), A Study of τ Decays Involving η and ω Mesons. CERN-PPE-96-103 (July 1996).

[34] ALEPH collaboration (R. Barate et al.), Measurements of the Spectral Functions of Vector Current Hadronic τ Decays. CERN-PPE-97-013 (January 1997).

[35] M. Artuso et al., Phys. Rev. Lett. 72, p. 3762 (1994).

[36] J. Uhrheim, The Fourth International Workshop on Tau Lepton Physics (TAU 96), Estes Park ,Colorado, 16-19 September 1996, The Hadronic Current in Tau Lepton Decay to 2 Pseudoscalar Mesons.

[37] V. Barger, W.F. Long and M.G. Olsen, Phys. Lett. 60B, p. 89 (1975).

[38] J. Calmet et al., Phys. Lett. 61B, p. 283 (1976).

[39] S. Narison, J. Phys. G: Nucl. Phys. 4, p. 1849 (1978).

[40] L.M. Barkov et al., Nucl. Phys. B256, p. 365 (1985).

[41] T. Kinoshita,B. Nizic and Y. Okamoto, Phys. Rev. D31, p. 2108 (1985).

[42] J.A. Casas, C. Lopez and F.J. Yndurain, Phys. Rev. D32, p. 736 (1985).

[43] L. Martinovic and S. Dubnicka, Phys. Rev. D42, p. 884 (1990).

[44] Burkhardt et al., Z. Phys. C42, p. 497 (1989).

[45] A.Z. Dubnickova, S. Dubnicka and P. Strizenec, Dubna preprint E2-92-281, (1992).

[46] Talk at Workshop on 'Hadron production cross sections at DAΦNE' in Karlsruhe (Germany), (1996).

[47] S. Eidelman and F. Jegerlehner, Z. Phys. C 67, p. 585 (1995) and F. Jegerlehner, Nucl. Phys. (Proc. Suppl.) 51C, p. 131 (1996).

[48] K. Adel and F.J. Yndurain, FTUAM 95-32, (1995).

[49] W.A. Worstell and D.H. Brown, 'Comparison of New Evaluations of the hadronic Contribution to the Muon (g-2) Value', Muon (g-2) note 220, (1994).

[50] B. Krause, Phys. Lett. B 390, 392 (1997).

[51] M.Hayakawa, T. Kinoshita and A.I. Sanda, Phys. Rev. Lett. 75, p. 790 (1995) and Phys. Rev. D54, p. 3137 (1996).

[52] J. Bijnens, E. Pallante and J. Prades, Phys. Rev. Lett. 75, 1447 and 3781 (1995) and Nucl. Phys. B 474, p. 379 (1996).

[53] M. Hayakawa and T. Kinoshita, Phys. Rev. D 57, p. 465 (1998).

[54] W.A. Bardeen, R. Gastmans and B. Lautrup, Nucl. Phys. B46, p. 319 (1972).

[55] R. Jackiw and S. Weinberg, Phys. Rev. D5, p. 157 (1972).

[56] I. Bars and M. Yoshimura, Phys. Rev. D6, p. 374 (1972).

[57] J. Calmet et al., Rev. Mod. Phys. 49, p. 21 (1977).

[58] T.V. Kutho et al., Nucl. Phys. B371, p. 567 (1992).

[59] A. Czarnecki, B. Krause and W.J. Marciano, Phys. Rev. D52, p. R2619 (1995).

[60] A. Czarnecki, B. Krause and W.J. Marciano, Phys. Rev. Lett. 76, p. 3267 (1996).

[61] G. Degrassi and G.F. Giudice, hep-ph/9803384 (March 1998).

[62] P. Mery et al., Z. Phys. C46, p. 229 (1990).

[63] W. Marciano, JHF Workshop , Tsukuba (1998)

[64] R.L. Garwin, L.M. Lederman and M. Weinreich, Phys. Rev. 105, p. 1415 (1957).

[65] J.I. Friedman and V.L. Telegdi, Phys. Rev. 105, p. 1681 (1957).

[66] C.S. Wu et al., Phys. Rev. 105, p. 1413 (1957).

[67] D.P. Hutchinson et al., Phys. Rev. 131, p. 1351 (1963).

[68] J.F. Lathrop et al., Nuovo Cim. 17, p. 109 (1960).

[69] J.F. Lathrop et al., Nuovo Cim. 17, p. 114 (1960).

[70] S. Devons et al., Phys. Rev. Lett. 5, p. 330 (1960).

[71] W.H. Louisell, R.W. Pidd and H.R. Crane, Phys. Rev. 94, p. 7 (1954).

[72] D.T. Wilkinson and H.R. Crane, Phys. Rev. 130, p. 852 (1963).

[73] J. Bailey et al., Nouvo Cim. 9A, p. 369 (1972).

[74] F.J.M. Farley, Z. Phys. C 56, p. 88 (1992).

[75] F. Combley and E. Picasso, Phys. Lett. C14,no 1 p. 1 (1974).

[76] J. Aldins, T. Kinoshita, S.J. Brodsky, A.J. Dufner Phys. Rev. Lett. 23, p. 441 (1969) and Phys. Rev. D1, p. 2378 (1970).

[77] g-2 design report, 3rd edition, p. 94 (March 1995).

[78] g-2 design report, 3rd edition, p. 81 (March 1995).

[79] g-2 design report, 3rd edition, p. 327 (March 1995).

[80] D. Hertzog et al., Nucl. Inst. and Meth. A294, p. 446 (1990).

[81] D. Simon et al., Nucl. Inst. and Meth. A335, p. 86 (1993).

[82] F.J.M. Farley and B.S. Carter, Nucl. Instr. Meth. 28, p. 279 (1964).

[83] R. Carey and J. Miller, 'The Impact of Gain and Resolution Shifts on the (g-2) Frequency Measurement', Muon (g-2) Note 165 (1993).

[84] A. Abragam, Principles of Nuclear Magnetism, (Oxford University Press, 1961).

[85] C.P. Slichter, Principles of Magnetic Resonance, 3rd ed. (Springer, Berlin, 1990).

[86] B. Cowan, Meas. Sci. Technol. 7, p690 (1996).

[87] J.H. Simpson and H.Y. Carr, Phys. Rev. 111, p. 1201 (1958).

[88] R. Prigl et al., Nucl. Inst. and Meth. A 374, p. 118 (1996).

[89] R. Prigl, doctoral thesis, University of Heidelberg (1994).

[90] X. Fei, V.W. Hughes and R. Prigl, Nucl. Inst. and Meth. A 394, p. 349 (1997).

[91] g-2 design report, 3rd edition, p. 280 (March 1995).

[92] B.W. Petley, R.W. Donaldson, Metrologia 20, p. 81 (1984).

[93] W.E. Lamb Jr., Phys. Rev. 60, p. 817 (1941).

[94] H. Grotch and R.A. Hegstrom, Phys. Rev. A4, p. 59 (1971).

[95] W.D. Phillips, W.E. Cooke and D. Kleppner, Phys. Rev. Lett. 35, p. 1619 (1975).

[96] W.D. Phillips, W.E. Cooke and D. Kleppner, Metrologia 13, p. 179 (1977).

[97] g-2 design report, 3rd edition, p. 107 (March 1995).

[98] R. Prigl, private communication (April 1998).

[99] S. Redin, private communication, and PhD thesis in preparation at Yale University (1998).

[100] K. Halbach, Nucl. Inst. and Meth. 107, p. 529 (1963).

[101] M. Perdekamp et al., g-2 internal note 287 Magnet Commissioning: Analysis of the Energy Extraction Data at Half and Full Field (1997).

[102] F. Krienen et al., Nucl. Inst. and Meth. A283, p. 5 (1989).

[103] G. Danby et al., IEEE Transactions on Magnetics 30-4, p. 1766 (1989).

[104] E. Efstathiadis, B.L. Roberts and Y.K. Sermertzidis, 'Tests of a new version of tracking code', Muon(g-2) note 283 (1997).

[105] B. Morse, private communcation (1998).

[106] B. Cowan, Meas. Sci. Technol. 7, p. 690 (1996).

[107] Cohen et al., Rev. of Mod. Phys. 59, p. 1121 (1987).

[108] P. Cushman Letter of intend to BNL-AGS in preparation

[109] K. Assamagan et al., Phys. Lett. B335, p. 231 (1994).

[110] Y. Semertzidis Letter of intend to BNL-AGS (1998)

[111] Abdullah et al., Phys. Rev. Lett. 65, p. 2347 (1990).

[112] J.L. Flowers, P.W. Franks and B.W. Petley, IEEE Trans. Instr. Meas. 44, p.572 (1995).

Acknowledgements

Last but not least I would like to express my thanks to all who have contributed to the success of this work:

Priv.-Doz. Dr. K. Jungmann for many fruitful discussions as well as for advising this thesis.

Prof. Dr. G. zu Putlitz for his active participation in the developments and the experiment.

Prof. Dr. U. Haeberlen for his interest in my work and the experiment.

Dr. R. Prigl for support at BNL and steady interest in all stages of this thesis.

All members of the muon group - A. Breitrück, M. Diaz Trigo, U. Gottwald, D. Hübl, J. Merkel, V. Meyer, P. Neumayer, Dr. T. Prokscha, Dr. I. Reinhard, R. Santra, Dr. P. Schmidt, Dr. W. Schwarz, K. Träger, C. Wasser, Dr. L. Willmann, Dr. V. Yakhontov and Dr. L. Zhang - for a friendly atmosphere and support whenever needed.

Members of the collaboration - J. Benante, Dr. H.N. Brown, Dr. G. Bunce, Dr. R.M. Carey, Prof. Dr. P. Cushman, Dr. G.T. Danby, Dr. P.T. Debevec, Dr. S.K. Dhawan, W. Deninger, Dr. E. Efstathiadis, Dr. F.J.M. Farley, Dr. X. Fei, J. Geller, S. Giron, Dr. M. Grosse-Perdekamp, Prof. Dr. D.W. Hertzog, Prof. Dr. V.W. Hughes, Dr. L. Jia, Dr. D. Kawall, Dr. B.I. Khazin, J. Kindem, Prof. Dr. T. Kinoshita, Dr. F. Krienen, R. Larsen, M. Mapes, Dr. W. Meng, D. Miller, Dr. J.P. Miller, Dr. W.M. Morse, C. Pai, S.I. Redin, Dr. O. Rind, Prof. Dr. B.L. Roberts, Dr. S. Sedykh, Dr. Y.K. Semertzidis, L. Snydstrup, A. Stillman, Dr. L.R. Sulak, T. Tallerico, Dr. C. Timmermans, Dr. D. Urner, Dr. D. Winn, Dr. K. Woodle, Dr. D. Zimmerman - for their input.

The staff of the electronics and mechanical workshop of the Physikalisches Institut for their extraordinary support.